

Study of the low-energy d+d reaction in liquid metals
(液体金属中での低エネルギー d+d 反応の研究)

Yuki HONDA
Department of Physics, Tohoku University

2017

Abstract

Liquid In, Pb, Sn and Bi were bombarded by a deuteron beam with an incident energy of 3.3 – 20 keV to study a strange $d+d$ reaction which was discovered recently. The reaction was clearly observed only when a molecular deuteron was used as the incident beam. The yields and energy spectra of proton, triton and ^3He -particle from the reaction were obtained.

In order to clarify the mechanism of the reaction, a Monte Carlo simulation of the $d+d$ reaction based on cooperative colliding mechanism (CCM) was developed. For the $d+d$ reaction through the CCM, reacting nuclei are two deuterons in the same molecule. One deuteron in a molecular beam change a direction due to an elastic scattering with a metal atom, and the scattered deuteron collides with the other deuteron in the same molecule.

The results of the simulation quantitatively represented the experimental yield and energy spectra. The screening potentials were deduced from the absolute value of the $d+d$ reaction yield and its energy dependence as $U_s = 170_{-30}^{+30}(\text{sta.}) \text{ }_{-110}^{+110}(\text{sys.})$, 0_{-0}^{+10+60} , $250_{-20-190}^{+20+190}$, $0_{-0}^{+10+120}$ eV for the In, Pb, Sn and Bi target, respectively. The deduced screening potentials were consistent with the theoretical ones of about 60 eV within a standard deviation. It became clear that the $d+d$ reaction through the CCM affects the value of the screening potential measured so far with the deuteron molecular beam. Since the misinterpretation of the screening potential of several hundred eV is caused by the CCM, the CCM must be considered for a determination of the screening potential.

Contents

1	Introduction	1
1.1	Nuclear reaction in dense plasmas	2
1.2	Strongly coupled plasma in metal	3
1.2.1	Anomalous enhancement of $d + d$ reaction in metals	4
1.2.2	Interpretation of enhancement	5
1.2.3	Experimental uncertainty	9
1.3	New method to determine screening potentials in metal	9
1.4	The aim of this study	10
2	Low-energy $d + d$ reaction	13
2.1	Cross section	13
2.2	Screening effect	15
2.3	Astrophysical S-factor	16
2.4	Angular distribution	18
2.5	Kinematics of $d + d$ reaction	21
2.5.1	Kinetic energy of emitted nuclei	21
2.5.2	Solid angle ratio	23
3	Coulomb scattering in matter	27
3.1	Differential Cross section	27
4	Cooperative colliding mechanism	35
4.1	Reaction Process	35
4.2	Thin-target yield	36

4.3	Thick-target yield	38
4.4	Realistic calculation	40
4.4.1	Trajectory calculation	40
4.4.2	Collision point	45
4.4.3	Total yield	48
4.5	Yield and energy spectra at laboratory frame	49
4.5.1	Yield	50
4.5.2	Energy spectra	50
4.5.3	Feature of the CCM spectra	51
5	Experiment	63
5.1	Beam line	65
5.1.1	Beam energy	67
5.1.2	Beam position	67
5.2	Reaction chamber	68
5.2.1	Target holder	71
5.2.2	Scraper	72
5.3	Experimental setup	73
5.3.1	Detector	73
5.3.2	Faraday cup	77
5.3.3	Thermometer	77
5.3.4	Target scanning system	78
5.4	Metal target	79
5.4.1	Stopping power	81
5.4.2	Target temperature	84
5.5	Solid angle	84
5.6	Data acquisition system	85
5.6.1	Block diagram for energy measurement	86
5.6.2	Block diagram for time and current measurement	88
6	Experimental results and analysis	89
6.1	Raw spectra	89
6.2	Background event	90
6.2.1	Thermal noise	94

6.2.2	Absorber background	94
6.3	Energy spectra	99
6.4	Yield	99
6.4.1	Integral region	99
6.4.2	Excitation function	103
7	Discussion	111
7.1	Results of experiment and calculation	111
7.1.1	Energy spectra	111
7.1.2	Yield	112
7.2	Screening potential	112
7.2.1	Interatomic potential dependence of screening potentials	112
7.2.2	Systematic uncertainty	121
7.2.3	Screening effect for the CCM	122
7.2.4	Discussion about screening potential	124
7.3	Contribution of CCM to solid metal experiment	125
8	Conclusions	129
8.1	Future issue	130
A	Calibration of the emissivity	133
A.1	Calibration of the thermal emissivity	133
B	Rest deuteron in the liquid metal	137
B.1	Rest target background	137
C	Absorber event	143
C.1	Absorber background	143
D	Energy calibration	147
D.1	Energy Calibration	147
E	Solid angle correction	151
E.1	Run dependence of solid angle	151
E.1.1	Target height	151
E.1.2	Solid angle correction depend on the target height	154

E.1.3 Solid angle correction depend on the beam position 156

Chapter 1

Introduction

A nuclear transmutation by collision of nuclei was made by Rutherford in 1919 [1]. Rutherford irradiated the α particles, which are emitted in an α -decay chain starting from Radium C (^{214}Bi), to nitrogen and observed $^{14}\text{N}(\alpha, p)^{17}\text{O}$ reaction. From this result, the existence of a proton which is a minimum component of a nucleus was confirmed. After that, in 1932, a scattering experiment using a proton beam was performed for the first time by Cockcroft and Walton [2]. They developed Cockcroft-Walton Accelerator which succeeded to accelerate a proton to 800 keV, and they observed the $^7\text{Li}(p, \alpha)^4\text{He}$ reaction. With the advent of the accelerator, a controlling the incident particles and energies became possible. It pioneered the way for many nuclear studies. As a result of the development of the accelerator, high energy physics experiments are advancing, for example, study of the quark gluon plasma by a collision of high energy heavy ion. On the other hand, researchers of nuclear astrophysics are interested in the nuclear reaction in the lower energy region to clarify nucleosynthesis process in the universe and stars,

In order to clarify the stellar evolution and the nucleosynthesis in the universe, low-energy nuclear reactions are studied. For example, in Big Bang Nucleosynthesis (BBN), it is thought that light nucleus ($A \leq 7$) were generated in the early stage of the universe [3]. BBN is thought to proceed at $k_B T \sim 100$ keV. In such a temperature, nuclear reactions occurring through the tunneling effect are dominant because almost the particles cannot overcome the Coulomb potential between the reacting nuclei.

Since the tunneling probability depends on the collision energy exponentially, the cross section rapidly decreases as the energy decreases. The energy region which mostly contributes to the reaction is obtained by the multiplication of the cross section with the Maxwell-Boltzmann distribution, called Gamow peak,. As for the BBN, the region is 100–300 keV, and the precise cross section in such energies was required. The result is summarized in reference [4]. The abundance ratio of H, D, He and Li in the early universe calculated by using their cross section well reproduces the element abundance ratio in the observed primordial stars. This shows the validity of BBN and is considered as a great achievement of the study of the low-energy nuclear reactions.

1.1 Nuclear reaction in dense plasmas

When a nuclear reaction occurs in space, in almost cases, these are surrounded by a plasma. It is thought that the plasma has a great influence on the reaction rate. The influence by the plasma is classified by its temperature and density. The strength of the ion-ion interaction in the plasma is represented by Coulomb coupling parameter Γ_i , and it is described as follow in one component plasma,

$$\Gamma_i = \frac{E_C}{k_B T} = \frac{(eZ_i)^2}{k_B T} \left(\frac{3}{4\pi n_i} \right)^{-1/3}. \quad (1.1)$$

Here, E_C and $k_B T$ represent the Coulomb energy and the thermal energy. Thus, Γ_i means the ratio of these. When $\Gamma_i \ll 1$, the plasma is ideal, and the interaction between ions can be ignored. It is though that ideal plasma is generated in the core of the sun ($\Gamma \sim 0.04$). There, the nuclear reaction rate may be enhanced by only several percents [5]. When $\Gamma_i > 1$, the plasma is called strongly coupled plasma which has a great influence on the reaction rate. For example, Ichimaru calculated the reaction rate of the $^{12}\text{C} + ^{12}\text{C}$ in the white dwarf, whose Γ_i is approximately 57. The reaction rate was estimated to be increased by approximately 23 orders of magnitude. This $^{12}\text{C} + ^{12}\text{C}$ reaction is thought to a trigger for Type Ia supernova which plays an important role of heavy element synthesis.

An enhancement of the nuclear reaction rate is also caused by electrons in a plasma, which screens a Coulomb barrier of a reacting nucleus. It is called electron screening effect. The most extreme example of the electron screening effect is pyc-

nonnuclear reaction proposed by Cameron [6]. In a very dense and low temperature environment, it is expected that electrons screen the almost all Coulomb potential of the nucleus, and the nuclear reaction rate is dominated by its density rather than its temperature. The effect of the electron screening is large at low temperature star. Ichimaru calculated the rate of $d + d$ and $d + p$ reaction in the Giant planet where the temperature and the density were supposed to be $T = 2 \times 10^4$ K and $\rho = 5$ g/cm³. The reaction rate was estimated to be increased by approximately 10 orders of magnitude [5]. With such a great enhancement, Ouyed and Jaikumar argued that the observed inflated size of some giant exoplanets (hot Jupiter) can be explained by an energy production from the screened $d + d$ reactions at the core [7]. The electron screening effect also contributes to the enhancement of the $^{12}\text{C} + ^{12}\text{C}$ reaction in the white dwarf. Potekhin and Chabrier pointed out that the screening effect can greatly influence to the ignition condition of the supernova [8].

In this way, from the viewpoint of the nuclear reaction occurring in the dense plasma, not only the measurement of the cross section but also the study of the influence from the surrounding environment is very important.

1.2 Strongly coupled plasma in metal

Since it is difficult to reproduce the stellar plasma in the terrestrial laboratory, studies of the electron screening effect are conducted utilizing the nuclear reaction in metals. The inside of the metal composed of conduction electrons and ions is the same as the plasma.

As is well known, electrons in metals are degenerated. The screening effect by degenerated electrons are estimated using the Thomas-Fermi screening model. When the nucleus of charge Z_1 is placed in the electron ocean of density n_e , the potential around the nucleus is calculated using the Thomas-Fermi approximation,

$$\phi(r) \sim \frac{Z_1 e}{r} - \frac{Z_1 e}{\lambda_F}. \quad (1.2)$$

Here, Thomas-Fermi screening length λ_F is described in following equation with Fermi energy E_F

$$\lambda_F = \sqrt{\frac{E_F}{6\pi n_e e^2}}, \quad (1.3)$$

and

$$E_F = \frac{\hbar^2}{2m_e} (3\pi^2 n_e)^{2/3}. \quad (1.4)$$

The second term of the Equation (1.2) corresponds to the decrease in potential. When a nucleus of charge Z_2 is incident from the outside without disturbing the polarization of electrons, the value of the decreasing potential due to screening is

$$U_s = \frac{Z_1 Z_2 e^2}{\lambda_F}. \quad (1.5)$$

U_s is usually called screening potential. Assuming a $d+d$ reaction where $Z_1 = Z_2 = 1$, $U_s = 20\text{--}30$ eV is expected in the metal.

1.2.1 Anomalous enhancement of $d+d$ reaction in metals

Measurement of the screening potential of the $d+d$ reaction in metals has been developed using deuteron beams. Deuterons are accumulated in solid metal and the $d+d$ reactions between the beam and accumulated deuteron are observed. Since the reaction occurs in the metal, an increase in reaction yield is expected due to screening by conduction electrons. Up to the present, a screening potential of hundreds of eV was reported for many metals which value greatly exceeds the theoretical expectation. Examples of the measurement are shown below.

Tohoku experiment

Kasagi *et al.* bombarded D^+ beam of 2.5 – 10 keV and, measured excitation functions of the yield of protons emitted in the $D(d,p)T$ reaction in Ti, Fe, Pd, PdO and Au [9]. They bombarded the host material with 10 keV deuteron beam, and made deuteron-saturated target. The deduced screening potentials were 70 ± 10 , 65 ± 10 eV for Au and Ti respectively, but, very large values of 600 ± 20 , 310 ± 20 , 200 ± 15 eV for PdO, Pd and Fe, respectively. Kasagi *et al.* argued that the large enhancement cannot be explained by electron screening alone and suggested the existence of an additional mechanism of the screening in solids.

Bochum experiment

Raiola *et al.* bombarded D^+ and D_3^+ beam of 8 – 30 keV and, measured screening potentials for the $d + d$ reactions for many targets including 32 kinds of metals [10]. (The beam energy range inferred from Figure 1 of reference [10]). They bombarded the host material with 10 and 30 keV deuteron beam, and made deuteron-saturated target. A large screening potential $U_s = 100\text{--}700$ eV has been reported for the metal target. On the other hand, low values of $U_s \leq 80$ eV have been reported for insulators and semiconductors, 3 and 4 groups, and lanthanoids. To explain the large screening potentials, Raiola *et al.* propose Debye screening model which treat the conduction electrons as a classical plasma. The Debye screening is discussed in § 1.2.2.

Berlin experiment

Czerski *et al.* bombarded D^+ and D_2^+ beam of 5 – 60 keV and, measured screening potentials of the $d + d$ reactions for Al, Zr and Ta [11]. Czerski *et al.* pointed out that deuteron density can be changed during beam irradiation, even if the deuteron is saturated. In order to deal with the change, the S-factor of the $d + d$ reaction is determined every short time, and the number of incident deuterons and the reaction yield are continuously obtained. Czerski *et al.* argued that the technique can separate the deuteron density and screening potentials, and it can decide the screening potentials more precisely. The estimated screening potentials are 190 ± 15 , 297 ± 8 and 322 ± 15 eV for Al, Zr and Ta respectively.

1.2.2 Interpretation of enhancement

The measured enhancement factor for the $d + d$ reaction in metals cannot be explained with the screening potentials of 20 – 30 eV expected in the Thomas-Fermi screening model. Therefore, various theoretical considerations are being made. Examples are shown below. In spite of these efforts, a unified interpretation that explains many experimental results has not been obtained yet.

Self-consistent dielectric function theory

Czerski *et al.* calculated screening contributions from the polarization of bound electrons of host atom and "cohesion" screening originated from different binding energies

of deuterons and α -particles in crystal lattices in addition to a polarization of conduction electrons which is considered in Thomas-Fermi model [12]. The reported experimental and calculated screening potentials for Li, Be, C, Al, Zr, Pd and Ta are shown in the figure 1.1. The open circles shows the sum of the contribution of screening from polarization of conduction and bound electrons, and the open triangles shows one from cohesion screening. The solid circles shows the sum of calculated polarization and cohesion screening, and solid square shows the experimental screening potentials. Czernski *et al.* argues that the calculation can explain the material dependence of screening potentials qualitatively, but the calculated value is about half of the experimental value.

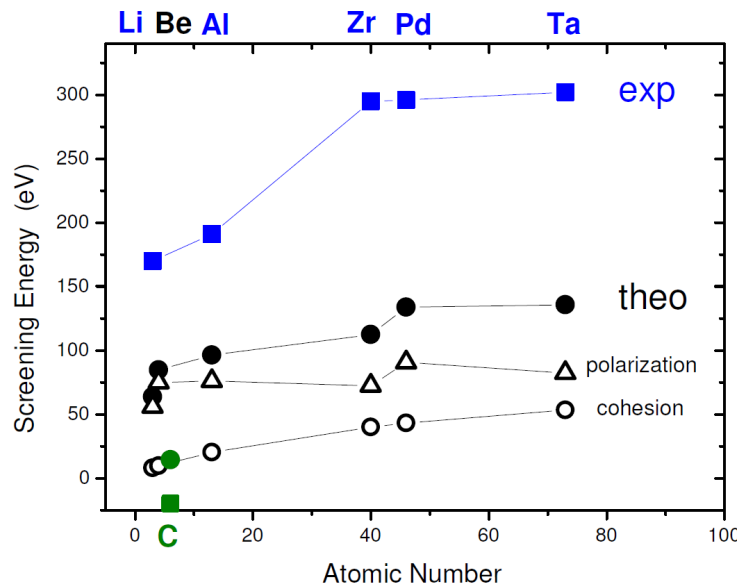


Figure 1.1: Experimental and theoretical electron screening energies reported by Czernski *et al.* [12]

Debye screening

Bonomo *et al.* argues that the large screening potentials in metal can be explained by Debye's classical plasma theory [13]. In the Debye screening model, it is assumed that conduction electrons are treated as semi-free classical particles and their velocity distribution follows the Maxwell's distribution. In the region where the Coulomb potential is sufficiently small with respect to the movement of electrons, the screened

potential is expressed as [14]

$$\phi \sim \frac{eZ_1}{r} \left(1 - \frac{r}{\lambda_D} \right), \quad (1.6)$$

given by Debye screening length

$$\lambda_D = \left(\frac{\epsilon_0 k T_e}{n e^2} \right)^{1/2}. \quad (1.7)$$

Here, n is the uniform electron density and T_e is the temperature of electrons. λ_D becomes longer as the temperature rises, and the screening effect decreases. This is due to the fact that the movement of electrons becomes large, it becomes possible to escape from the target potential and the electron density around the target decreases.

Raiola *et al.* measured the temperature dependence of the screening potentials for Pt and Co in the range of $T_e = 20\text{--}340$, $20\text{--}200$ °C, respectively, and argues that the dependence corresponds to $U_D \propto 1/\sqrt{T_e}$ which consist with the calculated one from the Debye model [15]. Figure 1.2 shows the screening potentials for Pt for each temperature reported by Raiola *et al.* The red points show the experimental screening potentials, and the dotted line shows the temperature dependence of the screening potentials predicted from the Debey model. The absolute value of the screening potential is normalized with minimum temperature data.

The temperature dependence of the screening potentials are also measured by Bystritsky *et al.* [16]. They measured the screening potentials of $d(d,n)^3\text{He}$ reactions for TiD_2 , ZrD_2 at the temperature of $T_e = 20 - 200$ °C by the D^+ beam bombardment with the energy of $E_d = 7 - 12$ keV. The deduced screening potentials for TiD_2 are $U_s = 125 \pm 34$, 133 ± 47 and 113 ± 38 eV at the temperature of $T_e = 20$, 60 and 200 °, and the one for ZrD_2 are $U_s = 205 \pm 37$, 186 ± 37 and 196 ± 29 eV at the temperature of $T_e = 20$, 60 and 200 °, respectively. There can be seen no temperature dependence of $U_e \propto 1/\sqrt{T_e}$.

Channeling effect

Bystritsky *et al.* explains the increase of yield at low energy by channeling effect in metal lattice [17]. Since the deuteron that caused channeling can go deeper in the metal, the effective number of the target increase. Because the acceptance angle of

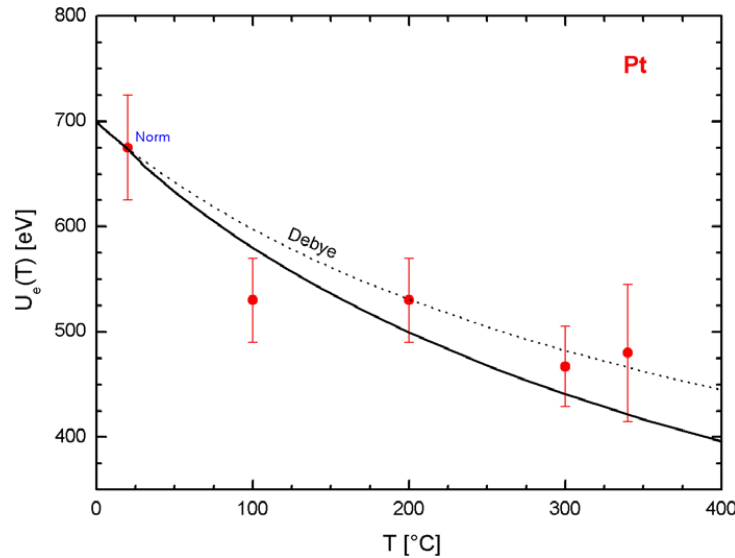


Figure 1.2: Screening potentials for Pt in the temperature range of 20–340 °C reported by Raiola *et al.* [15]. The red points show the experimental screening potentials, and the dotted curve shows the temperature dependence of the screening potentials predicted from the Debye model.

the channeling increases as the incident energy decreases, the enhancement of yield at low energy can be seen. Bystritsky *et al.* argue that the results can be explained by either the channeling model or the screening model, and that a series of experiments with different crystal orientations should be performed.

0^+ resonance of ^4He

Czerski *et al.* explains the large enhancement of low energy yield by a combination of 0^+ resonance of ^4He and electron screening potential. They pointed out the disagreement between the experimental enhancement factor and the theoretical one due to the electron screening. They argued that if the 0^+ resonance of ^4He at the reaction threshold exists, the energy dependence of the experimental enhancement factor can be explained. They calculated the theoretical enhancement factor taking into the resonance, and fit to the experimental one. The width and the phase shift of the resonance were treated as the free parameter as well as the screening potential. The screening potential obtained from the fit considering the resonance is 109 ± 30 eV. It is argued that the value is close to the expected one, 80 eV obtained by self-consistent

dielectric function theory.

1.2.3 Experimental uncertainty

While the theoretical considerations described above are done, experimental problems are also discussed. Huke *et al.* points out the contamination of the metal surface and the nonuniformity and instability of the deuteron density distribution which caused the large influence to deduced screening potentials [18, 19]. The contamination of the metal surface mainly consists of two kind of mechanisms, metal oxidation and carbon layer formation. The metal oxide is formed from oxygen from residual moisture decomposed by beam. Since the oxygen binds more strongly to metal than hydrogen, deuterons do not accumulate in that region. The region can not provide the $d + d$ reaction and only cause energy loss of the beam. This may decrease the values of deduced screening potentials. On the other hand, the carbon layer is formed from carbon from the decomposed oil used in the vacuum pump. Many deuterons accumulate in the carbon layer, but conduction electrons do not exist, and screening effect can not be obtained.

Huke, Czerski and Heide studied the influence of the surface contamination on the deduced screening potentials [19]. They measured the $d + d$ reaction in Ta with several kinds of the surface contamination conditions, and deduced screening potentials. The deduced screening potentials are 210 – 460 eV, which indicates that the surface contamination can be a large systematic errors. They argues that to conduct precise measurement, a high vacuum of 10^{-10} hPa or less is necessary so as not to form a contaminating layer.

Bystritsky *et al.* who previously showed the channeling model argue that the crystal structure of the target should be reported to consider the difference of the channeling effect due to the variety of the orientation of the crystal structure [16].

1.3 New method to determine screening potentials in metal

In order to clarify the influence from the dense plasma in the nuclear reaction rate, our group have investigated the $d + d$ reaction in various metals and also the $\text{Li} + \text{p,d}$

reaction [9, 20–22]. In a series of the liquid metal experiments, Yoshida found strange $d + d$ reaction which occurred when the liquid In was bombarded by D_3^+ beam [23]. He obtained completely different energy spectra and excitation functions from the previous solid metal target experiments. As a result of a systematic investigation by Honda, it was identified that the unique $d + d$ reaction is a nuclear reaction resulting from the use of a molecular beam [24]. The reaction mechanism is schematically shown in Figure 1.3. In a molecular beam, two or three deuterons are present at a very close position of about 1 Å, and they are incident on the target while maintaining the distance. Even after incidence, the deuteron moves straight while maintaining its positional relationship until one of the deuteron causes Coulomb scattering with the target atoms. The scattering changes the direction of travel. When there is a partner deuteron at the destination of the scattering, a $d + d$ reaction occurs with a probability according to their relative momentum. We call it Cooperative colliding mechanism (CCM). The yield of CCM is mainly determined from 1) interatomic distance between deuterons, 2) the elastic scattering cross section between deuterons and metals and 3) cross section of $d + d$ reaction. The CCM is a complicated process involving atomic physics and nuclear physics. A deep understanding is necessary to understand the CCM.

If we can calculate the precise reaction yields of the CCM, it can be possible to determine the screening potentials excluding the uncertainty of the deuteron density. The target nucleus in the CCM is a deuteron contained in the same molecule, and no change in the deuteron density during measurement occurs. It is not necessary to accumulate deuterons in the metal, so liquid metal can be used. With liquid metal target, the surface is always changing due to convection, and it avoid forming a contamination layer. In addition, liquid metal loses its lattice structure, so channeling as claimed by Bystritsky does not occur.

1.4 The aim of this study

The CCM has been discovered recently and qualitatively understood quickly. However, it is necessary to fully understood this process in order to accurately deduce the physical quantity. Therefore, the main purpose of this study is to deepen the understanding of the newly found CCM, which is a complicated process involving atomic

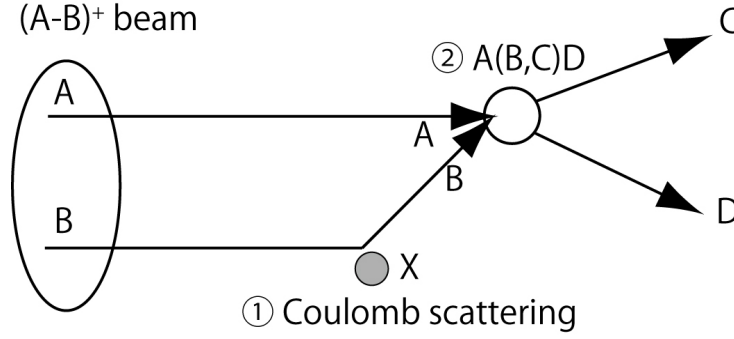


Figure 1.3: Diagram of cooperative colliding mechanism (CCM).

physics and nuclear physics. For this purpose, we systematically accumulate experimental data using D_3^+ molecular beam. In addition, we pioneer the simulation by a model calculation. We also aim to obtain the screening potential of the $d + d$ reaction in metal using the CCM, and clarify the characteristics, problems and limitations of it. We compare it with the previously reported values of the screening potential and deepen the understanding of the screening potential of $d + d$ reaction in metal.

As long as the deuteron molecular beam is used, the $d + d$ reaction through the CCM always occurs. In most past experiments, deuteron molecular beams were used to obtain lower beam energy. Therefore, it is plausible that the CCM contributes to its yield enhancement and the deduced screening potential might be overestimated. It is, thus, another aim of this study to discuss how much the effect of the CCM is in the $d + d$ reaction to be observed usually.

Chapter 2

Low-energy $d + d$ reaction

The $d + d$ reaction has three channels:

$$d + d \rightarrow p + t + 4.03 \text{ MeV} \quad (2.1)$$

$$d + d \rightarrow n + {}^3\text{He} + 3.27 \text{ MeV} \quad (2.2)$$

$$d + d \rightarrow {}^4\text{He} + \gamma + 23.08 \text{ MeV} \quad (2.3)$$

In these channels, reaction (2.1) and (2.2) occur through the strong interaction, and (2.3) occurs through the strong and electromagnetic interactions. Therefore, the branching ratio of the $d + d$ reaction is (2.1):(2.2):(2.3) $\sim 1:1:10^{-7}$. In this work, we use the $d + d$ reaction (2.1) and (2.2) with the center-of-mass (CM) energy for the $d + d$ system below 40 keV. In this chapter, the cross section and kinematics for the (2.1) and (2.2) reaction is discussed.

2.1 Cross section

Two deuterons involved in the $d + d$ fusion reaction must be close ($\sim \text{fm}$) to get the attractive strong force. For the $d + d$ reaction, they should have about 350 keV to overcome the electric repulsion since each deuterons have a positive charge. A Coulomb potential between two nuclei is expressed using an atomic number for the

incident nucleus Z_1 and that for the target nucleus Z_2 :

$$V(r) = \frac{Z_1 Z_2 e^2}{r} \quad (2.4)$$

where r stands for the distance between the two nuclei and e is the elementary charge. In the classical mechanics, the kinetic energy of the incident nucleus must exceed the Coulomb barrier to get the nuclear fusion reaction. In the quantum mechanics, the incident nucleus tunnels through a Coulomb barrier, and the nuclear fusion reaction takes place. The cross section σ as a function of the CM energy E is usually given by

$$\sigma(E) = \frac{S(E)}{E} \exp\{-2\pi\eta(E)\} \quad (2.5)$$

with the astrophysical S -factor $S(E)$. The Sommerfelt parameter $\eta(E)$ is given by

$$\eta(E) = Z_1 Z_2 \alpha \sqrt{\frac{\mu c^2}{2E}} \quad (2.6)$$

with the fine structure constant α and the reduced mass μ between the two nuclei involved in the reaction. In equation (2.5), the geometrical factor $1/E$ is caused by the fact that the cross section is proportional to the size of the wave packet for the incident nucleus $\pi\lambda^2$. The Gamow factor $\exp\{-2\pi\eta(E)\}$ is an approximated tunneling probability through the Coulomb barrier for the S -wave incident nucleus (the orbital angular momentum $L = 0$). The Gamow factor is expressed as

$$\exp\left\{-\sqrt{\frac{8\mu}{\hbar^2}} \int_{R_n}^{R_e} \sqrt{V(r) - E} dr\right\} \sim \exp\{-2\pi\eta\} \quad (2.7)$$

in the WKB approximation with

$$\frac{R_n}{R_e} \sim 10^{-3} \ll 1 \quad (2.8)$$

where R_n denotes the radius of the target nucleus and R_e stands for the classical turning point. The $S(E)$ includes all other effects, and is obtained by an equation

$$S(E) = \sigma(E) E \exp\{2\pi\eta(E)\} \quad (2.9)$$

using the cross sections obtained in the experiment and those obtained in the calculation. The $S(E)$ is known to be a function which changes very gradually as a function of the energy except near the resonance. While the Gamow factor changes drastically for different energies, and it is dominant factor for the low-energy nuclear reaction rate.

2.2 Screening effect

The low-energy nuclear-fusion reaction takes place owing to the quantum tunneling. Therefore, reduction of Coulomb barrier makes the reaction rate increase. Let us consider the atom-atom collision. The electric repulsion between the incident and target atoms disappears until atoms touch each other, because the charge of the nucleus is screened by its electron cloud. Thus, the effective Coulomb barrier is lower than the bare one.

Let us define the reduction of Coulomb potential due to the electric screening as the screening potential U_S . The modification of the potential from the original $V(r)$ to the screened $V(r) - U_S$ corresponds to the increase of the effective CM energy E to $E + U_S$. The cross section is expected to have a form:

$$\sigma(E) = \sigma_0(E + U_S) = \frac{S(E + U_S)}{E + U_S} \exp\{-2\pi\eta(E + U_S)\}, \quad (2.10)$$

where σ_0 stands for the cross section for bare nuclei, the nucleus does not have an electron cloud, namely it is a full-stripped nucleus. Assuming $S(E)/E$ changes very slightly with respect to E and $U_S \ll E$, the enhancement factor $f(E)$ is described as

$$f(E) \equiv \frac{\sigma(E)}{\sigma_0(E)} \sim \exp\left(\pi\eta(E)\frac{U_S}{E}\right). \quad (2.11)$$

Every low-energy fusion reaction is affected by the screening effect since it is very rare case that both the incident and target nuclei are full stripped. As discussed in § 1.2, the screening effect has a very large contribution for the nuclear fusion reactions in the metal.

2.3 Astrophysical S-factor

The astrophysical S -factor $S(E)$ is obtained from Eq. (2.9) using the measured or calculated cross sections. Although the geometrical factor and tunneling probability of the Coulomb barrier for the S -wave are absent in $S(E)$, the other components are expected to be involved. The low-energy nuclear fusion reaction exponentially decreases as the CM energy becomes lower. The uncertainties both in the cross section measurement and CM energy determination affect the evaluation of $S(E)$.

Krauss *et al.* measured the cross section for the $d + d$ reaction using a window-less gas target to minimize the systematic uncertainty, and reported $S(E)$ for $E = 2.98$ – 162.5 keV [25]. The $S(E)$ is given in a quadratic function,

$$S(E) = S(0) + \dot{S}(0)E + \frac{1}{2}\ddot{S}(0)E^2 \quad (2.12)$$

and the obtained parameters $S(0)$, \dot{S} , and $\ddot{S}(0)$ are summarized in Table 2.1.

Table 2.1: $S(0)$, \dot{S} , and $\ddot{S}(0)$ parameters for describing $S(E)$ in Equation (2.12) reported by Krauss *et al.* [25] These parameters are obtained for the $D(d,p)T$ and $D(d,n)^3\text{He}$ reactions.

reaction	$S(0)$ (keV·b)	$\dot{S}(0)$ (b)	$\ddot{S}(0)$ (b/keV)
$D(d,p)T$	52.9 ± 4.5	0.019 ± 0.081	$(3.82 \pm 1.38) \times 10^{-3}$
$D(d,n)^3\text{He}$	49.7 ± 5.0	0.170 ± 0.087	$(4.24 \pm 1.45) \times 10^{-3}$

Ronald *et al.* also measured the cross section for the $d + d$ reaction using a window-less gas target. [26] The CM energy ranged from 10 to 58.5 keV. Krauss *et al.* used a D^+ beam, while Ronald *et al.* used a D^- beam. The obtained $S(E)$ was parametrized in the form:

$$S = S_0(1 + \alpha E_d), \quad (2.13)$$

where E_d denotes the deuteron incident energy in the laboratory frame. The obtained parameters S_0 and α are summarized in Table 2.2.

In this thesis, the parameters for describing $S(E)$ reported by Ronald *et al.* are used since the uncertainties are less than those reported by Krauss *et al.*

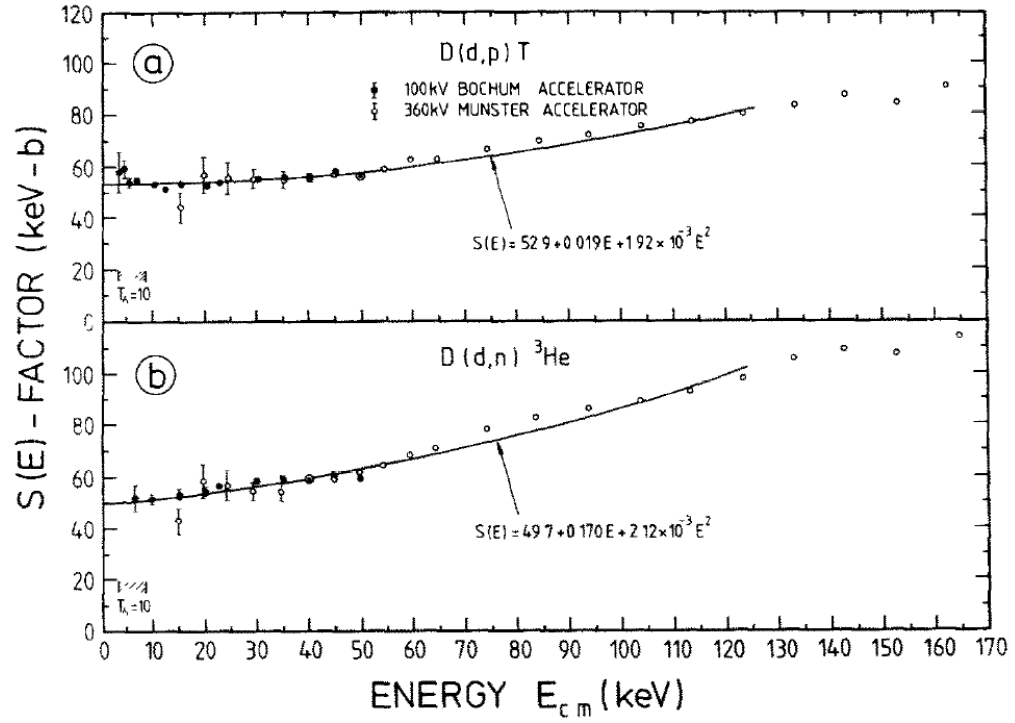


Figure 2.1: Astrophysical S factor $S(E)$ as a function of the CM energy E_{cm} for the D(d,p)T (a) and $\text{D(d,n)}^3\text{He}$ (b) reactions. The solid curve shows the fitted quadratic functions for $E_{\text{cm}} \leq 120$ keV, and the corresponding functions are described in the panels.

Table 2.2: $S(0)$, α parameters for describing $S(E)$ in Equation (2.13) reported by Ronald *et al.* [26]. These parameters are obtained for the $D(d,p)T$ and $D(d,n)^3He$ reactions.

reaction	S_0 (keV·b)	αS_0 (b)
$D(d,p)T$	55.49 ± 0.46	$(9.482 \pm 0.540) \times 10^{-2}$
$D(d,n)^3He$	53.76 ± 0.61	$(1.623 \pm 0.072) \times 10^{-1}$

2.4 Angular distribution

The angular distributions for the $D(d,p)T$ and $D(d,n)^3He$ reactions are described. The angular distribution is expanded by the Legendre polynomials,

$$W(\theta) = 1 + \sum_k a_k(E) P_k(\cos \theta). \quad (2.14)$$

The explicit representation of the Legendre polynomials is

$$P_n(x) = \frac{1}{2^n n!} \frac{d^n}{dx^n} [(x^2 - 1)^n]. \quad (2.15)$$

Because two deuterons in the initial state do not be identified, the angular distribution has a symmetry with respect to $\theta = 90^\circ$, and is expressed only by even n number in Equation (2.14). Krauss [25] gives the a_2 and a_4 fitting the measured cross section as a function of the deuteron emission angle θ in Equation (2.14) with $n \leq 4$. Figure 2.2 shows the a_2 and a_4 parameters as a function of the deuteron incident energy in the laboratory frame E_{lab} . In the present work, maximum center of mass energy of the $d + d$ reaction is about 40 keV. Therefore, since the angular momentum contributing to the reaction is considered to be $L=1$ at the maximum, we employ the following equation to the angular distribution which is the component of Equation (2.14) of $k \leq 2$.

$$W(\theta) \sim 1 + \frac{a_2}{2} (3 \cos^2 \theta - 1) \quad (2.16)$$

Here, a_2 parameter is obtained fitting the measured cross by Krauss for $E=0-60$ keV. The fitting result is summarized in Table 2.3.

TABLE 1
Angular distribution coefficients a_k ^{a)}

$E_{\text{lab}}^{\text{b)}}$ (keV)	D(d, p)T		D(d, n) ³ He	
	a_2	a_4	a_2	a_4
15	0.05 ± 0.04	≤ 0.03	0.11 ± 0.03	≤ 0.04
20	0.14 ± 0.01	0.04 ± 0.03	0.19 ± 0.04	-0.04 ± 0.05
30	0.21 ± 0.01	0.04 ± 0.03	0.35 ± 0.04	0.02 ± 0.05
40	0.23 ± 0.01	0.01 ± 0.03	0.35 ± 0.03	0.00 ± 0.05
50	0.23 ± 0.01	0.03 ± 0.03	0.39 ± 0.03	0.02 ± 0.05
60	0.29 ± 0.01	0.04 ± 0.03	0.42 ± 0.03	0.02 ± 0.02
70	0.31 ± 0.02	0.04 ± 0.03	0.48 ± 0.03	0.03 ± 0.03
80	0.33 ± 0.02	0.06 ± 0.03	0.53 ± 0.02	0.03 ± 0.03
90	0.33 ± 0.02	0.04 ± 0.03	0.55 ± 0.02	0.04 ± 0.02
100	0.36 ± 0.02	0.03 ± 0.02	0.60 ± 0.02	0.01 ± 0.02
110	0.39 ± 0.02	0.06 ± 0.03	0.58 ± 0.02	0.05 ± 0.05
130	0.44 ± 0.03	0.04 ± 0.03	0.63 ± 0.03	0.06 ± 0.05
150	0.45 ± 0.02	0.08 ± 0.03	0.66 ± 0.03	0.07 ± 0.05
170	0.49 ± 0.02	0.08 ± 0.03	0.67 ± 0.03	0.08 ± 0.05
190	0.55 ± 0.02	0.08 ± 0.02	0.73 ± 0.03	0.11 ± 0.05
210	0.54 ± 0.02	0.08 ± 0.02	0.74 ± 0.03	0.10 ± 0.05
230	0.57 ± 0.02	0.11 ± 0.02	0.75 ± 0.03	0.13 ± 0.06
250	0.60 ± 0.02	0.12 ± 0.04	0.78 ± 0.03	0.11 ± 0.06
270	0.60 ± 0.02	0.13 ± 0.02	0.76 ± 0.03	0.13 ± 0.06
290	0.62 ± 0.02	0.11 ± 0.03	0.78 ± 0.03	0.03 ± 0.06
310	0.58 ± 0.02	0.17 ± 0.03	0.69 ± 0.03	0.10 ± 0.07
330	0.67 ± 0.01	0.13 ± 0.02	0.82 ± 0.03	-0.12 ± 0.08

^{a)} One standard deviation error. Runs carried out at the same energy have been averaged.

^{b)} Incident energy.

Figure 2.2: The parameters a_2 and a_4 as a function of the incident deuteron energy in the laboratory frame E_{lab} for the D(d,p)T and D(d,n)³He reactions obtained by Krauss.

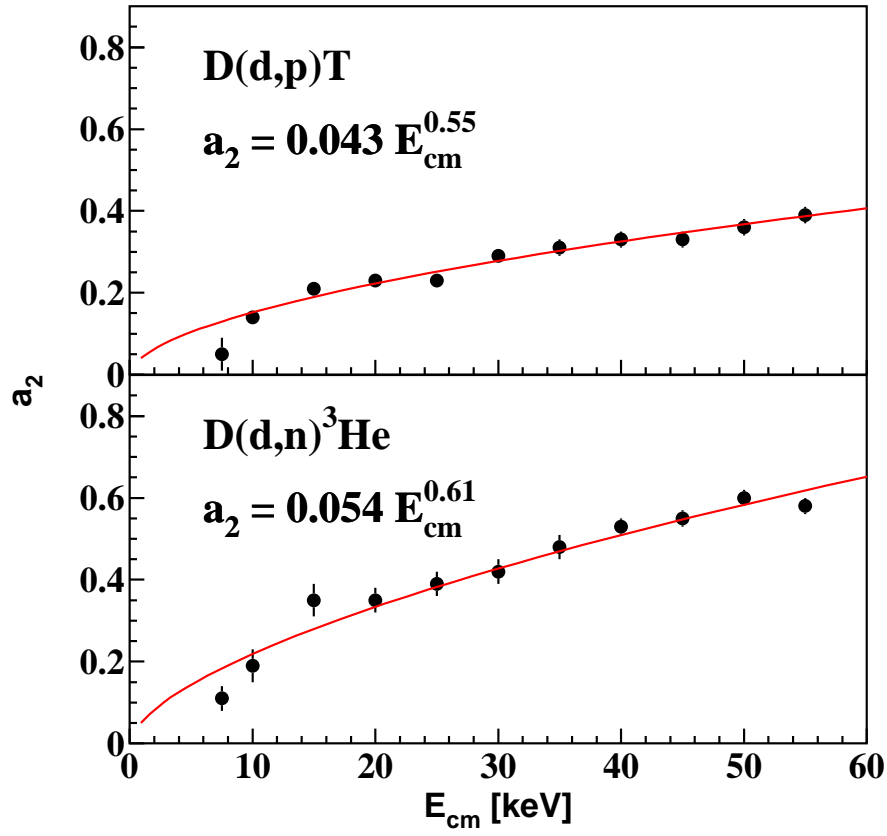


Figure 2.3: The parameter a_2 as a function of the CM energy E_{cm} for the $D(d,p)T$ and $D(d,n)^3\text{He}$ reactions obtained by Krauss. The solid curves show the fitted function to a_2 for $E_{\text{cm}} \leq 60$ keV, and the corresponding representations are described in the panels.

Table 2.3: Fitting result of a_2 parameter reported by Krauss

$$\begin{array}{ll} \text{D(d,p)T} & : a_2 = 0.043 E^{0.55} \\ \text{D(d,n)}^3\text{He} & : a_2 = 0.054 E^{0.61} \end{array}$$

2.5 Kinematics of $d + d$ reaction

In the $d+d$ reaction with CCM, the two deuterons have arbitrary momentum vectors in the laboratory frame, and the kinematics is a little bit complicated as compared with a stationary (fixed) target experiment. The energy spectra and angular distribution in CCM should be calculated by taking into account the actual momenta of the two deuterons. The kinetic energy of the emitted particle and ratio of the solid angle in the laboratory frame to that in the CM frame are described in this section.

2.5.1 Kinetic energy of emitted nuclei

Here, the nuclear reaction $N_1 + N_2 \rightarrow N_3 + N_4$ is considered. It should be noted that both the nuclei N_1 and N_2 have a finite momentum in the laboratory frame. Let us define the O frame in which the momentum vector of N_1 is parallel to the z axis. The momentum of N_i in the O frame is denoted by \vec{P}_i , and the corresponding polar and azimuthal angle is θ_i and ϕ_i , respectively. Apparently, $\theta_1 = 0$ is valid from the definition of the z -axis. The O' frame is the CM one, which moves with velocity $\vec{\beta}$ relative to the O frame, where

$$\begin{aligned} \vec{\beta} &= -\frac{\vec{P}_1 + \vec{P}_2}{m_1 + m_2} \\ &= -\frac{\sqrt{2m_2E_2}}{m_1 + m_2} \left(\sin \theta_2 \cos \phi_2, \sin \theta_2 \sin \phi_2, \cos \theta_2 + \sqrt{\frac{m_1E_1}{m_2E_2}} \right) \end{aligned} \quad (2.17)$$

The m_i stands for the mass of the nucleus N_i , and E_i is the kinetic energy in the O frame. The CM energy E_{CM} is expressed by

$$\begin{aligned} E_{\text{CM}} &\equiv E'_1 + E'_2 \\ &= \frac{m_2 E_1 + m_1 E_2 - 2 \cos \theta_2 \sqrt{m_1 m_2 E_1 E_2}}{m_1 + m_2}. \end{aligned} \quad (2.18)$$

The kinetic energy E'_3 for the N_3 nucleus in the final state in the O' frame can be obtained as

$$E'_3 = \frac{m_4}{m_3 + m_4} (Q + E_{\text{CM}}), \quad (2.19)$$

where the Q is Q-value($m_3 + m_4 - m_1 - m_2$) for the reaction of interest. The E'_3 is also given by the kinetic variables in the O frame as

$$\begin{aligned} E'_3 &= \frac{|\vec{P}_3 + m_3 \vec{\beta}|^2}{2m_3} \\ &= \frac{|\vec{P}_3|^2}{2m_3} + \frac{1}{2} m_3 |\vec{\beta}|^2 + \vec{P}_3 \vec{\beta} \\ &= E_3 + \frac{1}{2} m_3 |\vec{\beta}|^2 + \sqrt{2m_3 E_3} |\vec{\beta}| \cos \theta_\beta \end{aligned} \quad (2.20)$$

Here, the angle between \vec{P}_3 and $\vec{\beta}$ is θ_β . Equations (2.19) and (2.20) give an equation for E_3 :

$$E_3 = E'_3 \left\{ \sqrt{1 - \gamma^2 \sin^2 \theta_\beta} - \gamma \cos \theta_\beta \right\}^2 \quad (2.21)$$

where

$$\gamma^2 = \frac{\frac{1}{2} m_3 |\vec{\beta}|^2}{E'_3} \quad (2.22)$$

Now, the energy E_3 for the N_3 nucleus emitted in the direction (θ_3, ϕ_3) has been obtained.

When the momentum direction of each nucleus N_i is given in $(\theta_i^{\text{lab}}, \phi_i^{\text{lab}})$ in the laboratory frame, the momentum of each can be obtained rotating the z axis being parallel to the momentum direction of N_1 . The rotation matrix R corresponding to

the three-dimensional rotation from the laboratory frame to the O frame is described:

$$R = \begin{bmatrix} \cos \theta_1^{\text{lab}} \cos \phi_1^{\text{lab}} & \cos \theta_1^{\text{lab}} \sin \phi_1^{\text{lab}} & -\sin \theta_1^{\text{lab}} \\ -\sin \phi_1^{\text{lab}} & \cos \phi_1^{\text{lab}} & 0 \\ \sin \theta_1^{\text{lab}} \cos \phi_1^{\text{lab}} & \sin \theta_1^{\text{lab}} \sin \phi_1^{\text{lab}} & \cos \theta_1^{\text{lab}} \end{bmatrix} \quad (2.23)$$

Using the R matrix, the relation between (θ_i, ϕ_i) and $(\theta_i^{\text{lab}}, \phi_i^{\text{lab}})$ are given as

$$\theta_i = \cos^{-1} \left\{ \sin \theta_1^{\text{lab}} \sin \theta_i^{\text{lab}} \cos (\phi_i^{\text{lab}} - \phi_1^{\text{lab}}) + \cos \theta_1^{\text{lab}} \cos \theta_i^{\text{lab}} \right\}, \quad (2.24)$$

and

$$\phi_i = \tan^{-1} \left\{ \frac{\sin \theta_i^{\text{lab}} \sin (\phi_i^{\text{lab}} - \phi_1^{\text{lab}})}{\cos \theta_1^{\text{lab}} \sin \theta_i^{\text{lab}} \cos (\phi_i^{\text{lab}} - \phi_1^{\text{lab}}) - \sin \theta_1^{\text{lab}} \cos \theta_i^{\text{lab}}} \right\}. \quad (2.25)$$

This relation and Equation (2.21) give the energy of the N_3 nucleus emitted at the direction $(\theta_3^{\text{lab}}, \phi_3^{\text{lab}})$ in the laboratory frame.

Let us consider the $d + d$ reaction, where the deuteron d_1 , moving along the $+z$ axis with a kinetic energy of $E_1 = 20$ keV in the laboratory frame, collides with the deuteron d_2 , moving at the direction (θ_2, ϕ_2) with $E_2 = 20$ keV. Figure 2.4 shows the kinetic energy of the proton emission energy E_p , which is detected at the polar angle $\theta^{\text{lab}} = 146^\circ$ and azimuthal angle $\phi^{\text{lab}} = 0^\circ$, as a function of θ_2 and ϕ_2 . The E_p is calculated as a function of θ_2 for $\phi_2 = 0^\circ, 90^\circ$, and 180° . Even if θ_2 is the same, E_p for $\theta_2 = 0^\circ$ is larger than that for $\phi_2 = 180^\circ$. This is because the direction of the motion of the center of mass system depends on ϕ_2 . When the center of mass system goes to the detected direction ($\phi_2 = \phi^{\text{lab}}$), E_p becomes bigger. While E_p becomes smaller when the direction is opposite.

2.5.2 Solid angle ratio

The differential cross section in the laboratory frame $(d\sigma/d\Omega)^{\text{lab}}$ can be described by the cross section in the CM frame $(d\sigma/d\Omega)^{\text{cm}}$. Here, the $+z$ and $-z$ axes in the CM frame are parallel to the momentum directions of N_1 and N_2 . The (θ'_i, ϕ'_i) in the O'

frame is express by the $(\theta_i^{\text{cm}}, \phi_i^{\text{cm}})$ in the CM frame:

$$\theta_i^{\text{cm}} = \cos^{-1} \{ \sin \theta'_1 \sin \theta'_i \cos (\phi'_i - \phi'_1) + \cos \theta'_1 \cos \theta'_i \}, \quad (2.26)$$

$$\phi_i^{\text{cm}} = \tan^{-1} \left\{ \frac{\sin \theta'_i \sin (\phi'_i - \phi'_1)}{\cos \theta'_1 \sin \theta'_i \cos (\phi'_i - \phi'_1) - \sin \theta'_1 \cos \theta'_i} \right\}. \quad (2.27)$$

$(d\sigma/d\Omega)^{\text{lab}}$ is expressed with the ratio of solid angles between the CM and laboratory frames $(d\Omega^{\text{cm}}/d\Omega^{\text{lab}})$ as

$$\left(\frac{d\sigma}{d\Omega} \right)^{\text{lab}} = \left(\frac{d\sigma}{d\Omega} \right)^{\text{cm}} \left(\frac{d\Omega^{\text{cm}}}{d\Omega^{\text{lab}}} \right). \quad (2.28)$$

The formula can be modified as

$$\left(\frac{d\sigma}{d\Omega} \right)^{\text{lab}} = \left(\frac{d\sigma}{d\Omega} \right)^{\text{cm}} \left(\frac{d\Omega^{\text{cm}}}{d\Omega^{O'}} \right) \left(\frac{d\Omega^{O'}}{d\Omega^O} \right) \left(\frac{d\Omega^O}{d\Omega^{\text{lab}}} \right). \quad (2.29)$$

Since the solid angle is the same between the laboratory and O frames, and between the O' and CM frames,

$$\left(\frac{d\sigma}{d\Omega} \right)^{\text{lab}} = \left(\frac{d\sigma}{d\Omega} \right)^{\text{cm}} \left(\frac{d\Omega^{O'}}{d\Omega^O} \right). \quad (2.30)$$

In general, the ratio of solid angles in the two frames is described [27] as

$$\begin{aligned} \left(\frac{d\Omega^{O'}}{d\Omega^O} \right) &= \frac{E}{E'} [\cos \theta \cos \theta' + \sin \theta \sin \theta' \cos(\phi - \phi')] \\ &= \frac{E}{E'} \cos \delta. \end{aligned} \quad (2.31)$$

where δ denotes the angle between \vec{P} and \vec{P}' . Now, the ratio of solid angles between the laboratory and CM frames is given in Equation 2.31 and relations between (θ, θ') and (ϕ, ϕ') are calculated from Equation (2.24),(2.25),(2.26),(2.27).

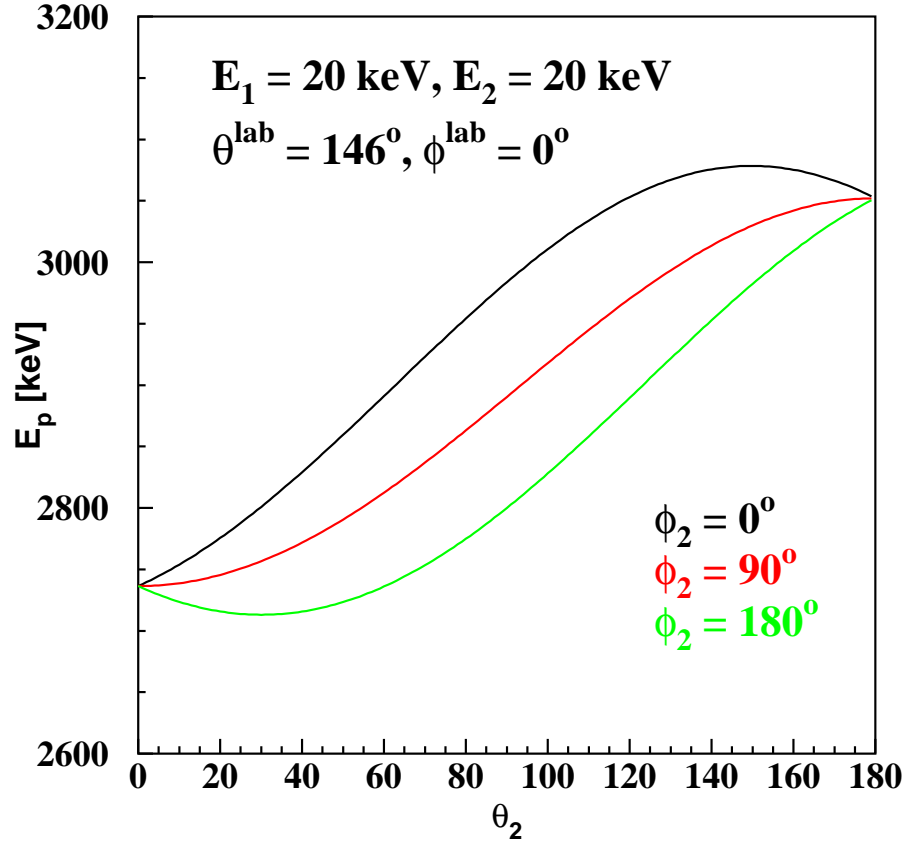


Figure 2.4: Proton energy E_p emitted from $d_1 + d_2 \rightarrow p + t$ reaction as a function of polar angle of d_2 , θ_2 for three azimuthal angle $\phi_2 = 0^\circ$ (black), 90° (red), and 180° (green). The kinetic energy of d_1 and d_2 is both 20 keV. The moving direction of d_1 is fixed to $+z$ axis direction. The proton is detected at the polar angle $\theta^{\text{lab}} = 146^\circ$ and azimuthal angle $\phi^{\text{lab}} = 0^\circ$.

Chapter 3

Coulomb scattering in matter

In CCM, Coulomb scattering between metal atom and deuteron plays a very important role. Since the nuclei in the matter have bound electrons, it is necessary to use the cross section of Coulomb scattering which includes screening effect. Coulomb scattering in a matter is described below.

3.1 Differential Cross section

A screened potential $V(r)$ between two atoms of charge Z_1 and Z_2 is usually expressed by the following formula with a distance r ,

$$V(r) = \frac{Z_1 Z_2 e^2}{r} \Phi(r). \quad (3.1)$$

Here $\Phi(r)$ is called screening function and represents the decrease of the potential. $\Phi(r)$ depends on the screening model, examples of which are shown below.

$$\text{Bohr : } \Phi = \exp(-x_B) \quad (3.2)$$

$$\text{Moliere : } \Phi = 0.35 \exp(-0.3x_M) + 0.55 \exp(-1.2x_M) + 0.1 \exp(-6.0x_M) \quad (3.3)$$

$$\begin{aligned} \text{ZBL : } \Phi = & 0.1818 \exp(-3.2x_Z) + 0.5099 \exp(-0.9423x_Z) \\ & + 0.2802 \exp(-0.4028x_Z) + 0.02817 \exp(-0.2016x_Z) \end{aligned} \quad (3.4)$$

Here, x_B , x_M , x_Z are reduced length obtained by dividing r by screening length a_B , a_M , a_Z ,

$$\text{Bohr : } a_B = \frac{a_0}{\left(Z_1^{2/3} + Z_2^{2/3}\right)^{1/2}}, \quad (3.5)$$

$$\text{Moliere : } a_M = \frac{0.8853 a_0}{\left(Z_1^{1/2} + Z_2^{1/2}\right)^{2/3}}, \quad (3.6)$$

$$\text{ZBL : } a_Z = \frac{0.8853 a_0}{Z_1^{0.23} + Z_2^{0.23}}, \quad (3.7)$$

with Bohr radius $a_0 = 0.529 \text{ \AA}$. The Bohr and Moliere model use a classical charge distribution that does not consider the shell structure of electrons. The ZBL model uses a charge state of a Hartree-Fock atom in solid state. The potentials between indium and hydrogen for each screening model as a function of r are shown in Figure 3.1. The black, red, green and blue curves show Coulomb potential for non-screening, Bohr, ZBL and Moliere model, respectively. The dot lines show the screening length. The screening is lager in order of the Bohr, Moliere and ZBL model.

In general, a scattering cross section for the potential described in Equation (3.1) cannot be obtained analytically. Therefore, the cross section is calculated from the classical scattering theory. Solving the scattering by the central force of two particles, we can obtain the following equation.

$$\Theta = \pi - 2 \int_{r_0}^{\infty} [r\phi(r)]^{-1} dr \quad (3.8)$$

$$\phi(r) = \left[\frac{r^2}{p^2} - 1 - \frac{r^2 V(r)}{Ep^2} \right]^{\frac{1}{2}} \quad (3.9)$$

Here, Θ is the scattering angle in the center-of-mass (CM) system, p is the impact parameter of the collision, E is the energy of the CM system, r_0 , which is the positive root of the Equation (3.9), is the closest distance between the two particles. Since the Equation (3.9) contains a singular point at the lower end of the integral region, it takes not short time to obtain sufficient accuracy with simple numerical integration. For this reason, conversion and approximation of expressions are performed, and the calculation speed is improved while maintaining the accuracy.

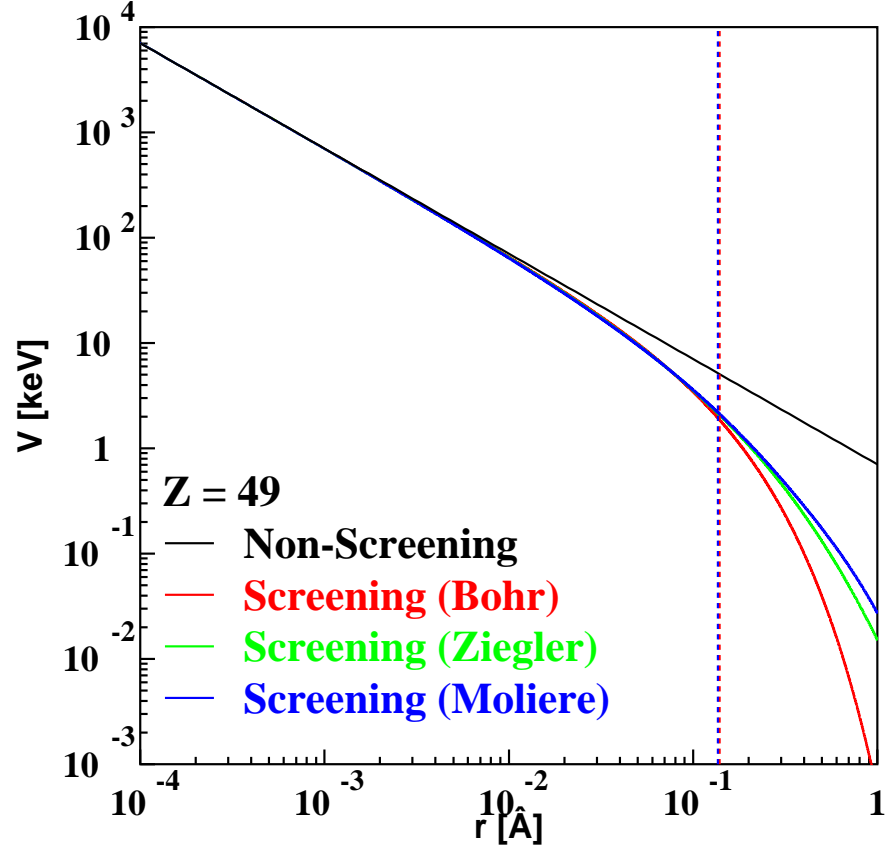


Figure 3.1: Coulomb potentials between indium and hydrogen for some screening model

For the Bohr screening function, singularity can be eliminated by deforming the Equation (3.9) as follows [28].

$$\Theta = \pi - \frac{2p}{a} \int_0^{z_0} y_0^{-1/2} dz + \frac{2p}{a} \int_0^{z_0} \left(y_0^{-1/2} - y^{-1/2} \right) dz \quad (3.10)$$

Here,

$$\begin{aligned} y &= 1 - (p/a)^2 z^2 - (b/a)z \exp(-1/z), \\ y_0 &= 1 - (p/a)^2 z_0^2 - (b/a)z_0 \exp(-1/z_0), \\ z &= a/r, \\ z_0 &= a/r_0. \end{aligned}$$

The second term of the Equation (3.10) can be integrated analytically, and we can obtain,

$$\Theta = 2 \cot^{-1} \left[\frac{2p/b}{\exp(-1/z_0)} \right] + \frac{2p}{a} \int_0^{z_0} \left(y_0^{-1/2} - y^{-1/2} \right) dz. \quad (3.11)$$

The Equation (3.11) is a simple function with no singularity, and the integration can be executed with a sufficient accuracy with the Gaussian quadrature method, etc. In this study, numerical integration was performed using the Gauss-Kronrod quadrature formula.

Biersack and Haggmark obtained an approximate expression of the scattering angle by adding a model-dependent correction term [29]. The Figure 3.2 represents the scattering of two particles in the CM system. M_1 and M_2 are mass of the particles, Θ is a scattering angle, p is an impact parameter, r_0 is a distance of closest approach, ρ_1 and ρ_2 are radiuses of curvature and δ_1 and δ_2 are correction terms. As can be seen from the figure, Θ can be expressed as

$$\cos \frac{\Theta}{2} = \frac{\rho + p + \delta}{\rho + r_0}. \quad (3.12)$$

Here,

$$\begin{aligned} \rho &= \rho_1 + \rho_2, \\ \delta &= \delta_1 + \delta_2. \end{aligned}$$

We define following with a screening length a ,

$$B \equiv p/a, \quad R_0 \equiv r_0/a, \quad R_c \equiv \rho/a, \quad \Delta \equiv \delta/a.$$

We can obtain

$$\cos \frac{\Theta}{2} = \frac{B + R_C + \Delta}{R_0 + R_C}. \quad (3.13)$$

The Equation (3.13) is called Magic Formula.

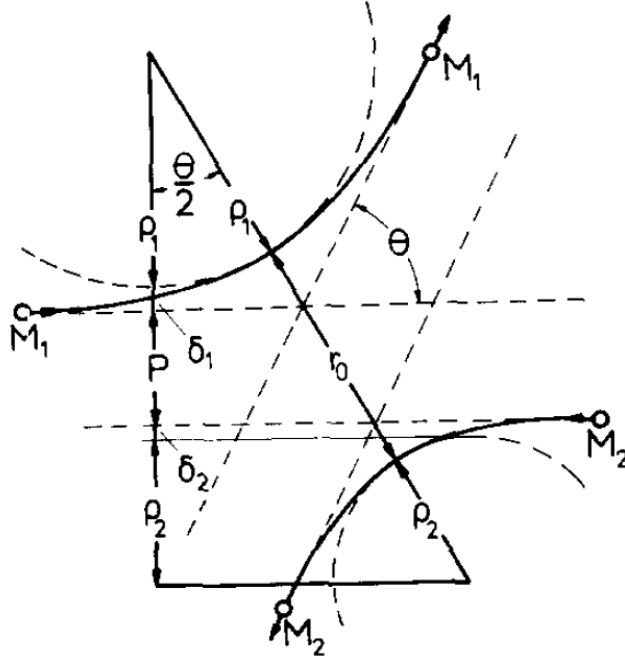


Figure 3.2: Particle trajectories in CM system.

From a fitting convenience and a restriction that the Equation (3.13) corresponds to the Rutherford scattering at the high energy limit, Δ is determined to the following with model-dependent correction coefficients C_1 – C_5 .

$$\Delta = A \frac{R_0 - B}{1 + G} \quad (3.14)$$

Here,

$$A = 2\alpha\epsilon B^\beta, \quad G = \gamma[(1 + A^2)^{1/2} - A]^{-1}, \quad (3.15)$$

and

$$\alpha = 1 + C_1 \epsilon^{-1/2}, \quad (3.16)$$

$$\beta = \frac{C_2 + \epsilon^{1/2}}{C_3 + \epsilon^{1/2}}, \quad (3.17)$$

$$\gamma = \frac{C_4 + \epsilon}{C_5 + \epsilon}. \quad (3.18)$$

Ziegler *et al.* calculated the correction coefficient from the comparison of the numerical integration result of the Equation (3.9) to the Magic formula. The result is summarized in Table 3.1.

Table 3.1: Correction coefficients of Magic formula for Moliere and ZBL screening model

Coefficient	Moliere	ZBL
C_1	0.6743	0.99229
C_2	0.009611	0.0011615
C_3	0.005175	0.007122
C_4	10.00	9.3066
C_5	6.314	14.813

As a result, we can obtain the differential scattering cross section ($d\sigma/d\Omega$) by

$$\frac{d\sigma(\Theta)}{d\Omega} = -\frac{pdp}{\sin \Theta d\Theta}. \quad (3.19)$$

The calculated differential cross section between indium and hydrogen with a CM energy of 20 keV is shown in Figure 3.3. The black, red, green and blue curve show that for non-screening(Rutherford), Bohr, ZBL and Moliere model, respectively. Although the cross section of large-angle scattering ($\Theta \sim \pi$) decreases by only a few tenth percent with respect to the non-screening, that of small-angle scattering ($\Theta \leq 0.01$) decreased more than two orders of magnitude. In the comparison between the screening models, the cross section of the small-angle scattering is strongly screened in the order of Bohr, ZBL and Moliere. The difference in large-angle scattering cross section between Bohr and Moliere model is small, it is about 5 ~ 10 % in the range

of $\Theta \geq 0.5$. In contrast, that of ZBL model is about 40 % smaller than that of Bohr model in the same range.

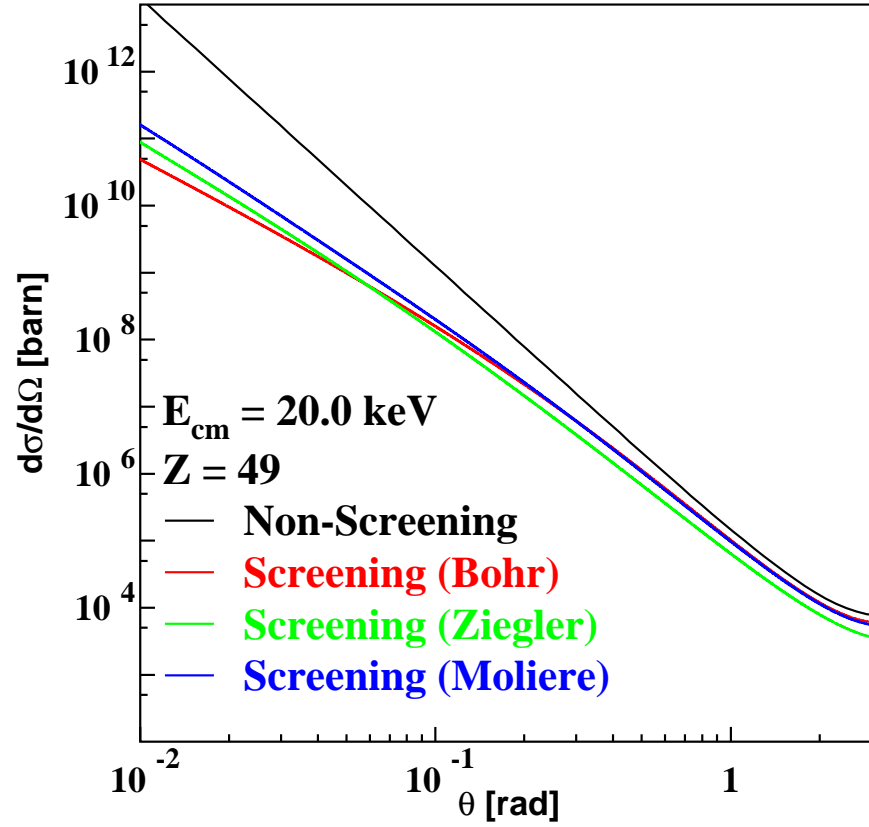


Figure 3.3: Differential cross section of Coulomb scattering between indium and hydrogen with a CM energy of 20 keV. The black, red, green and blue curve show that for non-screening(Rutherford), Bohr, ZBL and Moliere model, respectively.

Chapter 4

Cooperative colliding mechanism

This chapter serves to understand Cooperative colliding mechanism (CCM) which is a nuclear reaction process unique to a molecular beam. For that purpose, we performed simulation of the CCM.

4.1 Reaction Process

Consider the case where a deuteron molecular beam D_2^+ strikes a target composed of atoms X. While a molecular ion D_2^+ is accelerated and transported, deuterons d_1 and d_2 are bound in the molecule. Therefore, the velocity and the direction of motion of each deuteron are the same: both deuterons are incident on the target while maintaining that state. After that, d_1 and d_2 go straight ahead while losing their kinetic energy due to the interaction with electrons, and eventually cause a Coulomb scattering with atom X. As a result, the traveling direction of d_1 or d_2 changes. If there is a partner deuteron, the $d + d$ reaction occurs according to the probability depending on their relative momentum. When scattered backward by Coulomb scattering, two deuterons cause a head-on collision like a colliding beam, so we named it Cooperative Colliding Mechanism (CCM). The CCM is not only for

the deuteron molecule. A generalized diagram of the CCM has been already shown in Figure 1.3. The nucleus B in the (A+B) molecule scatters with a host atom X, and changes his direction and collides with the nucleus A. Thus, in the CCM, the two nuclei causing the nuclear reaction $A+B \rightarrow C+D$. It should be stressed that the nuclei that are both contained in the same molecule make a nuclear reaction.

4.2 Thin-target yield

Before more strict calculation, we simplify the situation and consider rough reaction yield. First, consider the thin-target yield of the CCM caused by a D_n^+ beam in a thin film target. We assume that the film is sufficiently thin so that only one among n deuterons is scattered. Furthermore, we ignore the energy change of deuteron due to Coulomb scattering. Then, an energy of the center-of-mass system of two deuterons is described as

$$E_{\text{cm}} \sim E_0(1 - \cos \theta) \quad (4.1)$$

Here, E_0 and θ are, respectively, the incident energy and scattering angle of a deuteron in the lab system. This assumption is not correct for light mass targets because the energy change due to Coulomb scattering increases as the mass of the target nucleus is closer to deuteron, but it is roughly correct for heavy mass targets. The CCM yield Y_{Thin} in the thin film target of thickness dx is calculated by the following formula using the cross section of Coulomb scattering $(d\sigma/d\Omega)_C$ and the cross section of $d+d$ reaction $\sigma_{dd}(E_{\text{cm}})$.

$$Y_{\text{Thin}}dx = nC_2\rho_d\rho_m dx \int \sigma_{dd}(E_{\text{cm}}) \left(\frac{d\sigma}{d\Omega} \right)_C d\Omega \quad (4.2)$$

Where ρ_m is the number density of the target atoms and ρ_d is the actual deuteron target density calculated from the probability that in which a specific partner deuteron is present at the scattering destination as described below.

$$\rho_d = \frac{1}{4\pi r_{dd}^2} \quad (4.3)$$

Here, r_{dd} is the interatomic distance in D_n^+ . Note that the unit of ρ_m is cm^{-3} , whereas the unit of ρ_d is cm^{-2} . nC_2 represents the number of combinations of scattered deuterons and other deuterons. We used an interatomic distance $r_{dd} = 0.93 \pm 0.02 \text{ \AA}$ for D_3^+ which is determined from a Coulomb breakup experiment by Jing-wei *et al.* Using that value, ρ_d is calculated as

$$\rho_d = 9.2 \times 10^{14} \text{ cm}^{-2}. \quad (4.4)$$

As mentioned in § 3 a Coulomb scattering in matter requires the screening effect to be taken into consideration. In the expression (4.2), E_{cm} dependency of σ_{dd} is very strong and small-angle scattering can be ignored because of its small E_{cm} . Figure 4.1 shows the ratio of the total cross section of the large-angle scattering ($\theta \geq 90^\circ$) for the Bohr, Moliere and ZBL screening model to the non-screening (Rutherford) as a function of the CM energy. Using the ratio, R , the expression (4.2) can be approximated as

$$Y_{\text{Thin}} dx = nC_2 \rho_d \rho_m R dx \int \sigma_{dd}(E_{\text{cm}}) \left(\frac{d\sigma}{d\Omega} \right)_R d\Omega, \quad (4.5)$$

where, $(d\sigma/d\Omega)_R$ is a cross section of the Rutherford scattering;

$$\left(\frac{d\sigma}{d\Omega} \right)_R = \left(\frac{Z_1 Z_2 e^2}{16\pi\epsilon_0 E_0} \right)^2 \frac{1}{\sin^4(\Theta/2)}. \quad (4.6)$$

Here, Θ is a scattering angle in the CM system, When the mass of the metal atom is greatly larger than that of the deuteron, Θ can be approximated to θ , and the Equation (4.2) can be integrated as

$$Y_{\text{Thin}} dx = nC_2 \frac{8\pi\rho_d\rho_m SR}{E_0^3} \left(\frac{Z_1 Z_2 e^2}{16\pi\epsilon_0} \right)^2 dx \frac{C^3 + 3C^2 + 6C + 6}{2C^4} e^{-C} \quad (4.7)$$

given by

$$C \equiv \frac{-\alpha}{\sqrt{2E_0}} = \frac{-31.397}{\sqrt{2E_0}}. \quad (4.8)$$

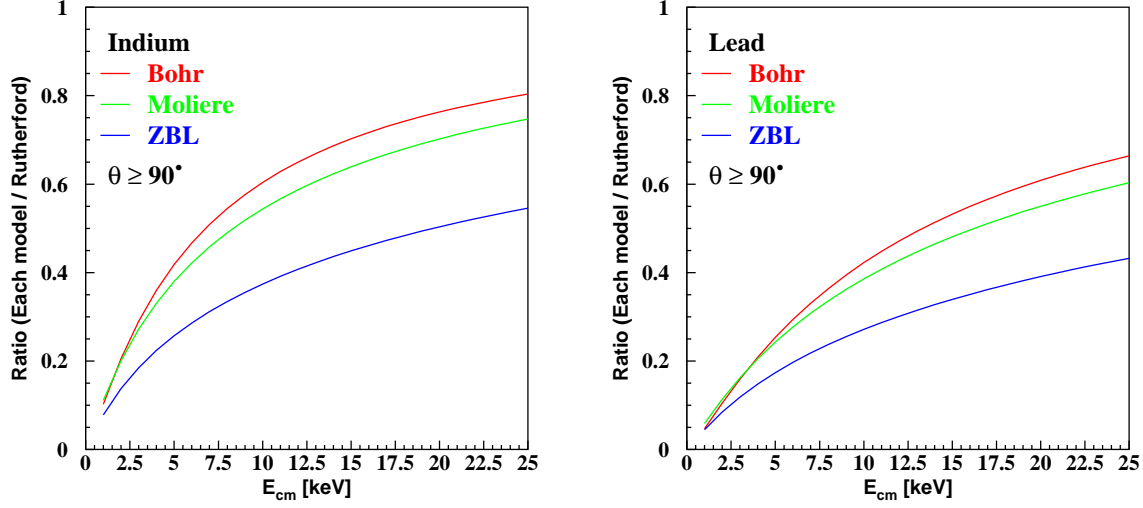


Figure 4.1: The ratio of the total cross section of the large-angle ($\theta \geq 90^\circ$) scattering for the Bohr, Moliere and ZBL screening model to the non-screening (Rutherford).

4.3 Thick-target yield

The target of the actual experiment has a finite thickness, and the measured yield is a thick-target yield which corresponds to the integration of the thin-target yield with respect to the thickness. For the integral region, the actual target thickness is used if the energy of the beam is high and the beam passes through the target, while the range is used if the beam stops halfway. Since the reaction target of the CCM is a partner deuteron in the same molecule, its position relationship collapses and the distance increases due to scattering as deuterons go into the substance. Due to this effect, the CCM occurs at most 200 Å from the target surface. And the substantial deuteron density reduction is overwhelmingly faster than the $d + d$ cross section reduction due to energy loss.

ρ_d is modified as a function of x as follows when we define the effective distance between deuterons in depth x as $r_{dd}(x)$.

$$\rho_d \rightarrow \rho_d(x) = \frac{1}{4\pi r_{dd}^2(x)} \quad (4.9)$$

Here, $r_{dd}(0) = r_{dd}$, and $\rho_d(0) = \rho_d$. Thick target yield, Y_{Thick} is expressed as

$$Y_{\text{Thick}} = \int_0^\infty \left(\frac{r_{dd}}{r_{dd}(x)} \right)^2 Y_{\text{Thin}} dx \quad (4.10)$$

Since we know that CCM is occurring on the extreme surface of the target, neglecting the energy loss in the target, Y_{Thin} which does not depend on x is expressed as follows.

$$Y_{\text{Thick}} = r_{dd}^2 Y_{\text{Thin}} \int_0^\infty \left(\frac{1}{r_{dd}(x)} \right)^2 dx \quad (4.11)$$

As the deuterons proceed the $r_{dd}(x)$ changes due to the change in the average distance between deuterons due to multiple scattering to a small angle. According to reference [30], the horizontal extent after traveling the distance $z = x\rho_m \text{ g cm}^{-2}$ is expressed as

$$\langle y^2 \rangle_{\text{av}} = \frac{\Theta_s^2 z^3}{6} \quad (4.12)$$

Here, Θ_s is

$$\Theta_s^2 = \left(\frac{E_s}{\beta c p} \right)^2 \frac{1}{X_0} \quad (4.13)$$

given by

$$E_s = \left(\frac{4\pi}{\alpha} \right)^{1/2} m_e c^2 = 21 \times 10^6 \text{ eV}, \text{ and} \quad (4.14)$$

$$\frac{1}{X_0} = 4\alpha \frac{N_A}{A} Z(Z+1) r_e^2 \ln(183Z^{-1/3}). \quad (4.15)$$

With $\langle y^2 \rangle_{\text{av}}$, $r_{dd}(x)$ is expressed as

$$r_{dd}(x) = r_{dd} + \frac{\sqrt{\langle y^2 \rangle_{\text{av}}}}{\rho_m}. \quad (4.16)$$

Performing the integration of the Equation (4.11), we obtain analytical form of the Y_{Thick} as

$$Y_{\text{Thick}} = Y_{\text{Thin}} \frac{4\pi}{9\sqrt{3}\rho_m} \left(\frac{6\rho_m^2 r_{dd}^2 (2E_0)^2 X_0}{E_s^2} \right)^{1/3}. \quad (4.17)$$

The calculation generally reproduce the experiment result qualitatively. However, the dependency of the interatomic potential is not incorporated into the change of the r_{dd} . Therefore, in order to perform more accurate calculation, Monte Carlo calculation is performed.

4.4 Realistic calculation

From now on, the CCM is modeled and the reaction yield and energy spectrum are calculated more precisely. In conducting calculations, the CCM can be thought as follows. Consider two deuterons d_i and d_j contained in the same molecule in D_2^+ or D_3^+ . The numbers of the combination of i and j are one for D_2^+ and three for D_3^+ . We assume that the distance between d_i and d_j is a fixed value determined by the binding potential between atoms and let its length be r_{dd} . At that time, d_j exists somewhere in the sphere shell $S(r_{dd})$ of the radius r_{dd} centered on d_i . If the position of d_j is uniformly distributed on the spherical shell, $S(r_{dd})$ can be regarded as a membrane of deuteron. The deuteron surface density $\rho_d(r_{dd})$ at that time is expressed by the following formula.

$$\rho_d(r_{dd}) = \frac{1}{4\pi r_{dd}^2} \quad (4.18)$$

$d + d$ reaction by the CCM is caused by d_i colliding with this membrane made by d_j . Therefore, if we can know the relative motion of d_i and the spherical shell at the time of collision, we can calculate the yield using the cross section of $d + d$ reaction.

Specifically, first of all, we calculated the trajectory of deuterons in the substance, using the Coulomb scattering cross section shown in § 3, § 4.4.1. After that, we determined the collision point of deuteron with § 4.4.2 and calculated the yield of $d + d$ reaction with § 4.4.3.

4.4.1 Trajectory calculation

A deuteron on the metal travel straight while receiving energy loss by electrons until scattering occurs with a metal atom. When it causes elastic scattering with the metal atom, it changes its traveling direction. These processes continue until the deuteron becomes at rest or comes out of the target. The trajectory of the deuteron formed by the scattering was calculated using a Monte Carlo Method.

In other words, we advance the deuteron by a small distance dx , and calculate the scattering and energy loss every time to create the trajectory. Actual calculation is performed in the following flow. First, a small distance dx is determined so that the scattering probability dP becomes uniform at each step. Next, we advance the deuteron by $dx/2$ and give an energy loss due to electrons the value of which was indicated by § 5.4.1. Then it is decided whether the deuteron scatters with a metal atom according to probability dP . In the case of scattering, the scattering angle is determined and the energy loss due to scattering is applied by changing the direction. If scattering does not occur, the above procedure is not executed. After that, we advance the deuteron again by $dx/2$, give energy loss due to electrons, and return to the determination of the first dx . The flow of calculation is shown in Figure 4.2. This calculation was performed for two or three deuterons at the same time for D_2^+ and D_3^+ , respectively. The calculations were terminated when the intervals exceeded 2 nm in all combinations. This is equivalent to a situation in which the deuterons constituting D_2^+ or D_3^+ are scattered and the distance expands and the probability of collision is very low. Details of each item are shown below.

Step length

In the trajectory calculation, a deuteron travels through the metal with a small distance of dx . One step is corresponding to the distance of dx . The length of each step was decided so that the scattering probability becomes a constant value in all the steps. When the deuteron travels through the metal by a distance of dx_n , it causes elastic scattering with metal atoms with probability dP_n represented by the following formula.

$$dP_n = \rho_m dx_n \sigma(E_n)_{\text{pm}} \quad (4.19)$$

$$\sigma(E_n)_{\text{pm}} = 2\pi \int_{\Theta_{\min}}^{\pi} \left(\frac{d\sigma(E_n)}{d\Omega} \right)_{\text{pm}} \sin \Theta d\Theta \quad (4.20)$$

Here, Θ is the scattering angle with respect to the direction of travel in the center-of-mass (CM) system, E_n is the energy at the n th step in the CM system for deuteron and metal atom, ρ_m is the number density of metal atom. $(d\sigma(E_n)/d\Omega)_{\text{pm}}$ is a differential cross section for Coulomb scattering which is described in § 3. $\sigma(E_n)_{\text{pm}}$ is a total cross section of Coulomb scattering ignoring small angle scattering less than

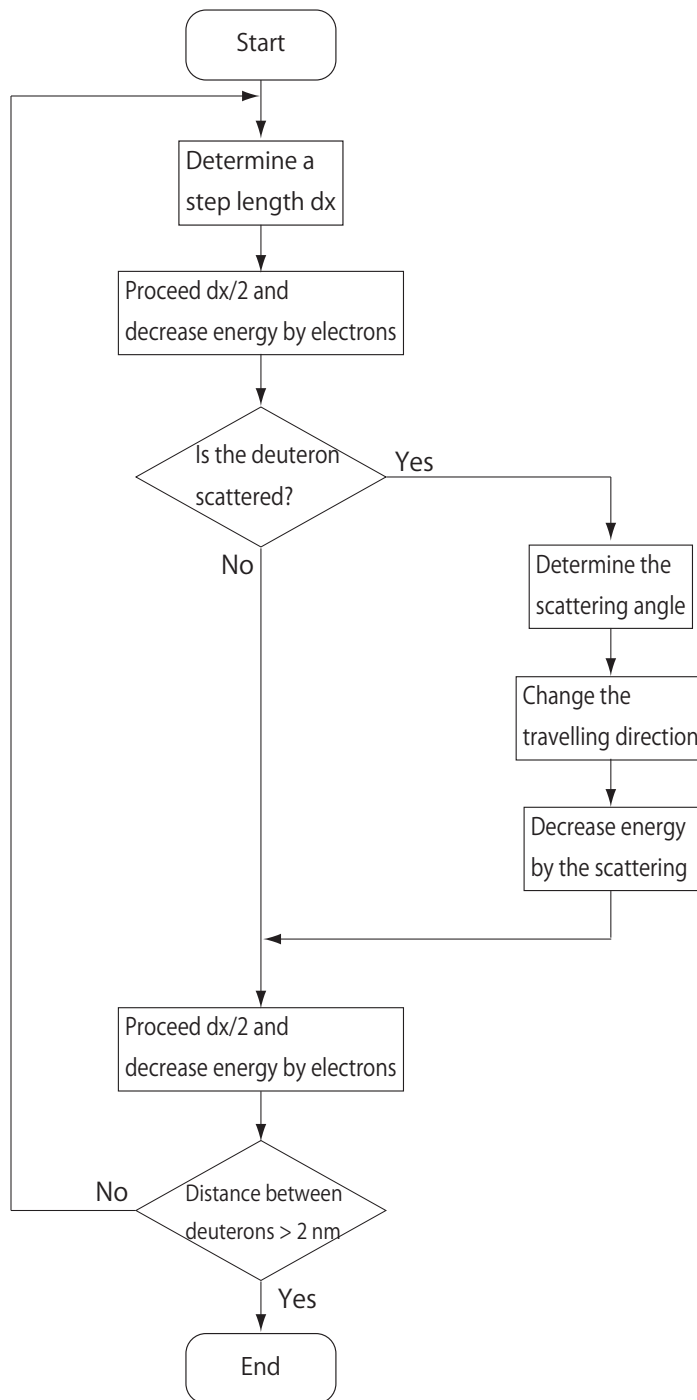


Figure 4.2: Flowchart for calculation of deuteron trajectory in metal.

Θ_{\min} . In Coulomb scattering, since the forward scattering cross section diverges, it is necessary to set the minimum scattering angle in order to determine the total cross section. When dP_n is a constant value dP in all steps, dx_n is expressed by the following equation.

$$dx_n = \frac{dP}{\rho_m \sigma(E_n)_{\text{pm}}} \quad (4.21)$$

Scattering angle

Consider the method of determining the scattering angle. Define impact parameter that realizes scattering to Θ_{\min} as $p_{\max}(E_n)$. We deform and integrate the Equation (3.19) to obtain the following relationship.

$$\sigma(E_n)_{\text{pm}} = \pi p_{\max}^2(E_n) \quad (4.22)$$

This coincides with the radius of the circle whose radius is $p_{\max}(E_n)$. In Coulomb scattering, the smaller the impact parameter, the larger the scattering angle. In other words, scattering to $\Theta \geq \Theta_{\min}$ is caused by a deuteron entering into the circle of radius $p_{\max}(E_n)$. Since the incident position of the deuteron is considered to be uniform, Θ and Φ can be determined by generating random numbers uniformly distributed in the circle. Random numbers uniformly distributed within the radius r_{\max} are generated using the two uniform random numbers R $[0, 1]$ and ϕ $[0, 2\pi]$ as follows.

$$x = r_{\max} \sqrt{R} \cos \phi \quad (4.23)$$

$$y = r_{\max} \sqrt{R} \sin \phi \quad (4.24)$$

Change direction

The incoming deuteron scattered by a metal atom changes the direction in (Θ, Φ) with respect to the direction before scattering. The scattering angle (Θ, Φ) in the CM system is related to the scattering angle (θ, ϕ) in the Lab system by the following

equation.

$$\tan \theta = \frac{\sin \Theta}{\cos \Theta + m_p/m_m} \quad (4.25)$$

$$\Phi = \phi \quad (4.26)$$

Here, m_p and m_m are the masses of the incident deuteron and metal atom.

Changes in the direction of the deuteron can be made using Rodrigues' rotation formula. Rodrigues' rotation formula rotates the angle α with the unit vector $\vec{n} = [n_1, n_2, n_3]$.

$$R(\vec{n}, \alpha) = \begin{bmatrix} \cos \alpha + n_1^2(1 - \cos \alpha) & n_1 n_2(1 - \cos \alpha) - n_3 \sin \alpha & n_1 n_3(1 - \cos \alpha) + n_2 \sin \alpha \\ n_2 n_1(1 - \cos \alpha) + n_3 \sin \alpha & \cos \alpha + n_2^2(1 - \cos \alpha) & n_2 n_3(1 - \cos \alpha) - n_1 \sin \alpha \\ n_3 n_1(1 - \cos \alpha) - n_2 \sin \alpha & n_3 n_2(1 - \cos \alpha) + n_1 \sin \alpha & \cos \alpha + n_3^2(1 - \cos \alpha) \end{bmatrix} \quad (4.27)$$

Define the direction of the incident deuteron before scattering as \vec{v}_p , and define a unit vector \vec{n}_\perp that is perpendicular to a parallel unit vector \vec{n}_\parallel . When the deuteron is scattered in the (θ, ϕ) direction with respect to the incident direction, the direction \vec{v}'_p after scattering is calculated as follows.

$$\vec{v}'_p = R(\vec{n}_\parallel, \phi)R(\vec{n}_\perp, \theta)\vec{v}_p \quad (4.28)$$

Collision energy loss

When the deuteron and a metal atom undergo elastic scattering, part of the energy moves to the atom and the energy of the deuteron decreases. The energy E'_p of the incident deuteron after scattering is derived from the energy and momentum conservation equations.

$$E'_p = \left(\frac{m_p \cos \theta \pm \sqrt{m_m^2 - m_p^2 \sin^2 \theta}}{m_p + m_m} \right)^2 E_p \quad (4.29)$$

4.4.2 Collision point

From the trajectory obtained by § 4.4.1, the point of occurrence of the $d + d$ reaction is determined. First, we calculate the trajectory for each deuteron, contained in the molecule. We choose two trajectories $\vec{T}_1(t)$, $\vec{T}_2(t)$, and call the corresponding deuterons as d_1 , d_2 . The way of combination is 3 pairs if D_3^+ and 1 pair if D_2^+ . Positions $\vec{x}_1(t)$ and $\vec{x}_2(t)$ at the time t of d_1 , d_2 are expressed by the following equations, taking the initial coordinates of d_1 as the origin.

$$\vec{x}_i(t) = \vec{x}_i(0) + \vec{T}_i(t) \quad (i = 1, 2) \quad (4.30)$$

Here,

$$\vec{x}_1(0) = (0, 0, 0) \quad (4.31)$$

$$\vec{x}_2(0) = r_{dd}(\sin \alpha \cos \beta, \sin \alpha \sin \beta, \cos \alpha) \quad (4.32)$$

α , β is the polar angle and azimuth of d_2 seen from d_1 . If the initial position distribution of d_2 is isotropic, at time t , d_2 can be regarded on the spherical shell of radius r_{dd} centered on $\vec{T}_2(t)$. $\vec{x}_1(t_{\text{col}}) = \vec{x}_2(t_{\text{col}})$ is derived for time t_{col} when d_1 collides with its deuterium membrane is expressed as,

$$|\vec{T}_1(t_{\text{col}}) - \vec{T}_2(t_{\text{col}})| = r_{dd} \quad (4.33)$$

Once the collision time is determined, the cross section of the $d + d$ reaction can be calculated from both momenta at that time. The time expressed in Equation (4.33) is not necessarily once for a set of trajectories. If d_1 passes through the deuterium membrane and returns to the inside of the membrane again, multiple collisions will occur.

Energy distribution at collision

The calculated result of the energy distribution of the center of mass system at the collision with a incident energy of 20 keV is shown in Figure 4.3. The black line represents the number of events in each E_{cm} , and the red line is the product of the number of events and the cross section of the $d + d$ reaction $\sigma(E_{\text{cm}})$. From the black

line, we find that most collisions give small values of E_{cm} . This results that most of the scattering in small-angle scattering and two deuterons are traveling almost in parallel. In such a condition, the collision can not contribute to the yield, because the cross section becomes very small. The red line shows that the yield of the CCM spans a wide range of E_{cm} , $10 \leq E_{\text{cm}} \leq 38$ keV.

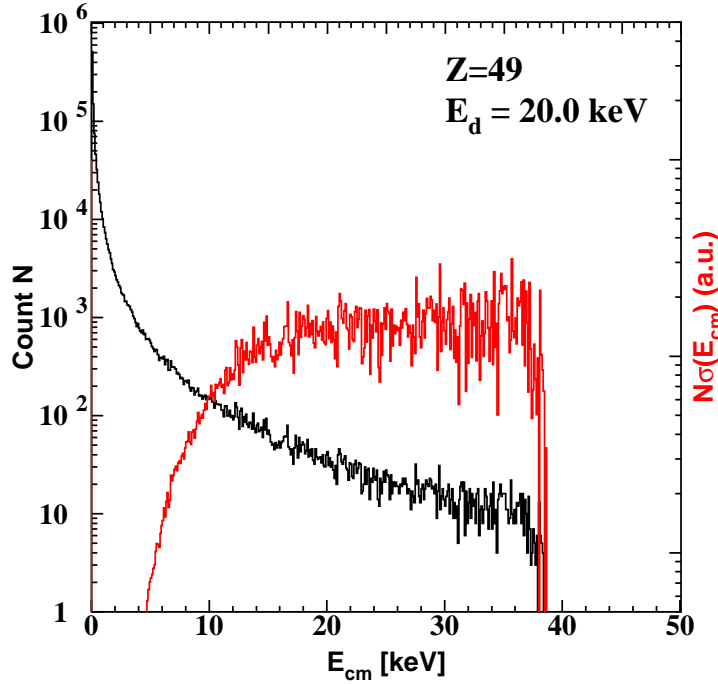


Figure 4.3: E_{cm} distribution at collision. Incident Energy is 20 keV. Target metal is Indium. The black line shows the count number of E_{cm} and the red line is weighted by the cross section of $d + d$ reaction.

Figure 4.4 shows the scatter plot of E_2 vs E_1 at collision point. The higher(lower) energy deuteron is $d_1(d_2)$, and corresponding energy and polar angle are $E_1(E_2)$ and $\theta_1(\theta_2)$, respectively. The target is In and incident energy is 20 keV. Each event is weighted by $\sigma(E_{\text{cm}})$. The red lines show the maximum energy (0 degree scattering) and the minimum energy (180 degree scattering) after elastically scattered deuteron at incident energy E_1 . Almost all events are within the red lines. This implies that most of events are composed of single large-angle scattering.

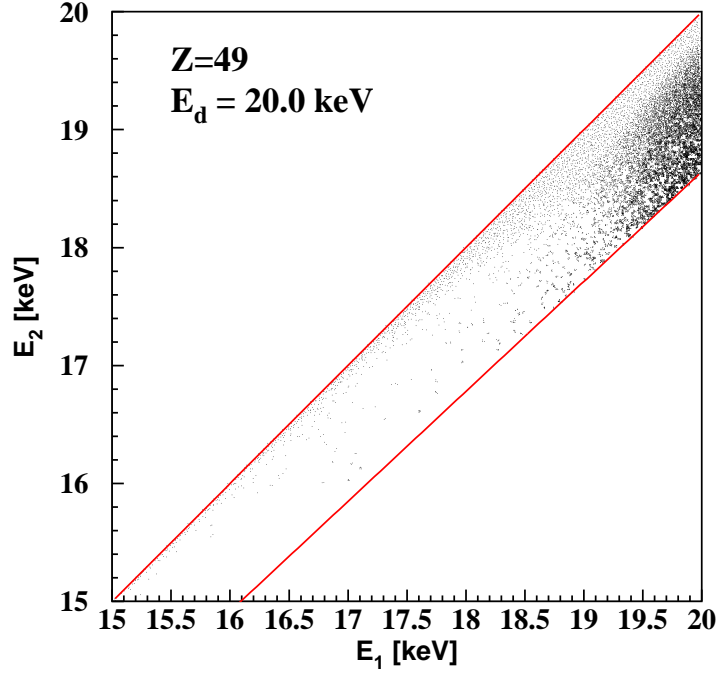


Figure 4.4: Scatter plot of E_1 and E_2 at collision point.

The E_1 and E_2 distributions at 20 keV incident are shown in Figure 4.5. Each event is weighted by $\sigma(E_{\text{cm}})$. The upper figure and the lower figure are those for the In and Pb target, respectively. And E_1 is represented by black lines and E_2 by red lines. Although E_1 looks identical in shape on both targets, E_2 is sharper for Pb target and peak position is higher. Since the energy difference between E_1 and E_2 is caused by an elastic scattering with metal atom, this is due to the difference in mass of In and Pb. Most of the yields are concentrated in $19 \text{ keV} \leq E_1 \leq 20 \text{ keV}$. Considering that 1 keV is an energy loss caused by traveling through the metal, we considered that almost all $d + d$ reactions are occurring in extremely thin layers of the surface (about 20 nm at $E_d = 20 \text{ keV}$). It can be inferred that the distance of the deuterons spreads quickly after the incident on the metal and cooperative collisions are formed with the event that caused large angle scattering before spread out.

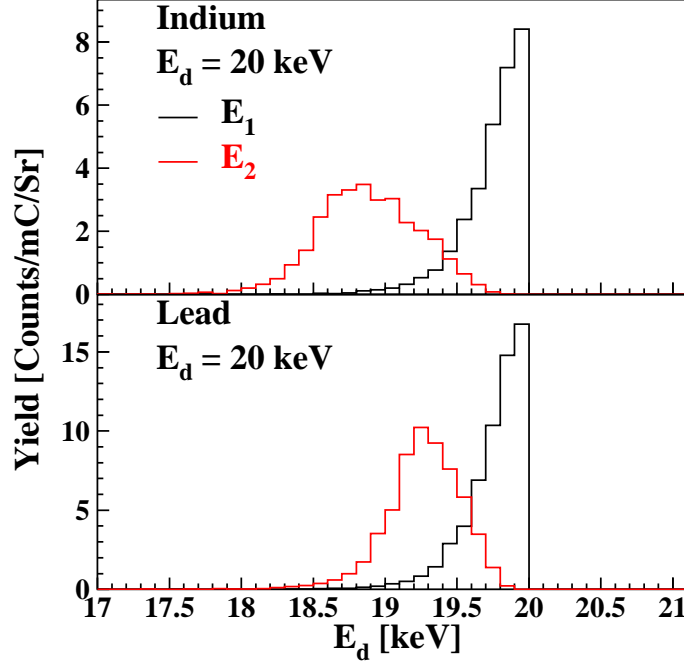


Figure 4.5: Energy distributions of E_1 and E_2 at collision.

4.4.3 Total yield

As we have determined the momentum of each deuteron at collision at § 4.4.2, the reaction yield can be calculated from the cross section of the $d + d$ reaction. Let n be the deuteron combination number and m the number of collisions in one combination, the number of collisions occurred in a combination both is discussed in § 4.4.2. The $d + d$ cross section for the k th collision in the j th deuteron combination is written as $\sigma_{j,k}$. The probability, P_{dd} , that a $d + d$ reaction occurs when a deuteron molecule strikes the metal is given by the following formula,

$$P_{dd} = \rho_d \sum_{j=1}^n \sum_{k=1}^m \sigma_{j,k}. \quad (4.34)$$

The $\sigma_{j,k}$ is calculated from the cross section described in § 2.1. This calculation process is repeated, and we obtained a probability \bar{P}_{dd} from the average. The average

number of $d + d$ reaction per $N_{\text{mC}} = 6.2415 \times 10^{15}$ counts of deuteron molecular incident for In target is shown in Figure 4.6. The difference of color represents the difference of the screening model for Coulomb scattering, the red, green and blue line shows calculated total yield with Bohr, Moliere and ZBL model, respectively. Although the energy dependence of the yield does not change largely for the screening model, the absolute value of yield changes by about 40% at maximum. Figure 4.7 shows the yield ratio for each screening model to the Bohr model. The yield is the largest in the Bohr model, followed by the Moliere and ZBL model. The difference in yield reflect the difference in cross section of large-angle scattering. The ratio of the coulomb scattering cross section for each screening model to that for Bohr model as a function of incident deuteron energy is shown in Figures 4.8 and 4.9. Figure 4.8 shows that for large-scattering angle $\theta = 100^\circ$ (solid curve), 140° (dash) and 170° (dot), and Figure 4.9 shows that for small-scattering angle $\theta = 10^\circ$ (solid curve), 40° (dash) and 70° (dot). The red, green and blue curves represent ratio, respectively, for Bohr/Bohr, Moliere/Bohr and ZBL/Bohr. Although there are some differences depending on θ , the CCM yield ratios for the high energy side roughly coincide with this scattering cross section ratio. On the other hand, although the large-angle scattering cross section ratio is smaller for the Bohr model than for the Moliere and ZBL model on the lower energy side, the yield ratio is larger for the Bohr model. This seems to reflect the quick separation of deuterons due to the large scattering cross section of small angles for the Moliere and ZBL model on the lower energy side which can be seen in Figure 4.9.

4.5 Yield and energy spectra at laboratory frame

Experimentally detected particles are limited to those emitted to the detector. The particles emitted from the CCM have the angular dependence which originates from the angular distribution of $d+d$ reaction, $W(\theta)$, and the solid angle ratio ($d\Omega_{\text{cm}}/d\Omega_{\text{lab}}$). The $W(\theta)$ and ($d\Omega_{\text{cm}}/d\Omega_{\text{lab}}$) are already discussed in § 2.4 and § 2.5.2, respectively. The detection probability at the area of $\Delta\Omega_{\text{lab}}$ at the angle θ^{lab} in the laboratory

frame is expressed by the following equation,

$$\Delta P_{dd}(\theta^{\text{lab}}) = \rho_d \sum_{j=1}^n \sum_{k=1}^m \sigma_{j,k} W(\theta^{\text{cm}}) \left(\frac{d\Omega_{\text{cm}}}{d\Omega_{\text{lab}}} \right) \Delta\Omega_{\text{lab}}. \quad (4.35)$$

Here, θ^{cm} is an angle of θ^{lab} in the center of mass frame.

4.5.1 Yield

The angular dependence of the CCM yield, $R(\theta^{\text{lab}}) = \Delta P_{dd}(\theta^{\text{lab}})/\Delta\Omega_{\text{lab}}P_{dd}$, is shown in Figure 4.10 and 4.11. The angular dependence originate from the angular distribution of $d + d$ reaction and the solid angle ratio of laboratory and center-of-mass frame are drawn individually in Figure 4.10 with a black and blue curve, respectively. The product of these components becomes $R(\theta^{\text{lab}})$ (red curve). Figure 4.11 shows the angle dependence for each incident energy. In the present experiment, the detector is installed at $\theta^{\text{lab}} = 146^\circ$ where the angular dependence is small. For the variation of 10° for θ^{lab} causes only change of 0.6 % for $R(\theta^{\text{lab}})$.

The $\Delta P_{dd}(\theta^{\text{lab}})$ for the Bohr model for $\Theta^{\text{lab}} = 146^\circ$ is drawn in Figure 4.12 with the black(In) and red(Pb) curve as a function of incident energy E_d . A thick-target yield for same incident energy with a rest deuteron target is also drawn with blue curve. Since the yield of blue line proportional to the deuteron density in metal, it is normalized to $\Delta P_{dd}(\theta^{\text{lab}})$ for In at $E_d = 15$ keV. The blue line has the same energy dependence as in the case of previous solid metal target experiments, and the CCM yield has a weak energy dependence with respect to the solid metal experiments. This is because the average energy of center-of-mass system, \bar{E}_{cm} ; $\bar{E}_{\text{cm}} \sim E_d/2$ for solid metal experiments, however, $\bar{E}_{\text{cm}} > E_d$ for the CCM.

4.5.2 Energy spectra

Figure 4.13 shows the energy spectrum of charged particles emitted from the CCM to $\theta^{\text{lab}} = 146^\circ$ for In target. The spectra of proton, triton and ^3He are the same shape, which are wide and asymmetry. The shape of the CCM spectra can be understood from the energy of CM system of two deuterons E_{cm} and the velocity of CM frame with respect to the Lab frame \vec{v}_{cm} . When the only small-angle scattering occurs between a deuteron and metal atom, E_{cm} becomes very low because the two deuterons go almost

parallel, and the cross section of $d + d$ reaction becomes very small. In such a case, \vec{v}_{cm} is almost equal to the speed of the deuteron, and it moves away from a detector installed at backward angle. Therefore, the energy of the detected particles becomes lower. When large-angle scattering occurs, E_{cm} becomes larger as the scattering angle is backward, and \vec{v}_{cm} approaches to $\vec{0}$. Such an event has a high $d + d$ reaction cross section and forms a peak on the high energy side. Since the E_{cm} dependency of the $d + d$ reaction cross section is stronger than the scattering angle dependence of the Coulomb scattering cross section, the large-angle scattering event become dominant, although the probability of large-angle scattering is very low.

Figure 4.14 shows the energy spectra for each model. The red, green and blue line show that for Bohr, Moliere and ZBL model, respectively. The target is the In, and the incident energy is fixed to 20 keV. The shapes are almost the same.

4.5.3 Feature of the CCM spectra

A 2-dimensional histogram of θ_2 vs emitted energy of proton E_p is shown in Figure 4.15. Incident energy of deuteron is fixed to 20 keV, and the target is In. Each events are weighted by the cross section of the $d + d$ reaction. Since the E_p depends on not only θ_2 but also azimuthal angle of collide deuterons, it can be wide E_p even at the same θ_2 .

We separate the E_p every 70 keV (drawn with red dot line in Figure 4.15), and present the θ_2 distribution for each region in Figure 4.16. The ranges of E_p are shown in upper left of each panel; they are 2710–2780, 2780–2850, 2850–2920, 2920–2990, 2990–3060 and 3060–3130 keV, respectively. It can be seen that around the peak energy of $E_p = 3000$ keV, events are of large-angle scattering greater than 100° . On the other hand, those for the lower energy tail of E_p are composed of small-scattering angle less than 100° . The events for small angle scattering less than 30° hardly contribute to the yield.

Figure 4.17 shows the energy spectra of emitted protons for each incident energy, E_d . The values of E_d is shown in upper left of each panel. The difference of color shows the difference of target; black for Pb and red for In. The peak position of the CCM weakly depends on E_d and target, however, the width strongly depends on E_d . The dashed blue line corresponds to the peak position for the normal $d(d,p)t$ reaction. As the incident energy decreases, the peaks of both reactions are close to each other

and their widths become similar, it becomes difficult to distinguish them at very low energies.

Figure 4.18 shows proton energy spectra for various detection angles, θ^{lab} . The values of θ^{lab} are written in the upper left of each panel. The incident energy of deuteron is fixed to 20 keV, and the target is In. It can be seen that the E_p spectra strongly depends on the θ^{lab} . Basically, the average of E_p increases as the θ^{lab} decreases. This trend is the same as the solid metal experiments. Two peaks can be seen for $\theta^{\text{lab}} = 70\text{--}110^\circ$; this originates from the azimuthal angle dependence of E_p .

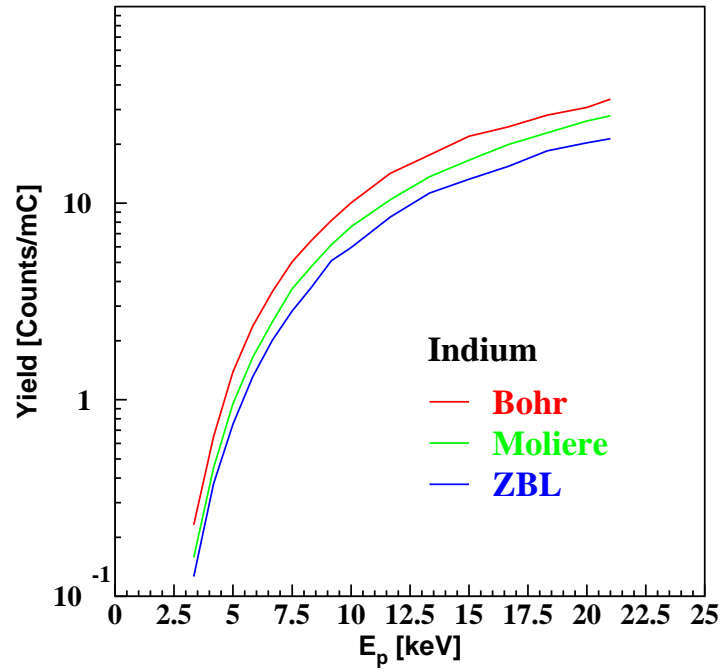


Figure 4.6: Calculated total yield of CCM for Indium target.

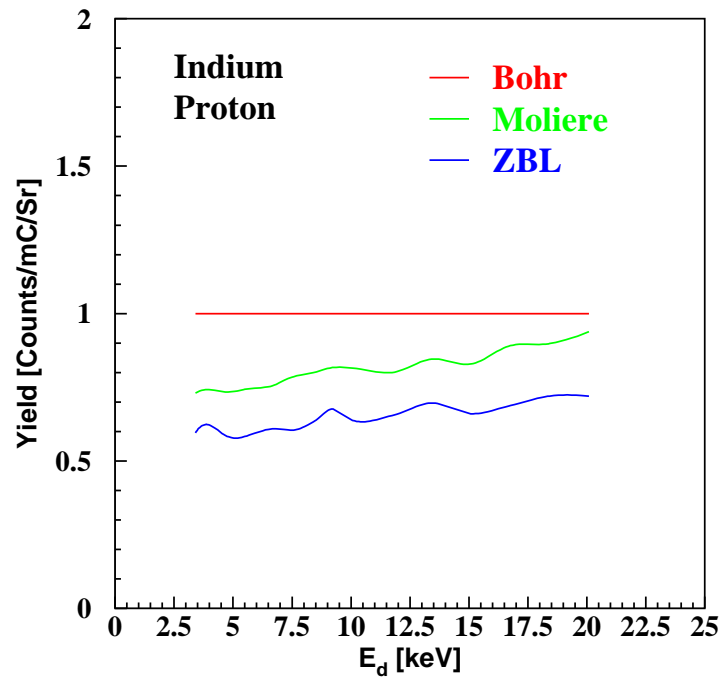


Figure 4.7: Yield ratio with respect to Bohr screening model.

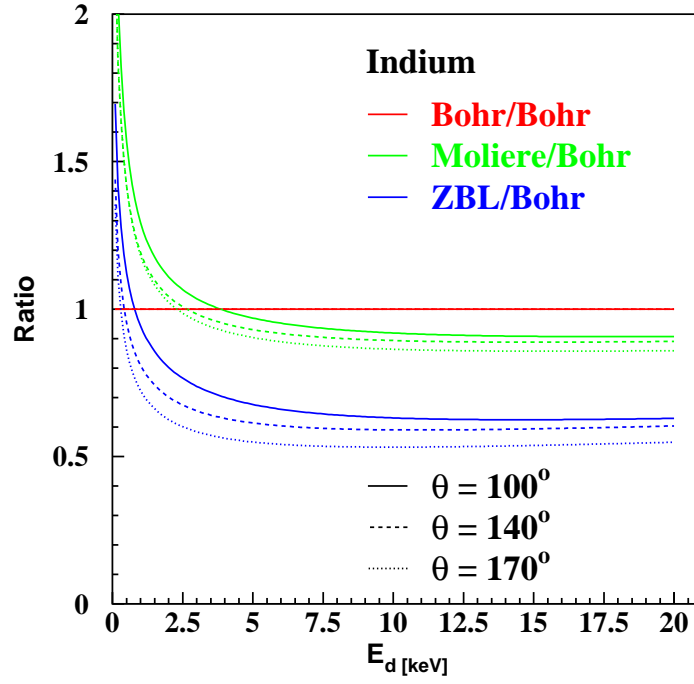


Figure 4.8: Differential cross section ratio of large angle scattering with respect to one of Bohr screening model.

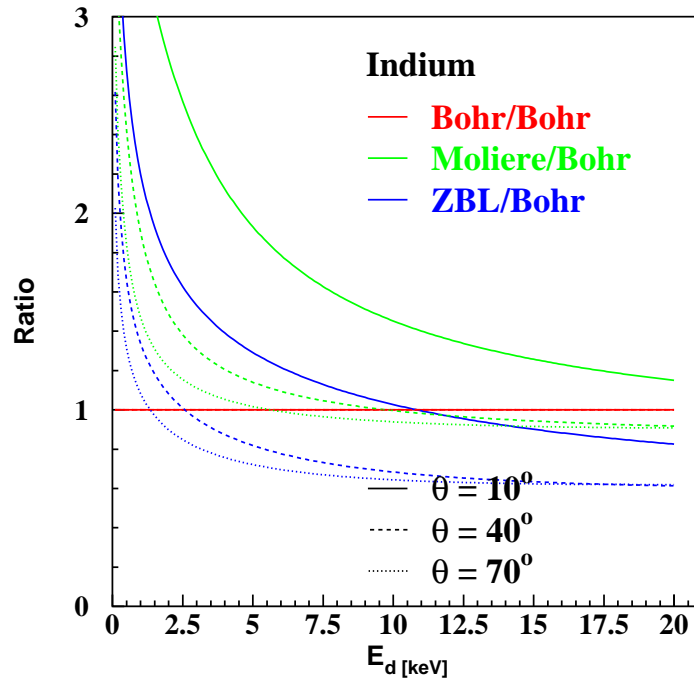


Figure 4.9: Differential cross section ratio of small angle scattering with respect to one of Bohr screening model.

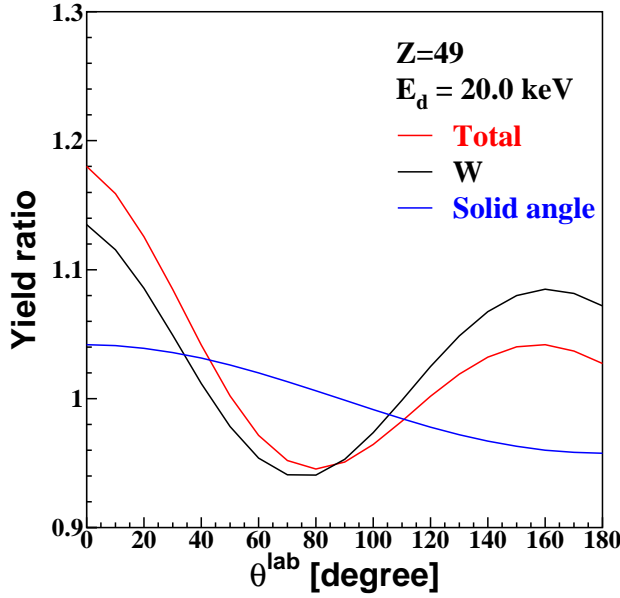


Figure 4.10: Angular dependence of the CCM yield for each component. Black and blue curve show the angular dependence originates from the angular distribution of $d + d$ reaction in CM frame and the solid angle ratio of laboratory and CM frame, respectively. Red curve shows the product of these components which becomes the effective angular dependence.

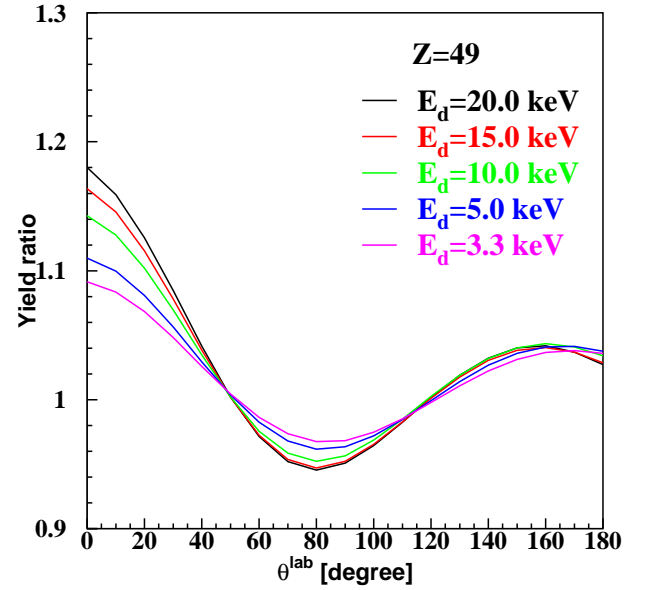


Figure 4.11: Angle dependence for each incident energy for In target.

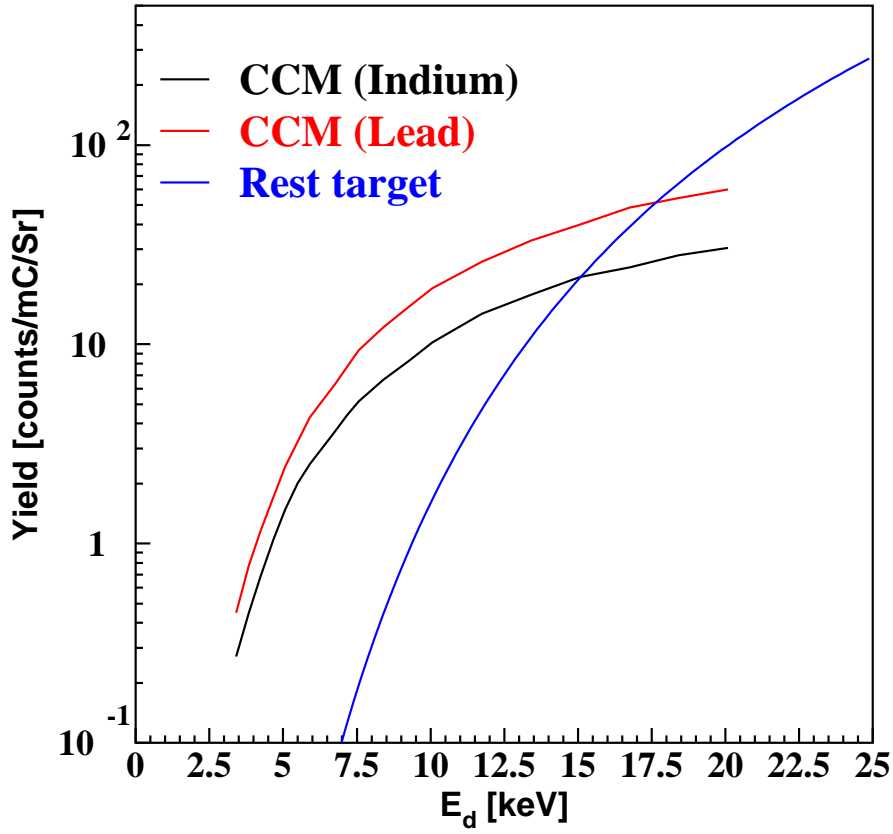


Figure 4.12: The $\Delta P_{dd}(\theta^{\text{lab}})$ for Bohr model for $\Theta^{\text{lab}} = 146^\circ$ and a thick-target yield for same incident energy with a rest deuteron target.

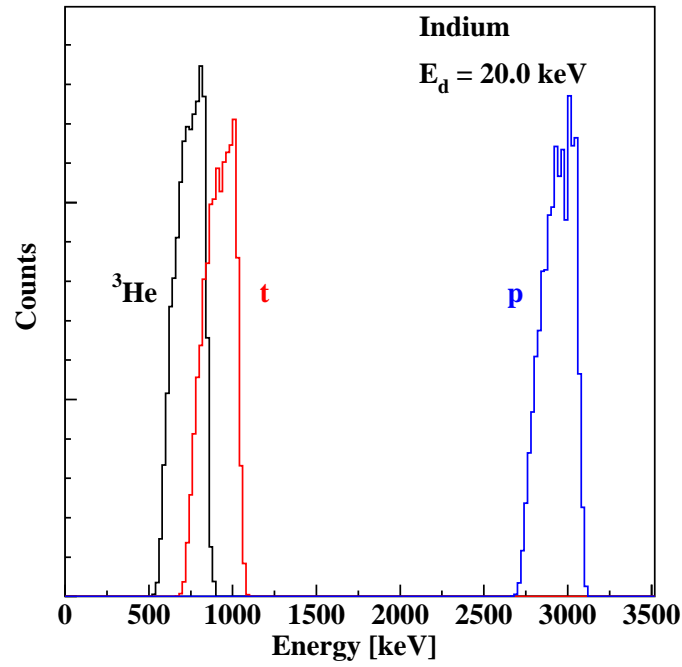


Figure 4.13: Energy spectra of emitted particles from CCM for In target

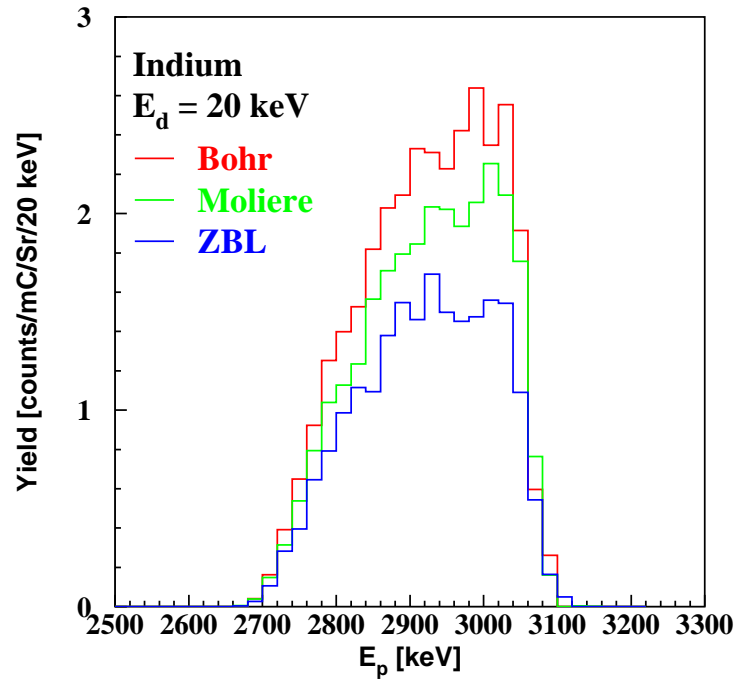


Figure 4.14: Energy spectra of emitted particles from CCM with each model. The target is the In, and the incident energy is fixed to 20 keV.

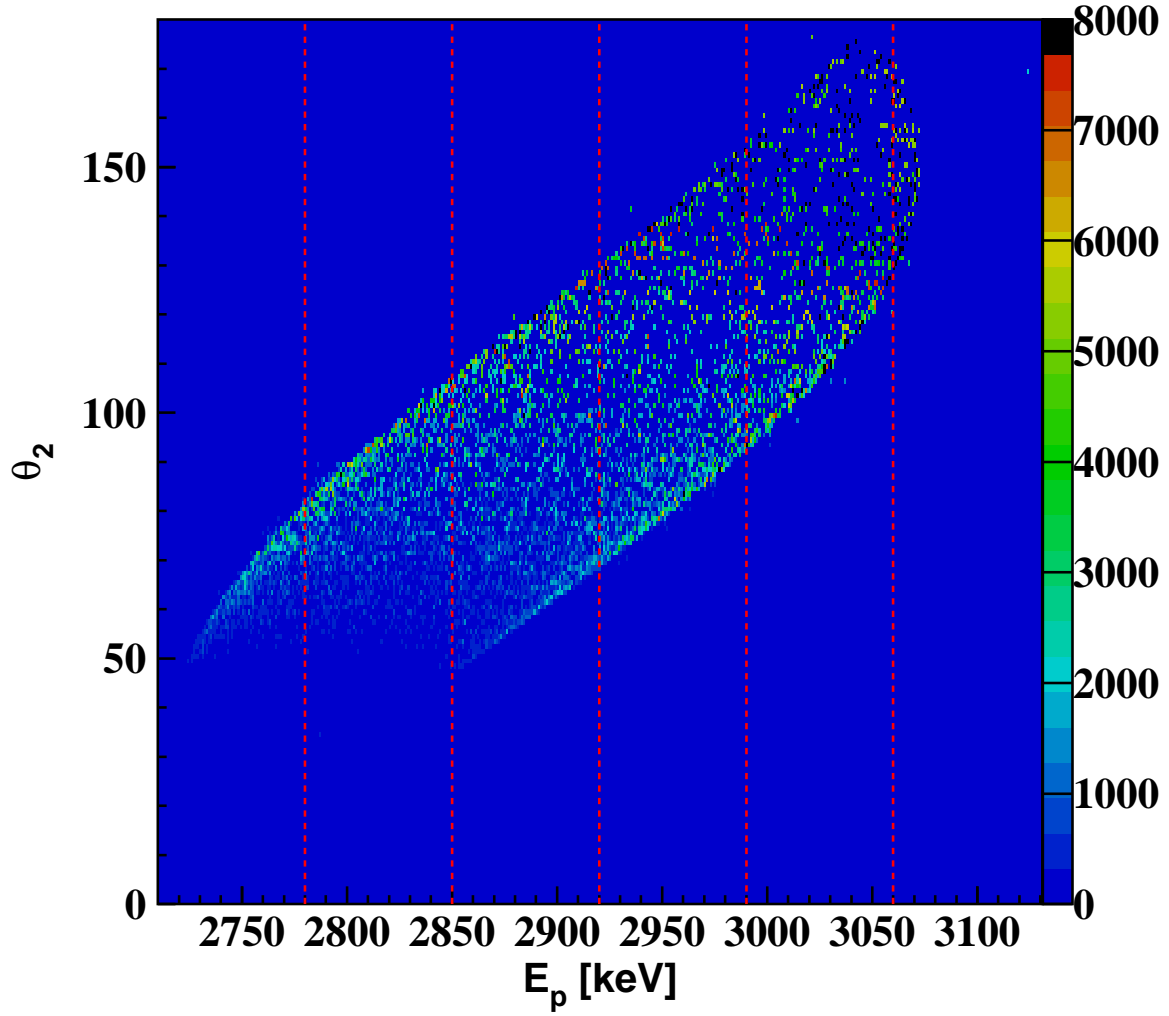


Figure 4.15: 2-dimensional histogram of θ_2 vs E_p . Incident energy of deuteron is fixed to 20 keV, and the target is In. Each events are weighted by the cross section of $d + d$ event.

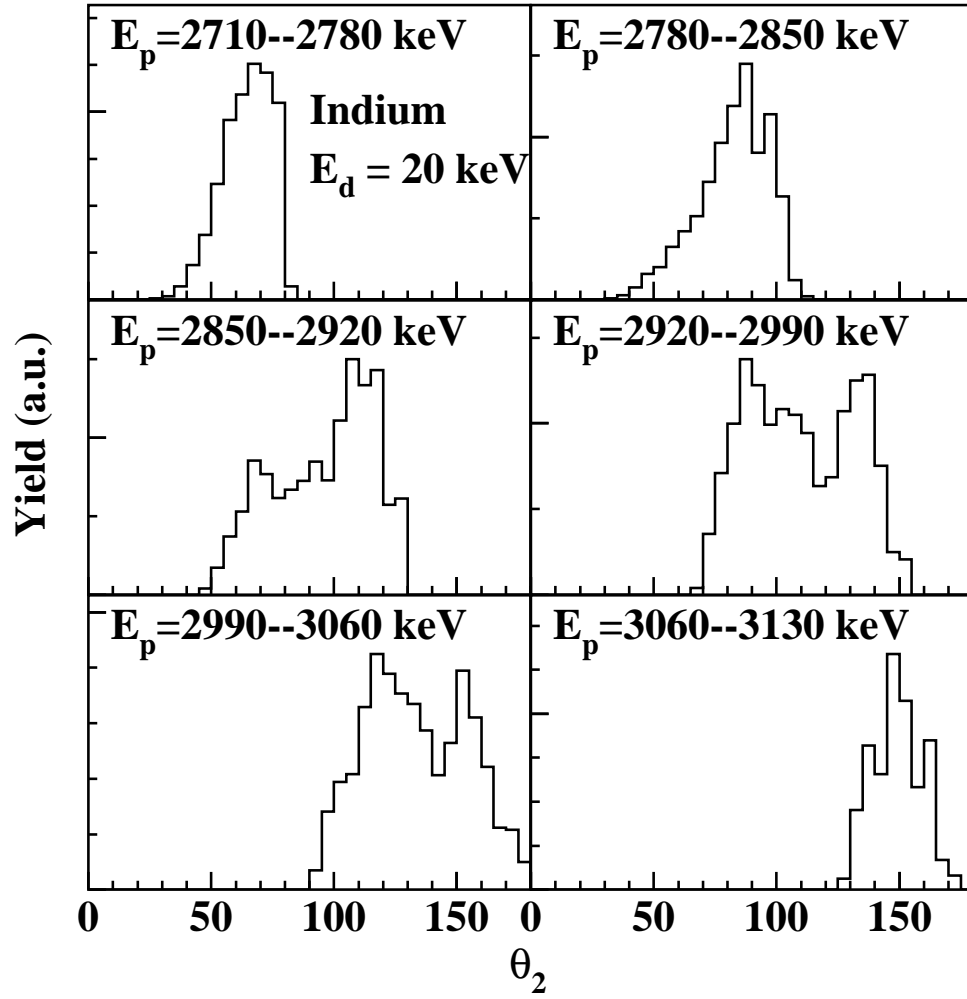


Figure 4.16: The θ_2 distribution for each region of E_p . The ranges of E_p are shown in upper left of each panel, and they are 2710–2780, 2780–2850, 2850–2920, 2920–2990, 2990–3060 and 3060–3130 keV, respectively. Incident energy of deuteron is fixed to 20 keV, and the target is In. Each events are weighted by the cross section of $d + d$ event.

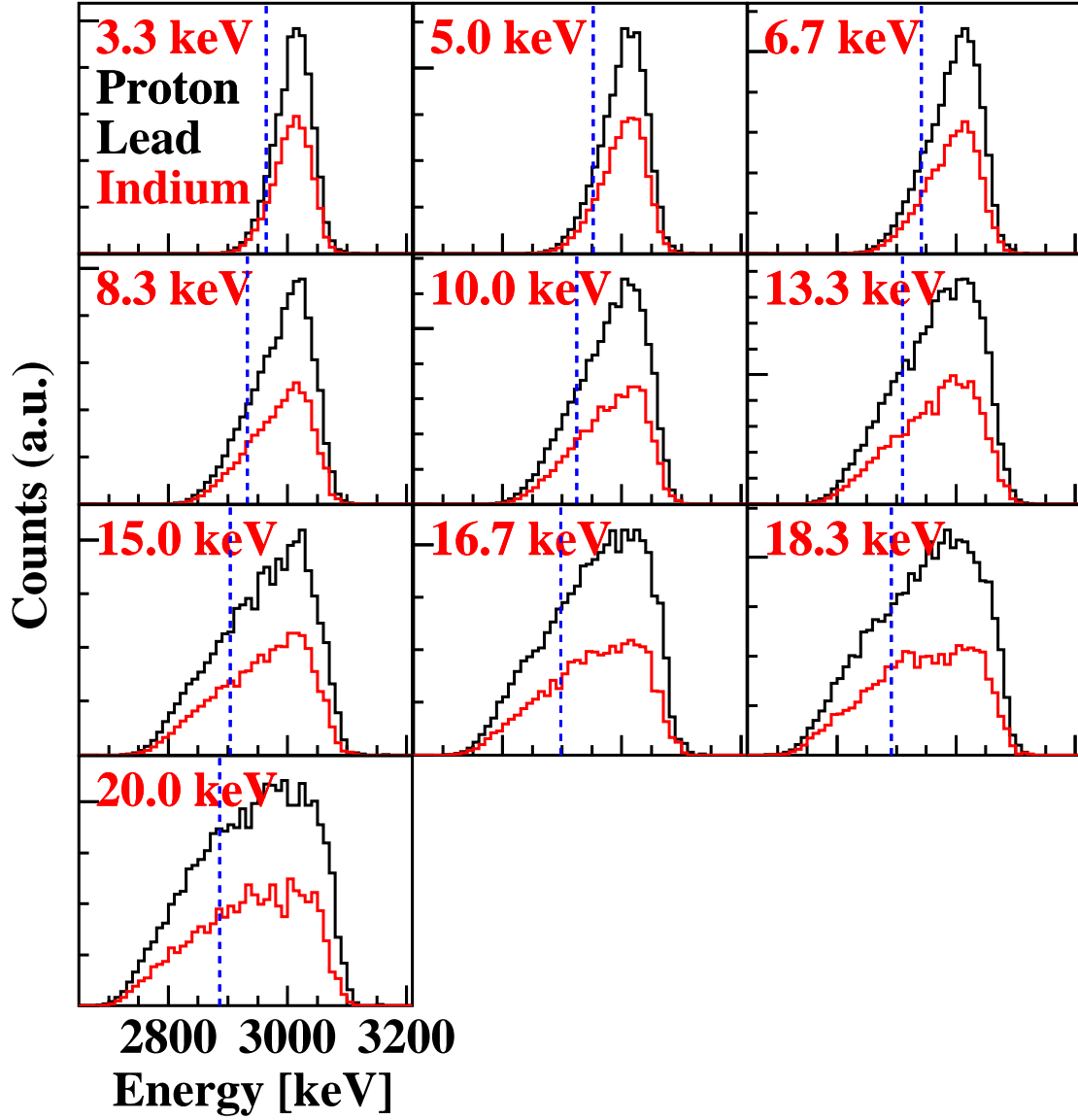


Figure 4.17: Energy spectra of proton emitted from CCM for each incident energy. The difference of color shows the difference of target, and black and red line are for Pb and In, respectively. The dashed blue lines correspond to the peak position of past solid metal experiment.

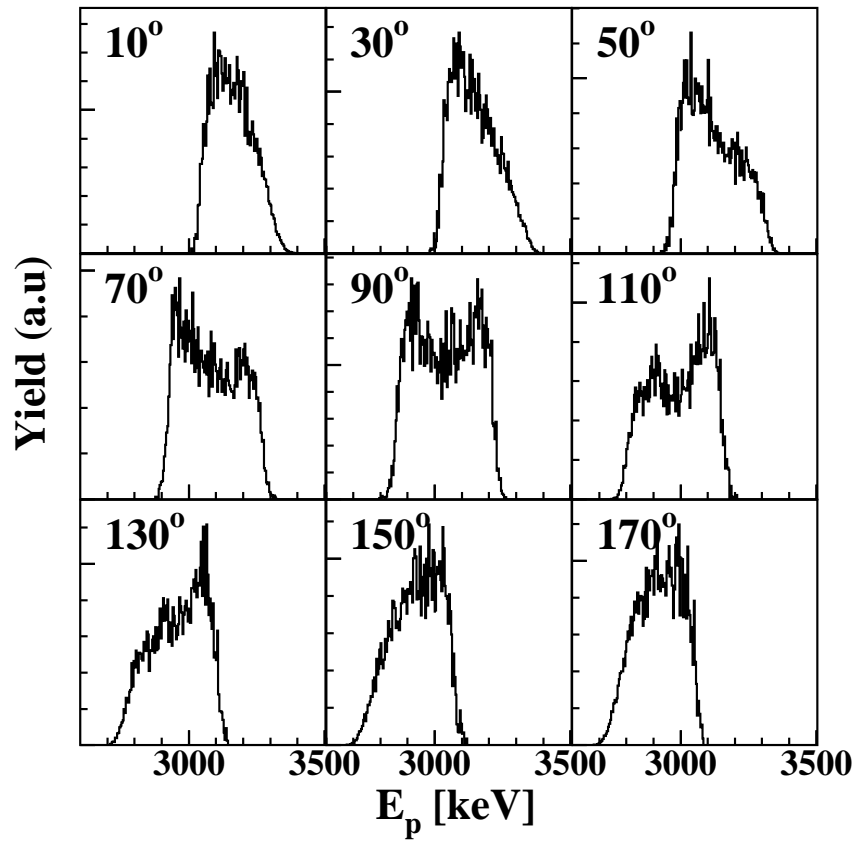


Figure 4.18: The E_p spectra for each detection angle θ^{lab} . The values of θ^{lab} is written in the upper left of each panel. Incident energy of deuteron is fixed to 20 keV, and the target is In.

Chapter 5

Experiment

For the purpose of the systematic data accumulation of CCM, we conducted beam experiments with liquid In, Pb, Sn and Bi. These experiments are classified into two series, In and Pb, and Sn and Bi. The former corresponds to the experiments measured more precisely. We irradiated a D_3^+ beam to these metals, and measured the energy of the charged particles emitted from the $d + d$ reaction through the CCM. The total beam energy $E_{D_3^+}$ is 10–60 keV, which is equivalent to 3.3–20 keV of energy per deuteron E_d . The experiment was conducted in high vacuum condition of $P \sim 3 \times 10^{-5}$ Pa. All target metals are heated and is liquefied by cartridge heaters. Due to the lack of the lattice structure very few deuterons accumulate in the target. The $d + d$ reaction with rest deuterons in the target (we call it normal $d + d$ reaction) are strongly suppressed, and the CCM becomes a dominant process. Since the normal $d + d$ reaction gives background yields for the CCM, the density of the rest deuterons is measured after each measurement. with a 60-keV D^+ beam. As already discussed in § 1.2.3, the metal surface during the beam bombardment must be clean. For liquid metal, the surface continues to change due to convection and, thus, it can be expected that the clean surface is maintained. Nevertheless, a contamination layer may be formed by a long-time beam bombardment or passage of time. Since such a layer is solid, deuterons can accumulate and the density of the rest deuteron becomes high. Therefore, the normal $d + d$ reaction can be observed during the D^+ beam bombardment. When the contamination is detected, we can remove it with a scraper

without breaking the vacuum. At that time, a small amount of metal target is removed together with the contaminants. Thus, the distance between the detectors and the beam spot slightly increases. In order to compensate the change of the detector solid angle, the height of the target is always measured using a laser displacement sensor (LDS) before the cleaning. Experimental procedure is summarized below,

- 1) Bombard the liquid metal target with a D_3^+ beam, and accumulate the $d + d$ reaction data.
- 2) Bombard the target with a 60-keV D^+ beam, measure the deuteron density, and check the surface cleanness.
- 3) Measure the target height with LDS if the contamination is detected. (Otherwise go back to 1).
- 4) Clean the target.

The processes 2) and 3) were performed only for the In and Bi target experiments. Since the Sn and Bi target experiments were conducted earlier, the target height measurement system had not been installed yet and the experimental procedure had not been established. Nevertheless, the surface cleanness of the target and the absence of the deuteron accumulation were confirmed by the absence of the peak of corresponding to the normal $d + d$ reaction in the energy spectra.

The measurement proceeds by repeating the cycle of a beam bombardment for 10 seconds and a beam current measurement for 3 seconds. The beam current I_b is measured with a Faraday cup installed upstream of the target. Inserting and pulling out the Faraday cup from the beam path realize the cycle.

The charged particles are detected by two silicon detectors, whose distance from the target is 60 mm and angle, θ^{lab} , is 146° with respect to the beam direction. The temperature of the metal target, T_m , is measured by a infrared radiation thermometer. The experimental conditions are summarized in Table 5.1. Here, the solid angles Ω^{lab} for Pb and Bi experiments are those for the latest measurement.

The beam line is explained in § 5.1, the description about production method of liquid metal target and the reaction chamber is in § 5.2, the measurement equipment such as silicon detector, Faraday cup, radiation thermometer and LDS are described in § 5.3, temperature of the target is discussed in § 5.4.2 and the data acquisition system is described in § 5.6.

Table 5.1: Summary of the experimental conditions

Target	Indium	Lead	Tin	Bismuth
T_m (°C)	264 – 320	438 – 489	340–380	320–358
$\Omega^{\text{lab}}/4\pi$ (%)	2.76 ± 0.07	2.76 ± 0.07	2.61 ± 0.07	2.61 ± 0.07
purity	Natural (6N)			
θ^{lab} (degree)	146			
$E_{D_3^+}$ (keV)	10 – 60			
I_b (μA)	5 – 60			

5.1 Beam line

A series of the experiments were conducted using the High Current Ion Accelerator (HCIA) at the Research Center for Electron Photon Science (ELPH), Tohoku University, Japan. HCIA provides the hydrogen molecular ion beams such as H^+ , H_2^+ , H_3^+ , D^+ , D_2^+ and D_3^+ . The beam energy is from 10 to 120 keV, which can be controlled adjusting a potential difference between the uppermost stream of the HCIA and the target. The typical beam current is approximately 100 μA for the 60-keV D_3^+ beam. Figure 5.1 shows an overview of HCIA. HCIA consists of an ion source, five focusing electrodes, an acceleration/deceleration electrode and two bending magnets. A duoplasmatron is employed for the ion source. The duoplasmatron ion source produces a various molecular beams; it produces not only D^+ but also D_2^+ , and D_3^+ beams simultaneously from the D_2 gas. Since the extracted ion beams from the duoplasmatron ion source have an approximately similar kinetic energy, we separate desirable molecular beams using a momentum analysis with a bending magnet. The energy of the ion beam is adjusted using an acceleration/deceleration electrode. Since the experiments was conducted using liquid metals, the ion beam is transported downward to the target in a reaction chamber using an additional bending magnet. The momentum analysis of the ion beam with a bending magnet was made twice during the transportation, and neutralized molecules in the beam are rejected. Four einzel lenses are placed to focus the ion beam, and a parallel plate electrode (steerer) behind the first bending magnet changes a vertical direction of the ion beam.

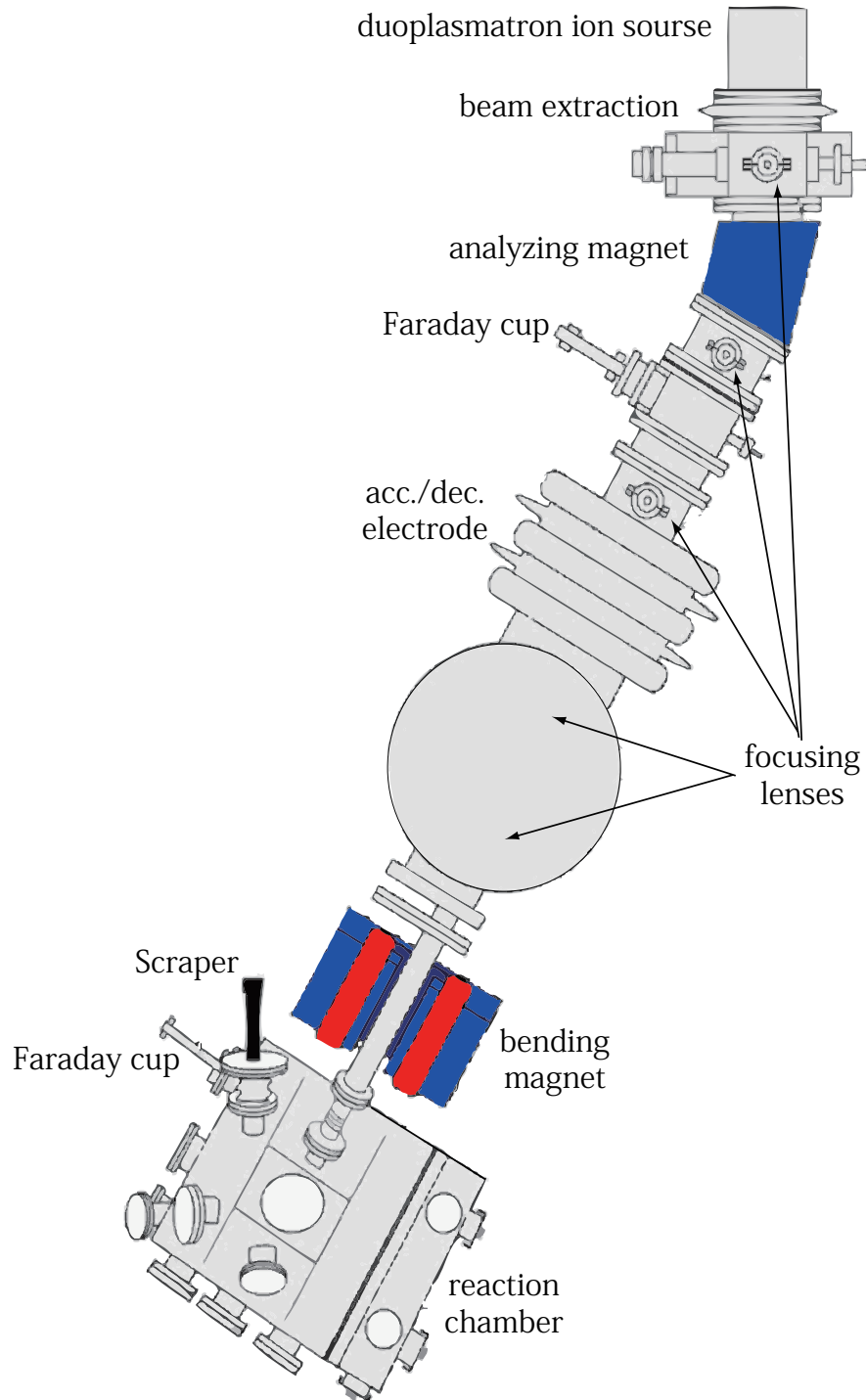


Figure 5.1: Overview of the High Current Ion Accelerator (HCIA) at ELPH. HCIA consists of an ion source, five focusing electrodes, an acceleration/deceleration electrode and two bending magnets.

5.1.1 Beam energy

The beam line is designed so that energy of the ion beam corresponds to a potential difference between a filament of the ion source and a target. In order to monitor the beam energy, we have measured the potential difference between the filament and the ground which has a same potential to the target. The difference was obtained by measuring the current through a resistance with 1 G Ω . The total beam energy E_{total} is evaluated as the following equation by taking into account the individual differences of measuring instruments,

$$E_{\text{total}} = 1.0016V + 0.1734 \text{ keV}, \quad (5.1)$$

where V keV is the potential difference.

5.1.2 Beam position

The beam position on the target is mainly determined by the deflection angle of the beam which is bent by the magnet placed just before the target chamber. Since the beam path changes somewhat with energy, the position of the beam on the target may change with energy. The beam position on the target relates to the solid angle of a detector which depends on the distance between the detector to the beam position. In the present experimental setup, which is describe in Section 5.3 in detail, when the beam position moves close 1 mm to a detector, 0.8 % of the solid angles increase. So as to decrease the uncertainty originating from the change of the beam position, we searched the optimum position of the beam aperture, placed in the chamber at 20 cm before the target.

First, we measured the beam position with the aperture at fixed position. A graph paper is placed on the target holder and bombarded with the deuteron beam. The results for the beam energy of 60, 45, 30, 25, 20, 15 and 10 keV are shown in Figure 5.2. The beam spot appears as a burnt spot on the paper. The horizontal and vertical red lines show x and y axis, respectively, and a point of intersection shows a center of the target. The beam spot is surrounded with an ellipse, and the center of the ellipse is considered as the center of the beam spot. The displacement of the beam center from the target center are summarized in Figure 5.3 as a function of the energy per a deuteron E_d . The red and black points show the x and y displacement

of the beam center from the target center, respectively. The errors of the each point are determined from the uncertainty of the position of the paper; its accuracy is estimated to approximately 0.2 mm. The x displacement seems to be independent on the energy, on the other hand, the y displacement has a clearly dependence. The dependence related to the beam momentum $\propto \sqrt{E_d}$. The black line in the Figure 5.3 shows following formula which is the result of the fitting,

$$y = 5.8741 - 1.4478\sqrt{E_d} \text{ mm.} \quad (5.2)$$

Under the present experimental setup, that energy dependence of the beam position causes maximum 4 % of variation to the solid angle of the detector. Since it is larger than the statistical error which is approximately 2 % at the maximum beam energy, we cannot ignore the variation. In order to decrease that, we adjusted the position of the beam aperture for each beam energy. When we move the aperture to +y direction, the bending angle of the second magnet should be increase to get a maximum beam current. It moves beam spot to +y direction. In the same way, we can move the beam spot to -y direction by moving the collimator to -y direction. Although, we cannot move the collimator to \pm x-direction freely, a displacement for the x-direction does not affect the solid angle because the detectors are placed symmetrically with respect to the y-axis.

The displacements after the adjustments are summarized in Figure 5.4 as a function of E_d . The red and black points show the x and y displacement of the beam center from the target center. The blue triangle shows the thickness of the spacer which determine the y-position of the beam aperture. The variation of the y displacements fall in less than about ± 0.5 mm. It effects on solid angle about 0.4 %, which is sufficiently small.

5.2 Reaction chamber

A series of the experiments with the liquid metal were conducted in a reaction chamber. Since the target is a liquid, the direction of the the beam is inclined by 30° with respect to the vertical axis. Figure 5.5 shows the side view of the reaction chamber. In order to adjust the beam size and position, the beam aperture with a diameter of 4 mm is placed just after the entrance port of the beam. Owing to a energy dependence

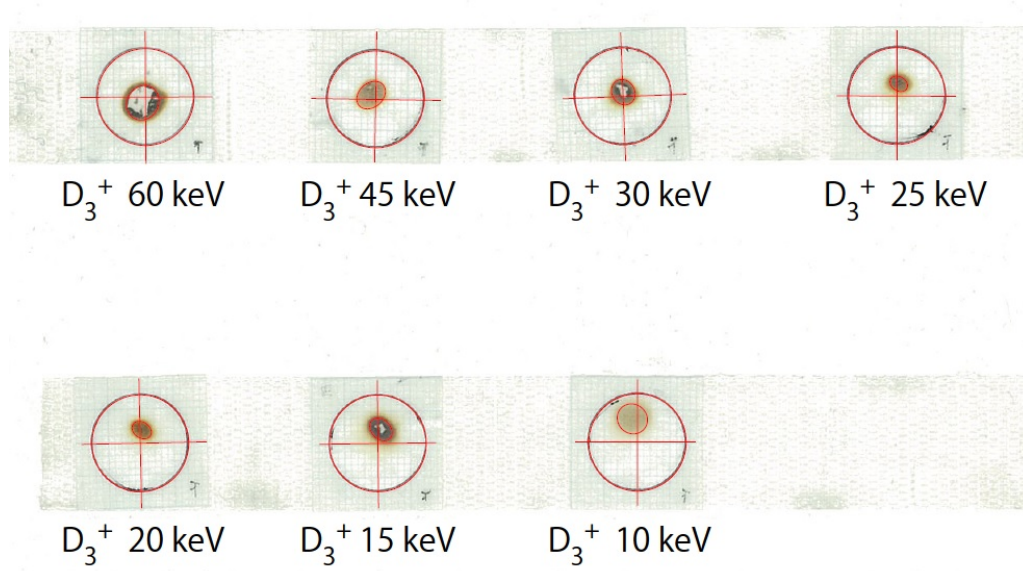


Figure 5.2: Result of the beam spot measurement with a fixed beam collimator. The red lines shows a x- and y-axis and a point of intersection of them shows a center of the target.

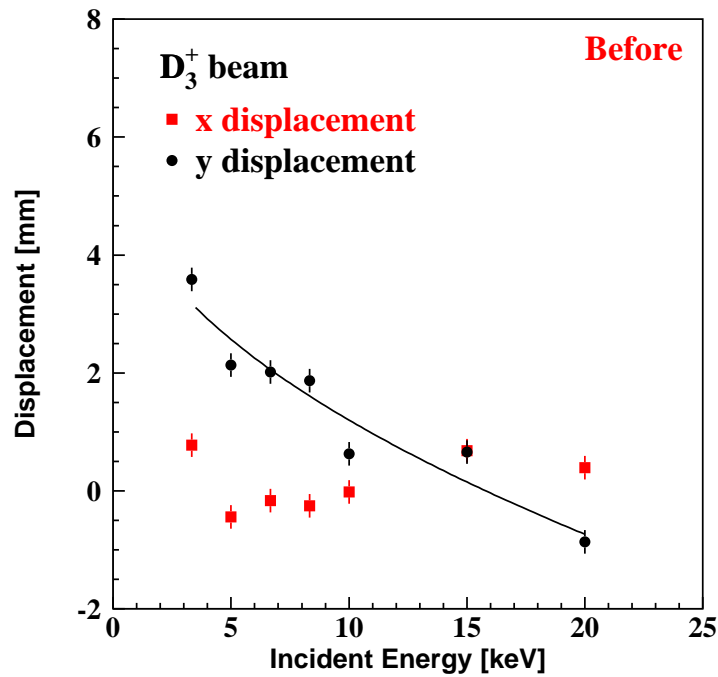


Figure 5.3: Summary of the beam spot measurement with a fixed beam collimator. The red and black points show the x and y displacement of the beam center from the target center.

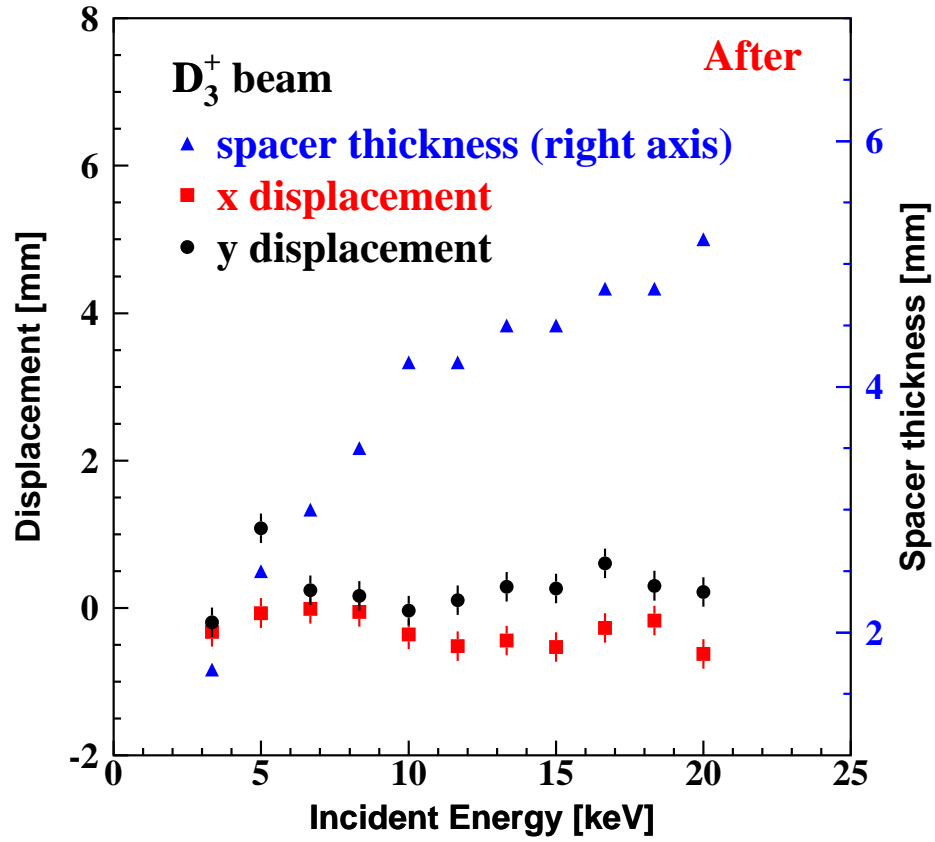


Figure 5.4: Summary of the beam spot measurement with a optimum beam collimator position. The red and black solid points show the x and y position of the beam with respect to the center of the target. The blue triangular solids shows the thickness of the spacer which determine the y-position of the beam collimator.

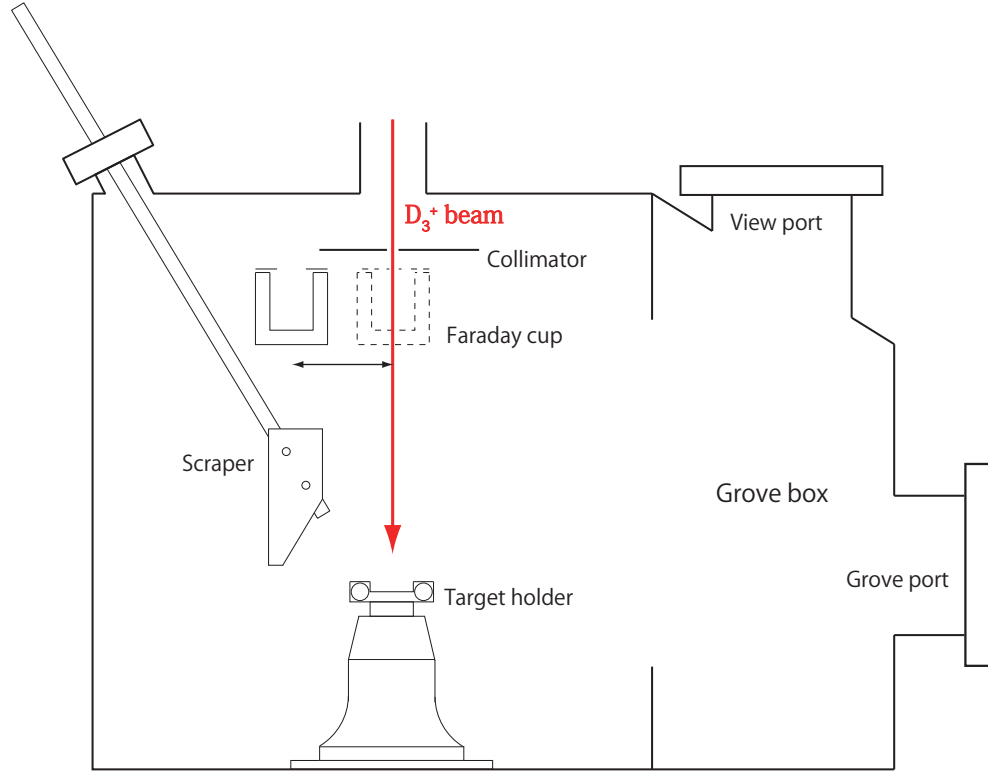


Figure 5.5: Side view of the reaction chamber.

of the beam trajectory, we adjusted a position of the aperture for each beam energy, as discussed in Section 5.1.2 in detail. A Faraday cup, which is described in Section 5.3.2 in detail, is equipped behind the aperture to measure the beam current. To handle a metal target without the exposure to an atmosphere, the reaction chamber is united with a vacuum globe box. It can reduce the oxidized contamination caused by the residual oxygen or water in a atmosphere. The contamination is removed by the scraper, which is described in Section 5.2.2 in detail, without breaking the vacuum.

5.2.1 Target holder

A target holder is fixed on the path of the ion beam. In order to liquefy a metal target, a cartridge heater is equipped to the target holder. Figure 5.6 shows the top view of the target holders. We have used two types of target holders both of which are made from SUS-316L. The target holder has a cylindrical dent for holding the targets and two holes to fix heaters. The diameter and depth of the dent are 15 mm and 3.5

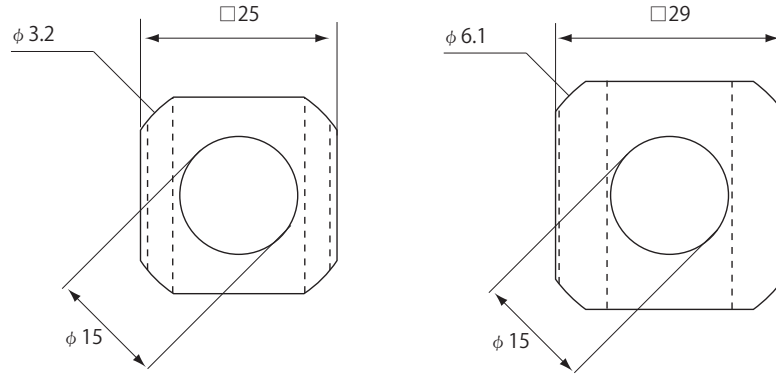


Figure 5.6: Top view of the target holders.

mm, respectively. A pair of the cartridge heaters, Hakko Electric HLX1101 with a diameter of 6.0 mm or HLJ1051 with a diameter of 3.1 mm, is stuck to the holder with heat resistance inorganic adhesive, Toagosei Aron Ceramic C. The maximum power of the heaters is 50 W. When the heater generate a heat, a temperature of the thinner heater becomes higher even if a temperature of a target is same. It has a danger to break themselves. For that reason, larger target holder is used for a measurement which needs higher temperature.

5.2.2 Scraper

Since the energies of the deuteron beam we used are extremely low, the energy loss at the contamination affect the experimental result even if these are few contaminated part. Thus, the contamination should be removed before bombarding the target. A metal surface is contaminated by residual air or water even if under a high vacuum condition ($\sim 10^{-5}$ Pa). The beam bombardment ionizes the residual and expands the contaminated part. A speed of expanding is strongly depends on the metal. The surface cleaning is necessary at least every several hours for the easy polluting metal.

In order to clean the surface of the liquid metal without breaking the vacuum, a scraper which sweeps the target surface by operating from out side of the chamber is prepared. The scraper is constructed from wobble stick, AVC AMW275-150, and a SUS plate which is fixed to the top of the wobble stick. The wobble stick provides rotational, liner and angular movement which range is 150 mm for liner and $\pm 22^\circ$ for angular. When the SUS plate touches the liquid metal where temperature is adjusted

to slightly higher than the melting point, a small amount of metal is solidified and sticks to the SUS plate together with the contamination. We made a clean metal target by repeating this operation.

5.3 Experimental setup

In the experiment, the $d + d \rightarrow p + t$ reaction and the $d + d \rightarrow {}^3\text{He} + n$ reaction occur and proton, triton and helium-3 particles are emitted. To detect these charged particles, two silicon semi-conductive detectors are employed. A carbon or aluminum absorber is placed at the front of the detectors to protect the detectors from the elastically scattered beams and spattered atoms. The details of the detector and the absorber are described in Section 5.3.1. In order to measure the temperature of the target, an infrared thermometer, which is discussed in Section 5.3.3, is used. When we clean up the surface of the target, the height of the target decrease slightly. A scanning system which consists of a laser displacement sensor and an automatic x-y stage was assembled to measure the change of the target height. Details of the scanning system are described in Section 5.3.4.

5.3.1 Detector

In the present experiment, two ion-implanted silicon detectors, ORTEC TU-023-600-300, were used. The typical energy resolution of the detector is 23-keV for 5-MeV alpha particle. The sensitive area and depletion depth of each detector are 600 mm² and 300 μm , respectively. To prevent the incidence of the charged particles from the outside of target, each detector is put in an aluminum case which is electrically isolated from the detector. The case has a hole with a diameter of 16.3 mm in front of the detector; the hole is covered by a thin carbon or aluminum foil, serving as an absorber. The absorber prevents δ -electrons, the elastically scattered beam and spattered atoms from hitting the detector. the thickness of them are 100 $\mu\text{g}/\text{cm}^2$ for carbon and 2 μm for aluminum. It stops the deuteron whose energy is lower than approximately 50 keV. The energy losses for 3.0 MeV proton, 1.0 MeV triton and 0.8 MeV ${}^3\text{He}$ -particle in the absorbers are 11.9 keV, 40.0 keV and 202 keV for carbon and 45.0 keV, 160 keV and 700 keV for aluminum, respectively. Due to the large energy loss, ${}^3\text{He}$ -particle can not be detected when the aluminum absorber is used. The cases

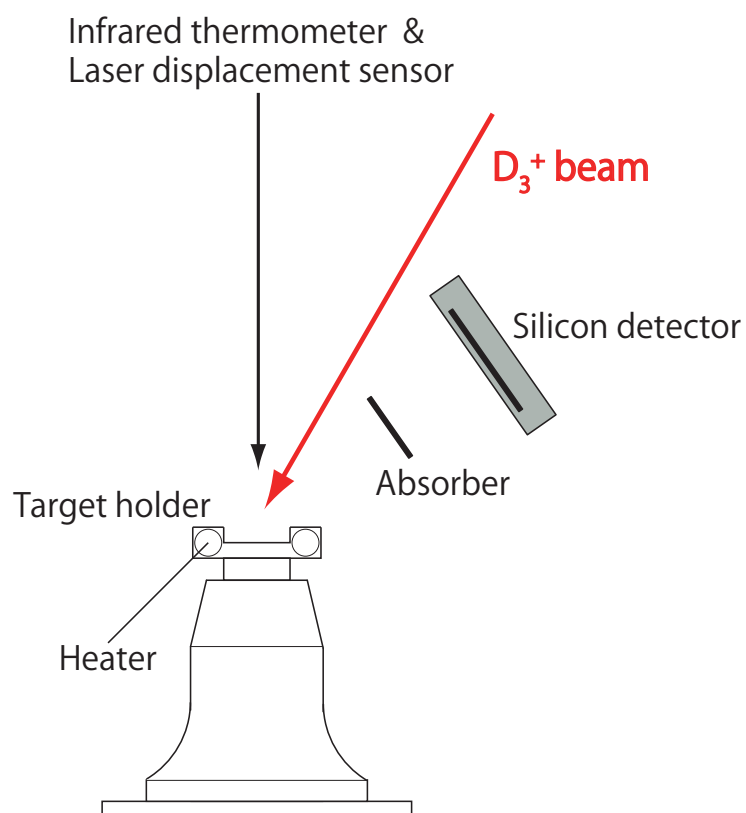


Figure 5.7: Side view of the setup in the reaction chamber.

are fixed to a rotary-linear movable feedthrough which can move 2π for rotation and 70 mm for linear. In order to reduce the thermal noise of the silicon detector, the detector is cooled down to $-10\text{ }^{\circ}\text{C}$ by circulating liquid of propylene glycol.

Figure 5.8 shows the defined coordinate of the system and placement of the detectors. A target plane is defined as the upper surface of the target holder which corresponds to the x-y plane. The y-axis is defined as a projection of the beam trajectory on that plane. The x-axis also lie on the target plane and cross to the y axis at the center of the target holder which is the origin of this coordinate. Each detector is placed at $(r, \theta, \phi) = (60\text{ mm}, 46^{\circ}, 50^{\circ})$ and $(60\text{ mm}, 46^{\circ}, 130^{\circ})$ in a polar coordinate. The angle of each detector with respect to the beam is 146° . A distance between the detector and the absorber is 25 mm.

The geometry is decided by requirements described below. The first is to reduce the background particles emitted in the $d + d$ reaction which occurs at the absorber. This reaction is caused by the accumulated deuterons in the absorber and the deuterons scattered by the target. Since a solid angle between the detector and the absorber depends on a distance between these, yields of the background are inversely proportional to the square of the distance roughly. Hence, the longer distance can reduce the background. In addition, setting the detector more backward angle can improve a separation of the foreground and the background. This due to the fact that the energy distribution of the background events are independent on the angle of the detector, but that of the foreground moves to lower energy side as the angle increases. The second is to reduce an accumulation of sputtered metal on the absorber. In the preliminary experiments, the absorber is placed at just above the liquid metal. Then, the absorber became partially thicker so that some of the emitted particles stop due to the sputtered atom. Since the angular distributions of the sputtered atoms become maximum at perpendicular to the target regardless of the incident beam angle [33], it is effective to install the absorbers at the outside of the space above the target. For these reason, we adopted this setup.

A designed solid angle for a detector is 1.28% which is calculated by the distance and the size of the detectors. Actually, the beam spot is a circle with a diameter of approximately 5 mm, this expanding affects to the solid angle. Since it is difficult to calculate the solid angle taking into account the expanding, we performed a Monte Carlo calculation to estimate the solid angle. The result of the calculation is 1.229

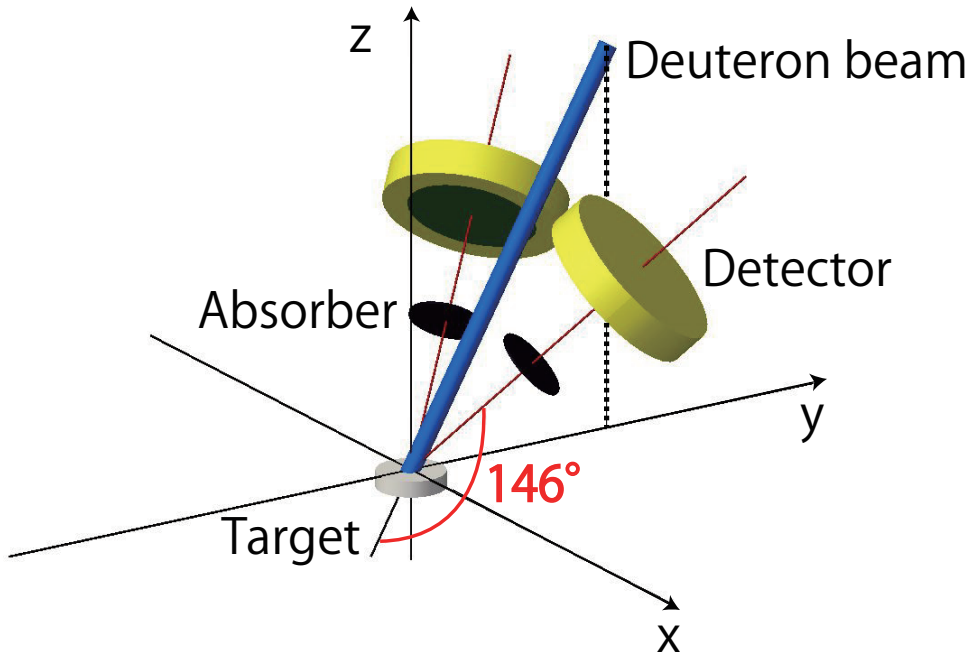


Figure 5.8: The overview of the geometry of the detectors, absorbers, target and beam path. Two detectors are installed symmetrically to the y-axis which is defined as a projection of the beam trajectory. The angle of each detector with respect to the beam is 146° . The distances from the detector to the target and the absorber is 60 mm and 25 mm, respectively.

%. Because there are particles which stop at the collimator in front of the detector, it is slightly smaller than the design value. The actual setup is probably different from the designed one. A method to measure the actual solid angle is discussed in Section 5.5.

5.3.2 Faraday cup

In order to measure the beam current in vacuum, a Faraday cup is employed. A Faraday cup is made from metal and insulated from all around. When we measure the beam current, a Faraday cup receives all of the beam and accumulates the charge. The charge is proportional to the number of the incident ions. The beam current is determined by the charge and the time of current measurement.

Our Faraday cup is placed just behind the beam aperture which is a upstream of the target. The charge of the beam incident on the Faraday cup is counted by the current integrator, Ortec 439 Digital current integrator. That module outputs a logic signal every 10 nC input. The signal is counted by a scaler, LeCroy 2551. A 100 MHz clock signal is also inputted to the scaler to determine the measurement time. While the beam bombards the target, the Faraday cup is removed from the beam line. The operation to put the Faraday cup in and out is done with an air cylinder, TAIYO 10Z-3V2LC20N30-A1AH1, which is equipped at the outside of the reaction chamber. The air cylinder is controlled by the amplified transistor-transistor-logic (TTL) signal generated by a NIM module, LeCroy 222 Gate Generator. We incorporated the operation of the Faraday cup into the DAQ system.

5.3.3 Thermometer

In order to measure the temperature of the target, an infrared radiation thermometer, Impac IP140, was employed. The thermometer measures the thermal radiation emitted from the target to determine the temperature from its intensity. It is equipped approximately 50 cm above the target, outside of the reaction chamber. The focal spot size at the surface of the target is 5 mm. The spectral range is 2 to 2.8 μm . The measured temperatures have an accuracy of 2°C below 400°C and 0.3% +1°C above 400°C. The measurement results at the experiments are described in § 5.4.2.

5.3.4 Target scanning system

A scanning system for the measurement of the target height consists of a laser displacement sensor (LDS), Optex FA CD5-W500, and an automatic x-y stage, Suruga Seiki PMG530, which was controlled by DS102. LDS can measure a distance to the target using reflection of the laser light. LDS has a emitter of the laser light and a receiver of for the reflected light. Emitted light is reflected by a target, and a part of it will be detected on the receiver, where a CCD image sensor give the position. The position has a one-to-one correspondence with a incident angle of the light. Since the incident angle also has a one-to-one correspondence with a distance between LDS and the target, the distance is determined by the position on the CCD sensor. LDS used can measure a distance from 300 to 700 mm with a linearity of $\pm 320 \mu\text{m}$.

LDS are fixed to the automatic x-y stage. The stage and LDS are equipped approximately 50 cm above the target, outside of the reaction chamber. The stage can move in an area of $30 \times 30 \text{ mm}^2$ with an accuracy of $2 \mu\text{m}$. The area covers the size of the target whose diameter is 15 mm. We divided a area of $220 \times 300 \text{ mm}^2$ into the mesh of the 0.5 or 0.25mm unit, and performed distance measurement for each mesh once. The command to LDS such as starting a measurement and reading out data is sent through an RS-422 standard of the serial communication. The command to the x-y stage such as moving to the given point is sent through an RS-232C standard of the serial communication.

Figure 5.9 shows typical results of scanning for several targets. The targets are different for each row, from top to bottom, targets are empty (only target holder), solid In and liquid In, respectively. The left column show the 2-D plot of the measurement result. The spectram of the right figures show the distance distributions within the blue circle and the red lines in the left figure. The mean value of the peak is considered as the distance between the LDS to target or target holder. A height of a target is determined by the difference between the peak of the target and that of the target holder.

In the lowest figure of the 2D-plot and the distance distribution, the measurement seems to have failed because of the low diffuse reflectivity. The failures are more pronounced for liquid metals. Therefore, metal was solidified at the LDS measurement.

If the laser does not irradiate to the target perpendicularly, the measured height can be longer. The depth of the target holder is 3.500 ± 0.005 for designed value

and 3.54 ± 0.04 mm for the LDS measurement. Therefore, the uncertainty of the height originate from the perpendicularity is considered to be approximately 1 %. The compensation using the result of the LDS measurement is discussed in § 5.5.

5.4 Metal target

The metal targets used this work are In, Pb, Sn and Bi. These metals have a relatively low melting point and low vapor pressure, which are suitable for present experiment. The natural metals are used, its purity is 99.9999 % (6 N). The atomic number Z , atomic mass, melting point, valence and vapor pressure at melting point for these are summarized in Table 5.2.

Table 5.2: Summary of the property of target metals

Metal	Z	Mass [u]	T_{melt} [K]	Valence	P_{melt} [Pa]
In	49	114.82	429	3	6×10^{-19}
Pb	82	207.2	601	4	6×10^{-7}
Sn	50	118.72	508	4	1×10^{-20}
Bi	83	208.98	545	5	1×10^{-8}

The P_{melt} is calculated by following formula [34, 35].

$$\text{In} : \log(p) = 9.919 - 12569 \cdot T^{-1} - 1.5298 \log(T) + 0.3377 \cdot T \cdot 10^{-3} \quad (5.3)$$

$$\text{Pb} : \log(p) = 8.532 - 10093 \cdot T^{-1} - 1.0750 \log(T) \quad (5.4)$$

$$\text{Sn} : \log(p) = 2.719 - 15107 \cdot T^{-1} + 0.8036 \log(T) - 0.1033 \cdot T \cdot 10^{-3} \quad (5.5)$$

$$\text{Bi} : \log(p) = 9.649 - 10400 \cdot T^{-1} - 1.26 \log(T) \quad (5.6)$$

The density of the metal is necessary to calculations for the energy loss and the scattering probability of the projectile. The following equations are used to obtain

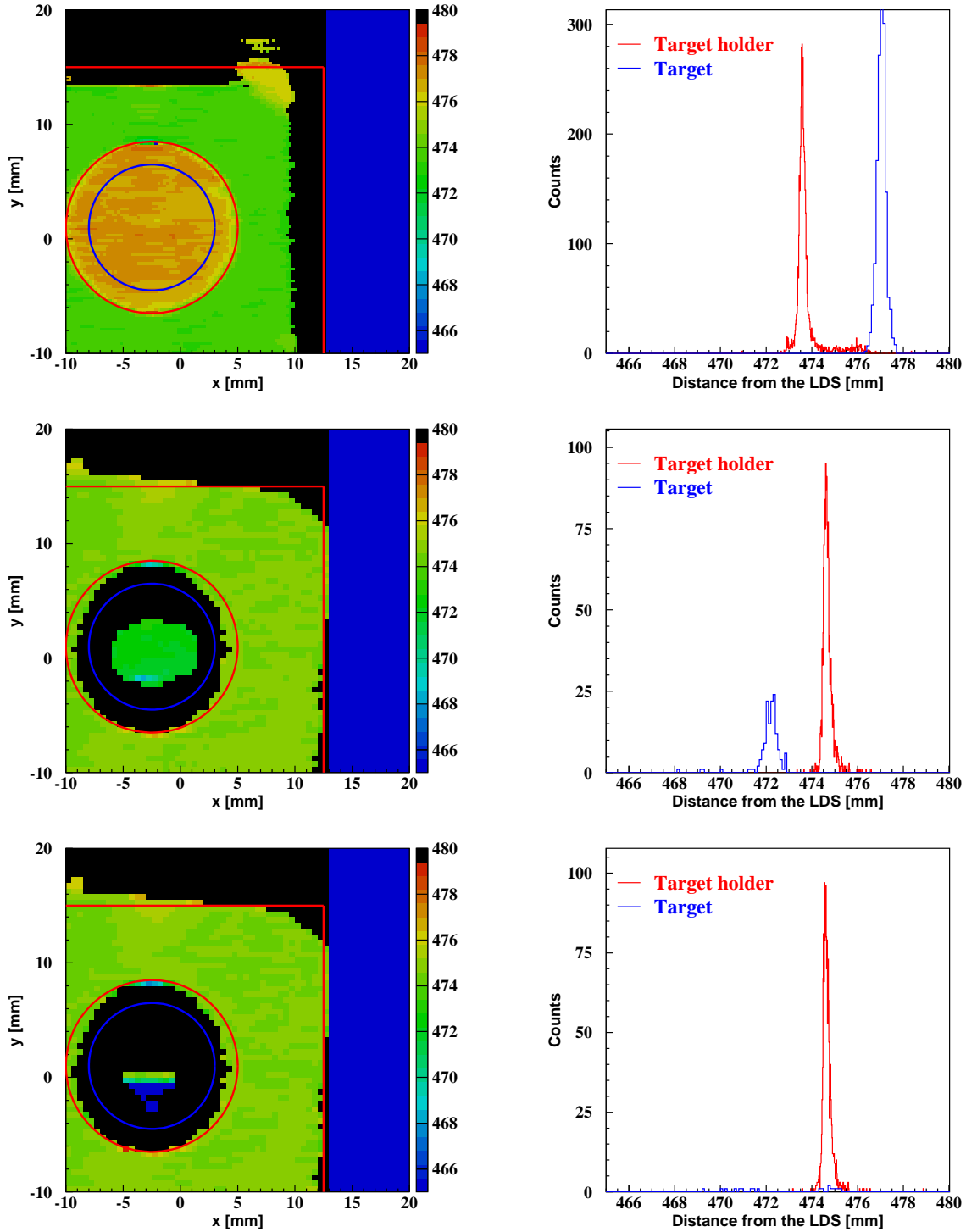


Figure 5.9: Typical results of the target scan with LDS for several targets. From top to bottom, targets are empty (only target holder), solid In and liquid In, respectively. The left column show the 2-D plot of the measurement result. The right shows the distance distributions of the target (blue) and target holder (red).

the metal density [36–39].

$$\text{In} : \rho = 7.023 \times \{1 - 9.323 \times 10^{-5} \times (T - 429.30)\}^{1/0.9607} \quad (5.7)$$

$$\text{Pb} : \rho = 10.678 - 13.174 \times 10^{-4}(T - 600.6) \quad (5.8)$$

$$\text{Sn} : \rho = 7.033 - 6.765 \times 10^{-4}(T - 505.1) \quad (5.9)$$

$$\text{Bi} : \rho = 10.021 - 11.820 \times 10^{-4}(T - 544.5) \quad (5.10)$$

In addition to In, Pb, Sn, and Bi, there are more metals suitable for liquid target as far as melting point and vapor pressure are concerned. We summarize these candidates in the table 5.3.

Table 5.3: Candidate for the target of liquid metal experiments.

Metal	Z	T_{melt} [K]	P_{melt} [Pa]
Li	3	453	2×10^{-8}
Na	11	371	2×10^{-5}
K	19	336	1×10^{-4}
Ga	31	303	6×10^{-36}
Rb	37	313	3×10^{-4}
Cs	55	302	3×10^{-4}
Hg	80	234	3×10^{-4}
Tl	81	577	4×10^{-6}

5.4.1 Stopping power

In this work, the stopping powers calculated by SRIM [40] are used with an interpolation. The stopping power of In, Pb, Sn, Bi for hydrogen are shown in Figure 5.4.1. These were used to the energy loss of the incident deuteron in the target. The stopping power of C and Al for hydrogen and helium are shown in Figure 5.4.1. The unit of x axis is keV/u for the hydrogen and keV/4u for the helium, here, u is a atomic mass unit. These were used to the energy loss in the absorbers.

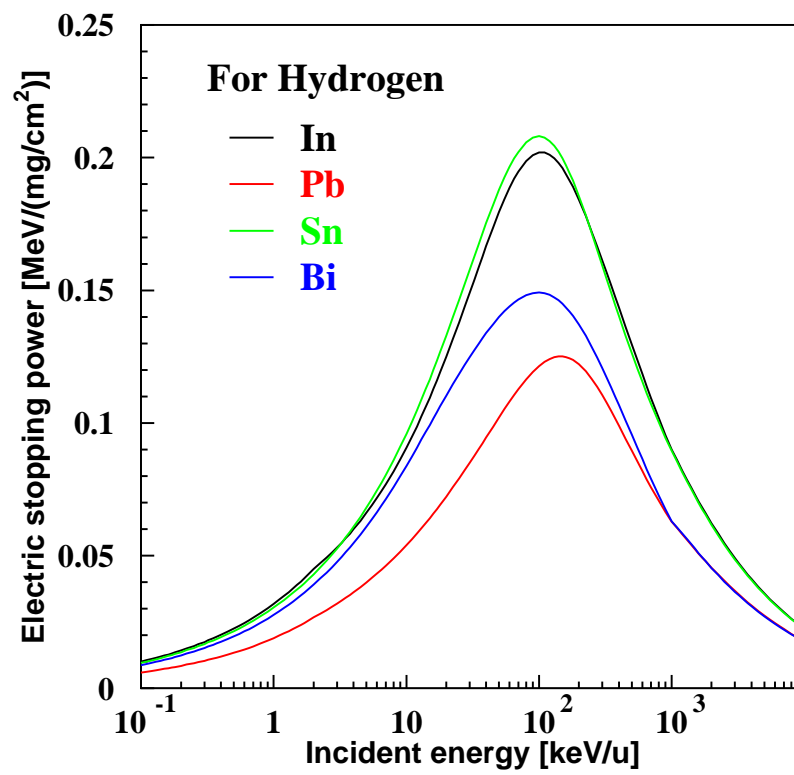


Figure 5.10: Stopping powers of various metals for hydrogen.

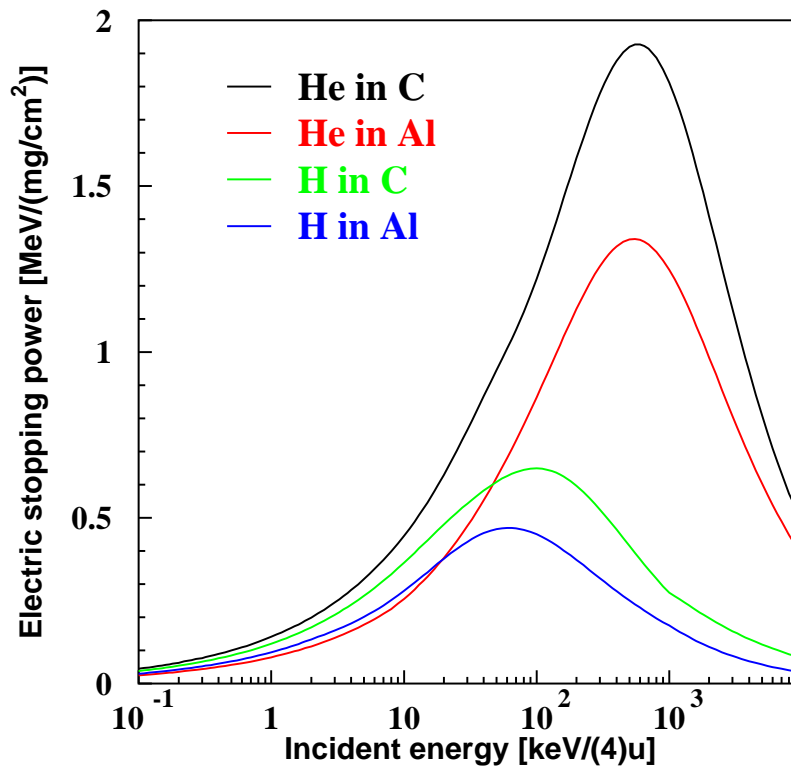


Figure 5.11: Stopping powers of the absorbers for a hydrogen and a helium. The unit of the x axis is keV/u for the hydrogen and keV/4u for the helium.

5.4.2 Target temperature

Temperature of the target is measured by a infrared radiation thermometer (IRT). In order to determine a temperature, IRT needs the emissivity of the target. The calibration of the emissivity is described in Appendix A.1 The temperature of the target are summarized in Table 5.4. Since the temperature rises due to the beam bombardment, the target temperature has dispersion of several tens of degrees depending on the beam energy and current. The dispersion in density due to the temperature change is less than 1 %, and the influence on the experiment yields is sufficiently small.

Table 5.4: Temperature of the target

Metal	Heater [W]	ϵ^2	T^2 [°C]	ϵ^1	T^1 [°C]	ρ [g cm ⁻³]
Indium	2×12.5	0.10	235 – 285	0.054	264 – 320	6.95 – 6.91
Lead	2×42.0	0.10	400 – 430	0.134	378 – 406	10.61 – 10.57
Tin	2×17.0	0.10	360 – 400	0.035	438 – 489	6.89 – 6.86
Bismuth	2×17.0	0.10	330 – 370	0.119	320 – 358	9.96 – 9.92

5.5 Solid angle

In order to obtain the precise solid angle Ω , we measured the yield of α -particles emitted from the ²⁴¹Am source. The trigger rates R_α made by α particles were measured for each experimental setup. The solid angle between the detector and emitter, Ω_E , is given by the expression, $\Omega_E = R_\alpha/A$. Here, A is a radioactivity of the emitter. The A is determined by R_α^{WE} which is a trigger rate for a well-established setup described as follow. A distance between the surface of the emitter and a silicon detector whose active area is 200 mm² is 299.5 ± 1 mm. A aperture with a diameter of 4.95 ± 0.02 mm is placed at the 3.0 mm front of the detector. The emitter is placed at right under the center of the detector and the aperture with ambiguity of 1 mm for horizontal direction. Since the size of the aperture is greatly smaller than the active area of the detector, the Ω_E^{WE} only depends on the distance, h , between the aperture

and the emitter and the diameter of aperture, $2r$. The Ω_E^{WE} is given by expression ,

$$\Omega_E^{\text{WE}} = 2\pi \left(1 - \frac{h}{\sqrt{h^2 + r^2}} \right). \quad (5.11)$$

The results of a measurement of R_α^{WE} and calculated $\Omega_E^{\text{WE}}/4\pi$ are $(9.58 \pm 0.11) \times 10^{-2} \text{ s}^{-1}$ and $(1.742 \pm 0.037) \times 10^{-3} \%$.

Measurements of the R_α are performed for In and Pb target experiment. The α emitter is placed on the center of the target holder with ambiguity of approximately 0.2 mm for horizontal direction. The measured R_α for In and Pb target are $155.15 \pm 0.40 \text{ s}^{-1}$ and $155.20 \pm 0.35 \text{ s}^{-1}$, respectively. Ω_E is calculated as

$$\Omega_E = \Omega_E^{\text{WE}} \frac{R_\alpha}{R_\alpha^{\text{WE}}}. \quad (5.12)$$

Since the emitter has a thickness of 0.55 mm, the difference of Ω_E and Ω with the designed setup was calculated by Monte Carlo method. Finally, Ω are obtained. These results are summarized in Table 5.5. For the experiment with Sn and Bi target, R_α measurements were not performed.

Table 5.5: The trigger rates, R_α , and total solid angle, Ω , of the detectors for various setups

Setup	$R_\alpha^{\text{WE}} [\text{s}^{-1}]$	$\Omega_E^{\text{WE}}/4\pi [\%]$	$\Omega/4\pi [\%]$
Well-established	0.0958 ± 0.0011	$(1.742 \pm 0.037) \times 10^{-3}$	–
Setup	$R_\alpha [\text{s}^{-1}]$	$\Omega_E/4\pi [\%]$	$\Omega/4\pi [\%]$
Indium	155.15 ± 0.40	2.822 ± 0.068	2.762 ± 0.067
Lead	155.20 ± 0.35	2.823 ± 0.068	2.763 ± 0.067

5.6 Data acquisition system

The data acquisition (DAQ) is performed by NIM and CAMAC modules which are controlled by a personal computer through a CAMAC create controller. The energy of the particles, integrated charge incident on Faraday cup and measurement time

is obtained. The DAQ is designed to repeat the cycle of the beam bombardment (beam on) and the current measurement (beam off) by turns. The cycle of DAQ is summarized in Table 5.6. The integrated charge and measurement time is recorded by every cycle.

Table 5.6: Cycle of the data acquisition.

Beam On	Wait for insertion	Beam Off	Wait for ejection
10 sec	1 sec	3 sec	1 sec

5.6.1 Block diagram for energy measurement

Figure 5.12 shows the block diagram of the measurement. It consist of silicon detectors, pre-amplifiers, amplifiers and an analog-to-digital converter. The electric signal is amplified and shaped by Pre-amplifier, ORTEC 142C, and Amplifier, ORTEC 572A. The Amplifier outputs a uni-polar and bi-polar signal whose pulse height are proportional to the deposit energy. A uni-polar signal from the amplifier goes into a analog-to-digital converter (ADC), Ortec AD811, which obtain the height of the pulse.

A bi-polar signal from the amplifier goes into a trigger system. When the bi-polar signal exceeds a threshold of Discriminator-1, Ortec 928, a request signal is generated. A Fan-in/Fan-out, Kaizu works KN490, summarizes the request signal from detector 1 and 2, and a accept signal, which starts the data acquisition, is generated by Discriminator-2, LeCroy 821. During a data acquisition and reading out, the generation of the accept signal is refused by a veto signal from the Gate Generator-2, Technoland TKY-0240. This veto signal is released after the reading out of the data is finished.

In order to identify which detectors makes the accept signal, time differences between the accept signal and delayed request signals from the Discriminator-1 are recorded by a Time-to-Digital-Converter, LeCroy 2228A.

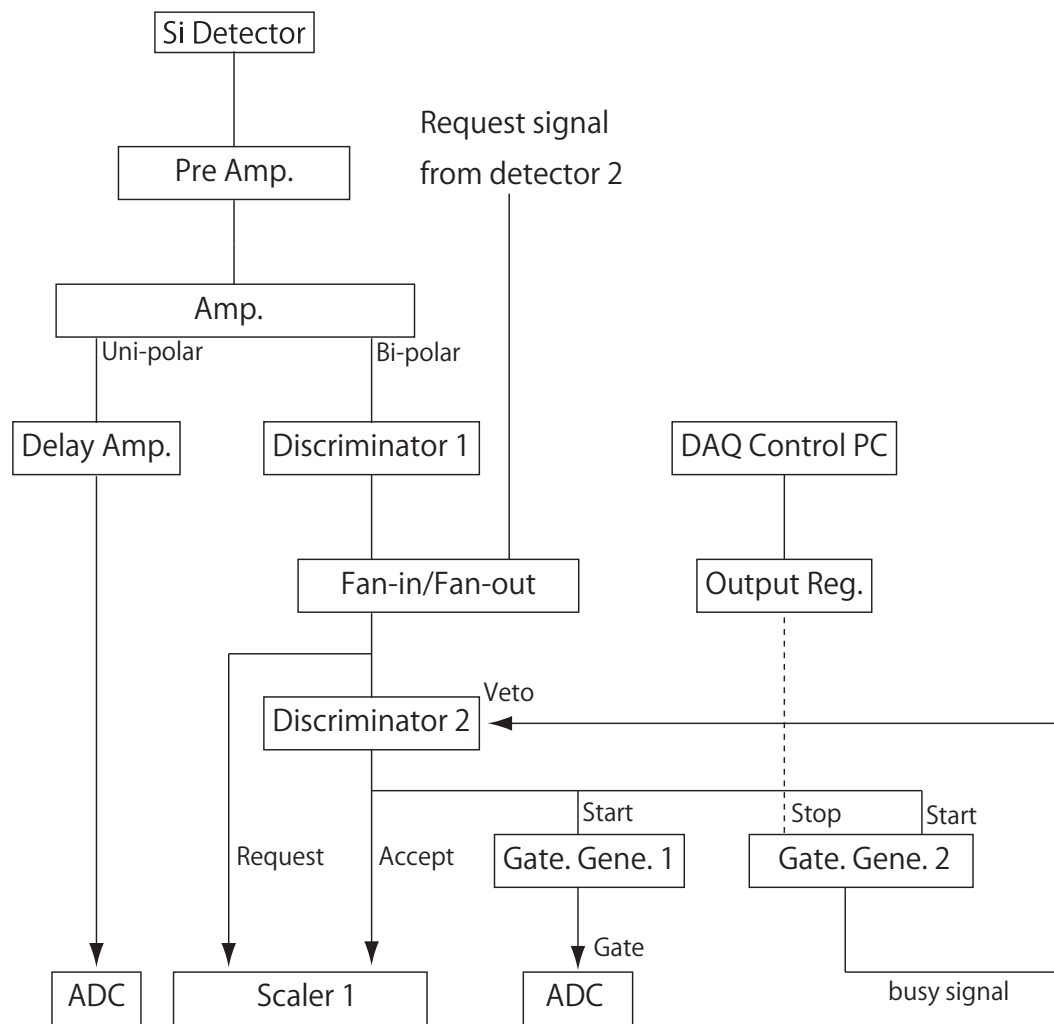


Figure 5.12: Block diagram for the energy measurement.

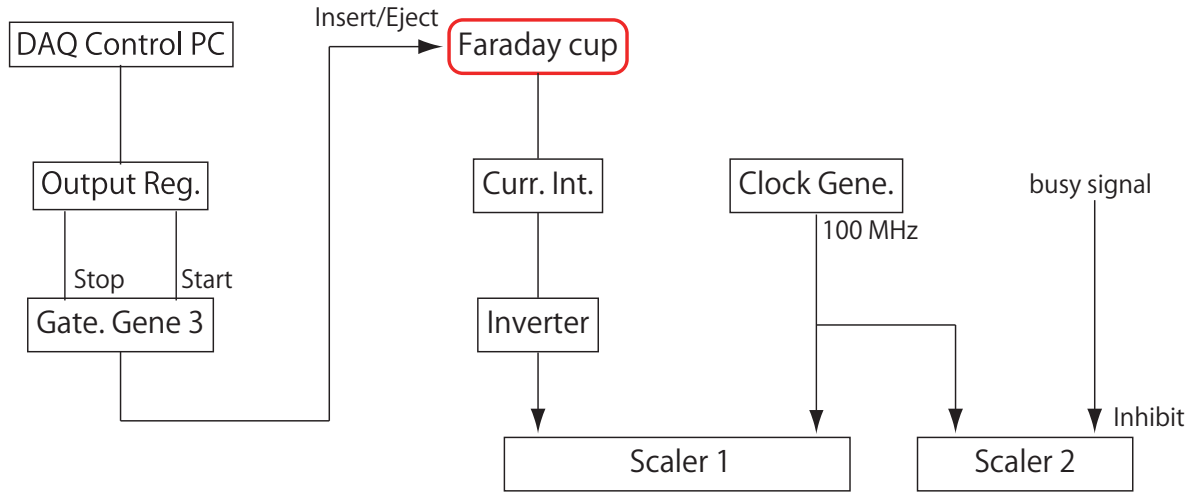


Figure 5.13: Time and Current measurement system.

5.6.2 Block diagram for time and current measurement

Figure 5.13 shows a diagram of time and current measurement. The incident charge on a target, Q_1 , the time of the current measurement, T_2 , and beam irradiation, T_1 , are necessary as well as integrated charge, Q_2 , incident on Faraday cup. T_1 and T_2 are obtained by counting the number of 100 MHz clock signal with CAMAC Scaler. The clock signal is generated by a Clock Generator, Tcnoland N-TM 203. Two CAMAC scaler, LeCroy 2551 and Tcnoland C-TS 203 are employed to obtain both the total and live time. An electric charge which is incident on the Faraday cup is converted to logic signals, and the signals are also counted by the CAMAC Scaler.

Chapter 6

Experimental results and analysis

In this section, reaction yields and energy spectra of $d + d$ reaction with CCM are extracted from experimental data.

6.1 Raw spectra

Typical energy spectra for liquid and solid In target are shown in Figure 6.1 and 6.2. The beams for both target are D_3^+ ion with the total energy of 60-keV. Three bumps corresponding to ^3He particles, tritons and protons emitted from the $d + d$ reaction are clearly observed. However, there is an entirely difference in the shape of the bumps between for liquid and solid target.

The energy spectrum for the solid target has narrow peaks. The peak consist of normal $d + d$ reactions which is occurred by a rest deuteron and beam deuteron. On the other hand, the bumps of the spectrum for the liquid target have a double peak structure. It consist of the wide peak by the CCM and narrow peak by the background from the absorber, we call it absorber background which is discussed in § 6.2.2. The difference in spectral shape for the liquid and solid target is due to the deuteron density in the metal. When the deuteron density is enough high, the

normal $d + d$ reaction becomes dominant. The reaction makes narrow peaks shown in the spectra for solid metal target. On the other hand, the CCM becomes dominant when the deuteron density is low. As the target deuteron has a large kinetic energy corresponding to the beam energy, CCM makes wide bumps shown in the spectra for liquid metal target, which is discussed in Section 4 in detail. The deuteron density in the liquid and solid metal is discussed in Section 6.2.

The raw spectra for the liquid In and Pb target with a total incident energy of 10, 30, 45 and 60 keV are shown in Figure 6.3 and 6.4. The shape of the CCM spectra for the In and Pb seems to be the same. The width of the CCM spectra becomes short as the incident energy decreases, but the peak position is almost constant. The contribution from the absorber background decreases, as the incident energy decreases, and it almost diminishes at the $E_{D_3^+} = 30$ keV. For the spectra of $E_{D_3^+} = 10$ keV, a large bump is seen at the region of 100–500 ch where corresponds to the energy of the triton and ^3He particle. The bump consist of the thermal noise of the detector, which is described in § 6.2.1. The contribution becomes large at the lower incident energy because of the low $d + d$ reaction rate.

6.2 Background event

In order to obtain the $d + d$ reaction yields for the CCM, the background events should be considered. The spectra for the liquid metal target include three kinds of major backgrounds. The first is a thermal noise of the silicon detector. Since the noise results from thermal agitation of the charge carriers, it occurs whether there are beam bombardments or not. The noise lies around the low-energy region such as the regions of ^3He and triton peaks. The second are absorber background. The absorber background originates from the scattered beam by metal atom. The scattered deuterons hit to the absorber, and they become serve as incident and target deuteron of the $d + d$ reaction. Since the emission angles of the detected particles are forward, the energy of the emitted particles for the absorber background is higher than the energy of the bumps of CCM. The third is the normal $d + d$ reaction. Even if using a liquid metal as the target, a small amount of deuterons can be accumulated in the metal. These deuterons become target of the normal $d + d$ reaction. It makes peaks at the middle of each bump of the CCM. We call it the rest target background. Result

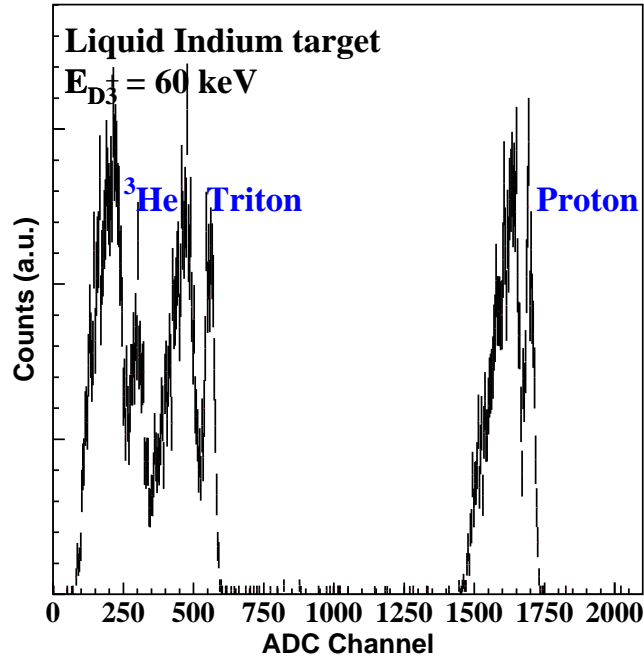


Figure 6.1: Raw spectra for the liquid indium target with the D_3^+ beam.

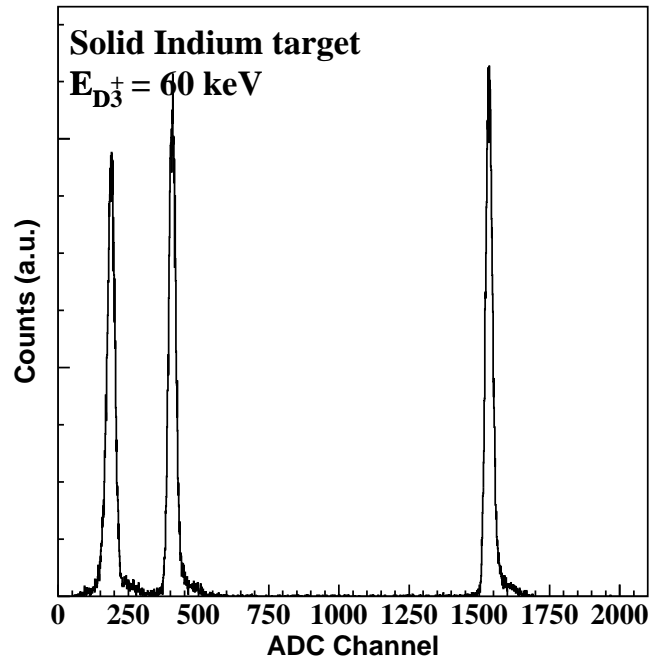


Figure 6.2: Raw spectra for the solid indium target with the D_3^+ beam.

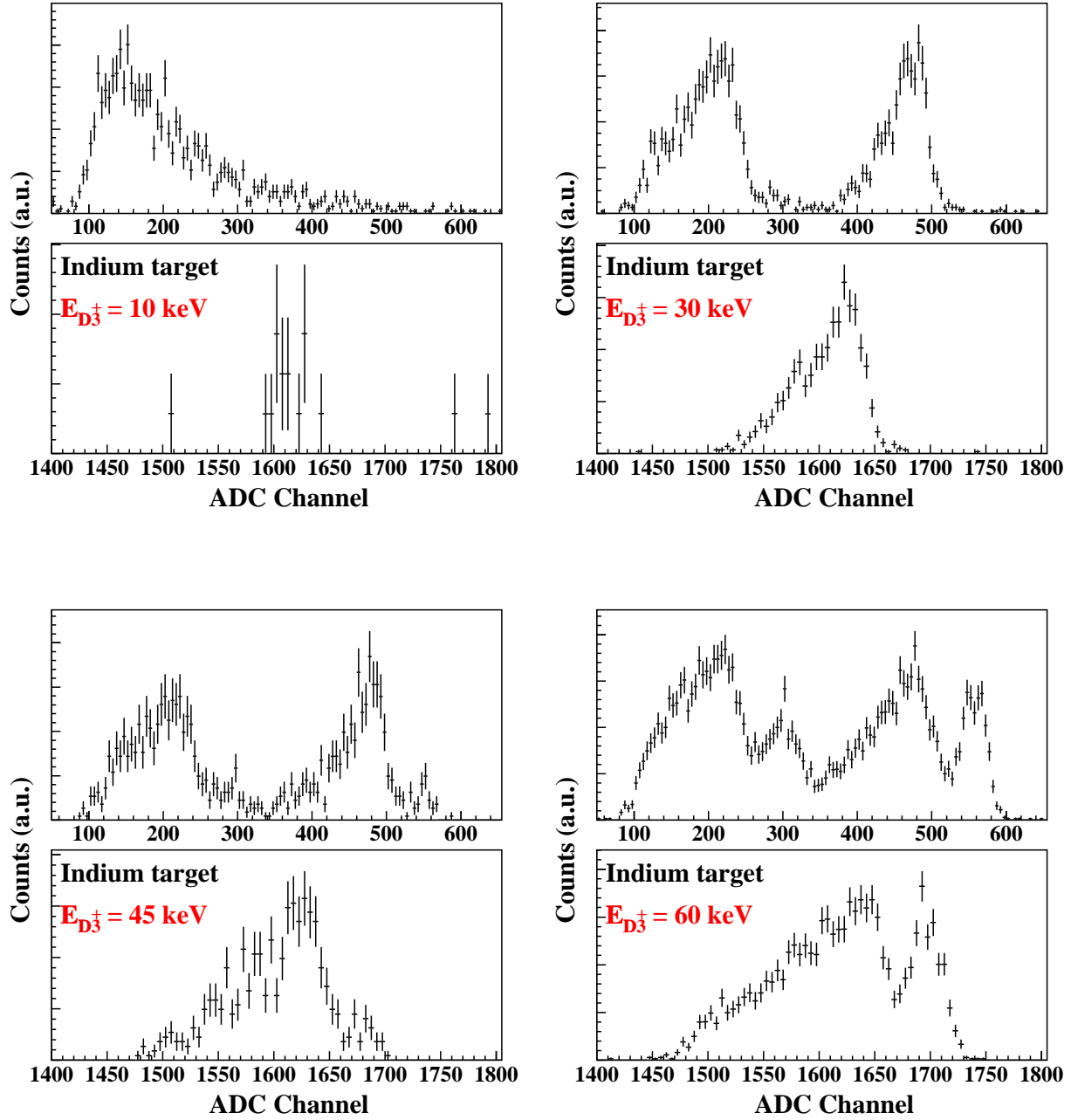


Figure 6.3: Raw energy spectra for the liquid In target with the D_3^+ beam for the total incident energies of 10, 30, 45 and 60 keV.

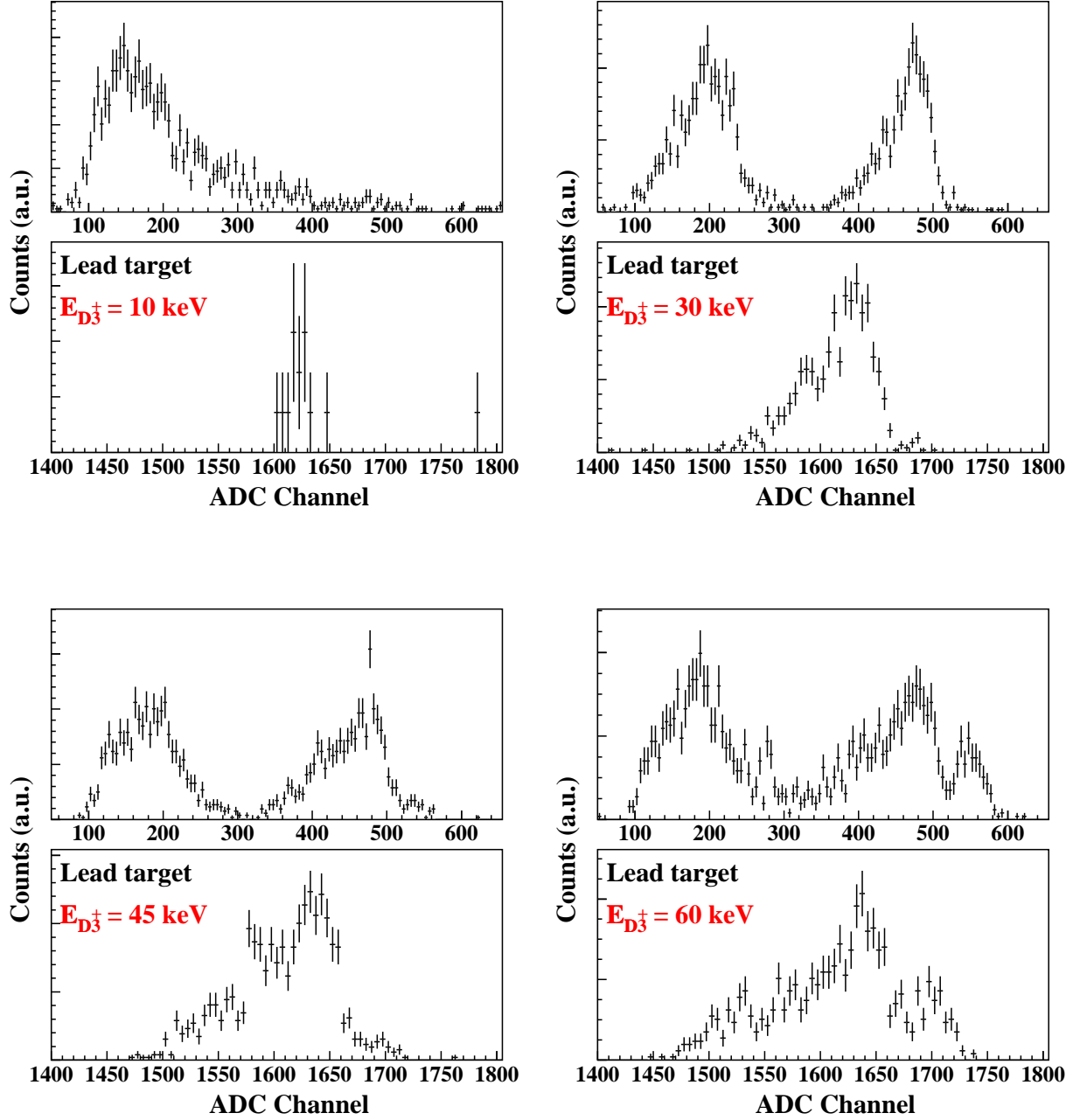


Figure 6.4: Raw energy spectra for the liquid Pb target with the D_3^+ beam for the total incident energies of 10, 30, 45 and 60 keV.

from the analysis, it is found that the contribution from the rest target background is sufficiently small. The deuteron density during the beam bombardment is estimated to be $1 \times 10^{17} \text{ cm}^{-3}$. The contribution to the yield of CCM is less than 1 % at the maximum. Therefore, we ignored the contribution. The estimation of the contribution and density is described in § B.1.

By considering these backgrounds, the yields and spectra of CCM were extracted from the experimental data. The thermal noise and absorber background described in § 6.2.1 and 6.2.2, respectively.

6.2.1 Thermal noise

The pulse height distribution and the yield of the thermal noise depend on temperature of the detector. Therefore, the detector is cooled down to reduce the noise. In the measurements, the current measurement and the beam bombardment are alternately switched in a short time. If the temperature change of the detector is gentle, the spectra obtain current measurement are spectra of the thermal noise. Therefore, the spectra at the current measurement was normalized by the measurement time, and subtracted from the foreground measurement. Typical spectra are plotted with the thermal noise in Figure 6.5.

6.2.2 Absorber background

The energy spectra of each particles have a wide bump and a narrow peak, which can be seen in Figure 6.5 for incident energies higher than 30 keV. The narrow peak is attributed to the $d+d$ reaction at the absorber. Figure 6.6 shows an illustration of the absorber background, originates from the deuterons scattered by metal atoms. The scattered deuterons are accumulated in the absorber, and become the target of the $d+d$ reaction. Therefore the yield almost diminishes just after changing the absorber, increases as the measurement proceeds.

The yield and the energy spectra were calculated using Monte Carlo method. The detail of the calculation is written in § C.1. A calculated energy distribution for the In target with $E_0 = 20 \text{ keV}$ is shown in Figure 6.7. A sharp peaks similar to the energy spectra for solid target are seen. Since the charged particles are emitted forward, their energies are larger than these for solid target.

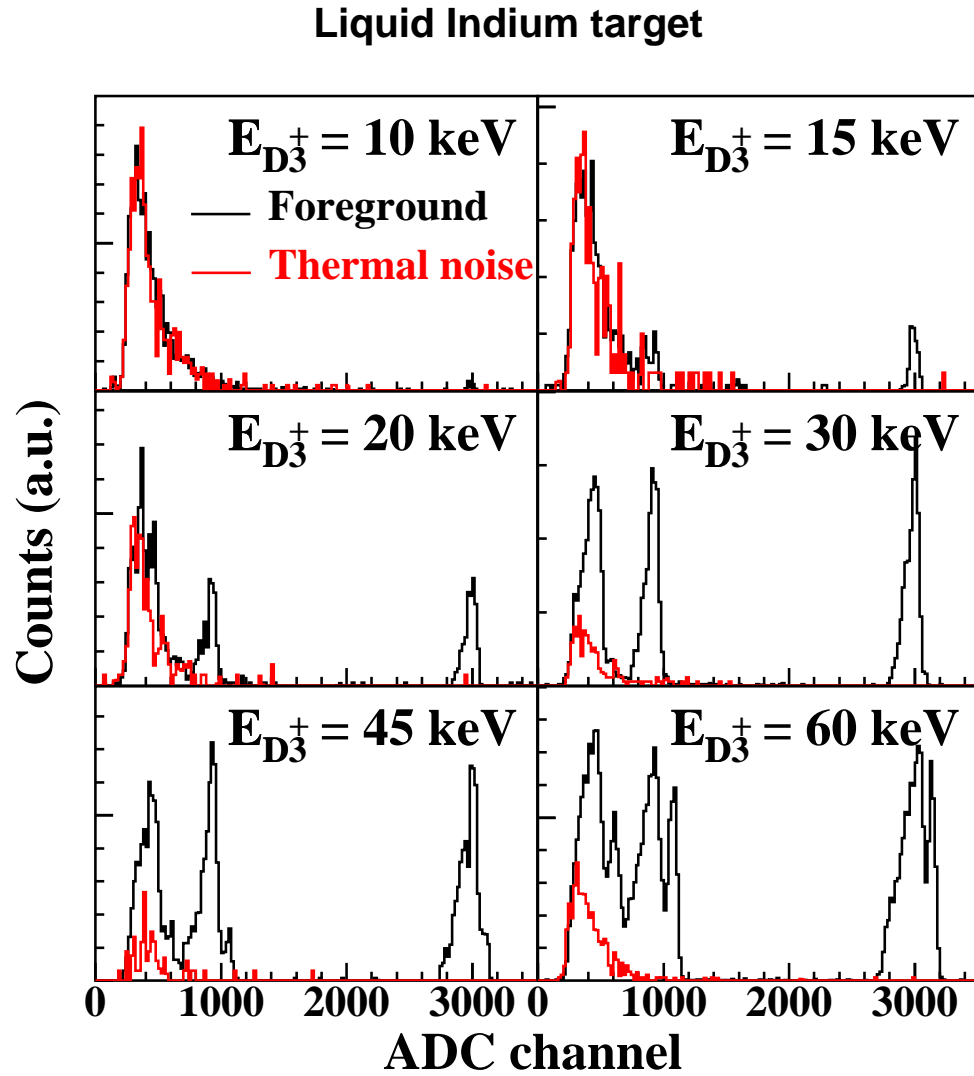


Figure 6.5: Energy spectra of foreground and thermal noise for liquid In target with incident energies of 10, 15, 20, 30, 45 and 60 keV.

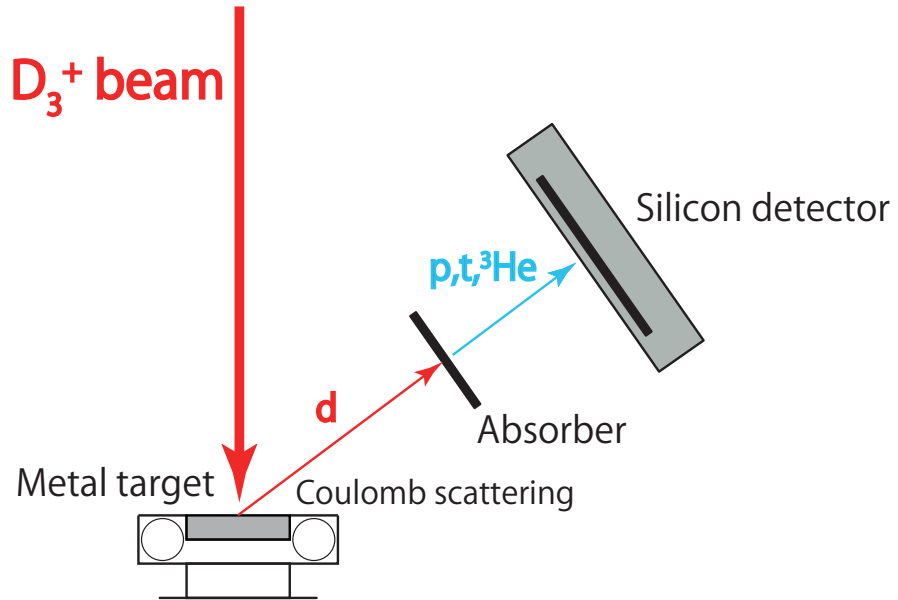


Figure 6.6: Briefly illustration of the absorber event.

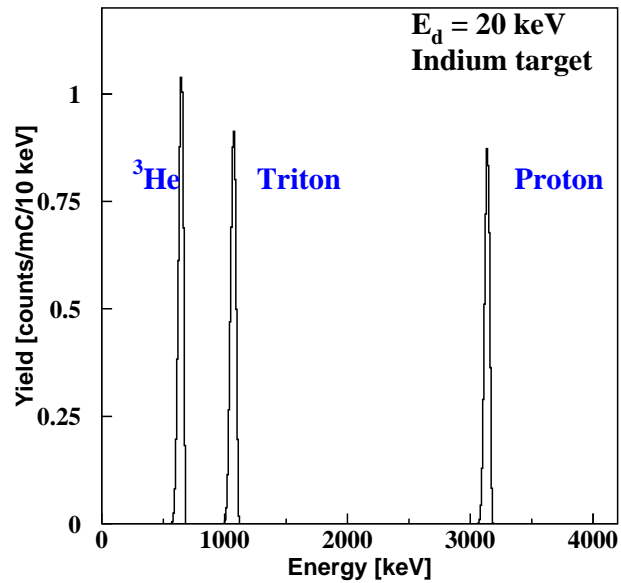


Figure 6.7: Energy spectra of the absorber event for In target with incident energy of 20 keV.

The excitation function of each charged particle emitted from the absorber is shown in Figure 6.8 with the CCM yield. The yield of the absorber background decreases faster as compared to that of CCM. Although not clearly seen in the figure, the magnitude of the yield is the order of ^3He particle, triton and proton. This is due to the difference in the detector solid angle of the CM system. The yield ratios of triton and ^3He to proton are shown in Figure 6.9.

If the thickness of the absorber increase by vapor deposition or sputtering, the spectrum shape of the absorber background does not match the calculated one. The absolute value of the yields is also difficult to estimate because the deuteron density depends on run. However, the yield ratio of each particle is not dependent on those factors and is reliable. Using the yields ratio, we estimated the yield of the absorber background.

First, fitting each bump with the sum of the spectrum shape $F_i(E)$ corresponding to the CCM and $G_i(E)$ corresponding to the absorber background. Here, $i = p, t$ and h , which represent proton, triton, and ^3He , respectively. $F_i(E)$ is obtained by convolving a right triangle shape $F_i^t(E)$ with Gaussian function $F_i^g(E)$. Each formula is described below.

$$F_i^t(E) = \begin{cases} c_i(E - a_i) & (a_i \leq E \leq b_i) \\ 0 & (\text{otherwise}) \end{cases}$$

$$F_i^g(E) = \frac{1}{\sqrt{2\pi}d_i} \exp\left(-\frac{E^2}{2d_i^2}\right)$$

From these functions, $F_i(E)$ is obtained as

$$F_i(E) = \int F_i^t(\tau) F_i^g(E - \tau) d\tau$$

$$= c_i \left[-d_i^2 \exp\left\{-\frac{(E - \tau)^2}{2d_i^2}\right\} - \sqrt{\frac{\pi}{2}} d_i (a_i - E) \text{erf}\left(\frac{\tau - E}{\sqrt{2}d_i}\right) \right]_{a_i}^{b_i}. \quad (6.1)$$

$F_i(E)$ reproduces the shape of the CCM well. The absorber background is approximated by the Gaussian distribution,

$$G_i(E) = e_i \exp\left(-\frac{(E - f_i)^2}{2g_i^2}\right). \quad (6.2)$$

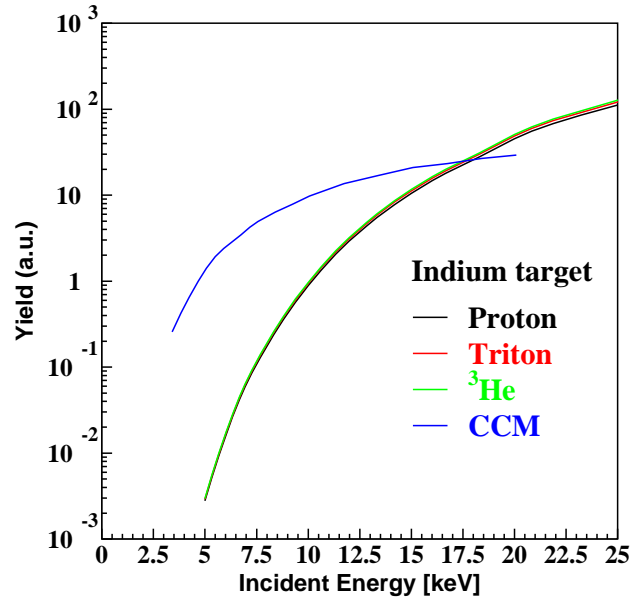


Figure 6.8: Excitation function of the absorber event and CCM for In target.

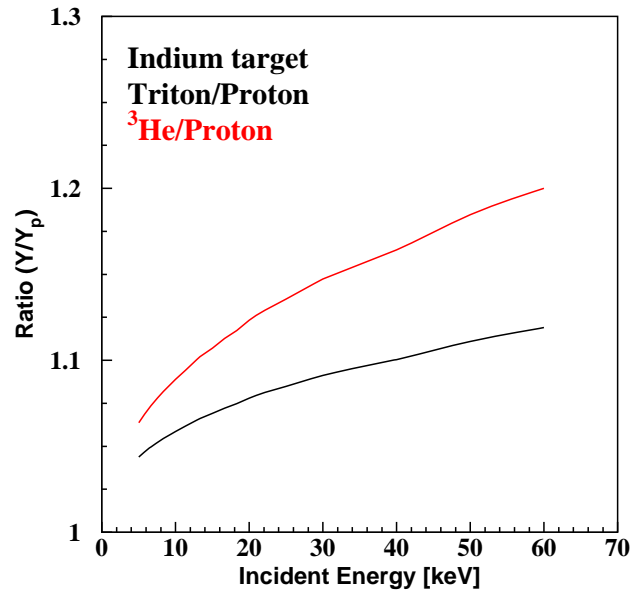


Figure 6.9: The yield ratios of triton and ^3He to proton of absorber background.

Here, $a_i \sim f_i$ are all fitting parameters. Each bump are fitted by $F_i(E) + G_i(E)$ with seven fitting parameters. Since the calculated yield ratio is used for the parameter of $G_i(E)$, there are following relations,

$$e_t = e_p \frac{g_p}{g_t} R_{pt} \quad (6.3)$$

and

$$e_h = e_p \frac{g_p}{g_t} R_{ph}. \quad (6.4)$$

Here, R_{pt} and R_{ph} are calculated yield ratio of triton/proton and ^3He /proton, respectively. Finally, fitting with 19 parameters for the all region of the energy spectrum is performed. A result of the fitting for the In target with the incident energy of 20 keV is shown in Figure 6.10. The amount of absorber background was estimated and subtracted from the Gaussian distribution. In addition, the mean values of the absorber background obtained from the fit were used for the energy calibration. The detail of the calibration is described in § D.1.

6.3 Energy spectra

The energy spectra for the liquid In and Pb target with a total incident energy of 10, 30, 45 and 60 keV are shown in Figure 6.11 and 6.12. The background contributions from the thermal noise and the absorber background are subtracted.

6.4 Yield

In this section, yield of the $d+d$ reaction with CCM is obtained from the experimental data.

6.4.1 Integral region

After subtracting the background, the bumps of proton, triton and ^3He are clearly separated, and the integral region can be determined visually. However, in the measurement of $E_{D_3^+} < 15$ keV, the yield was small and it was difficult to determine the region in triton and ^3He where thermal noise overlapped. Therefore, the region for

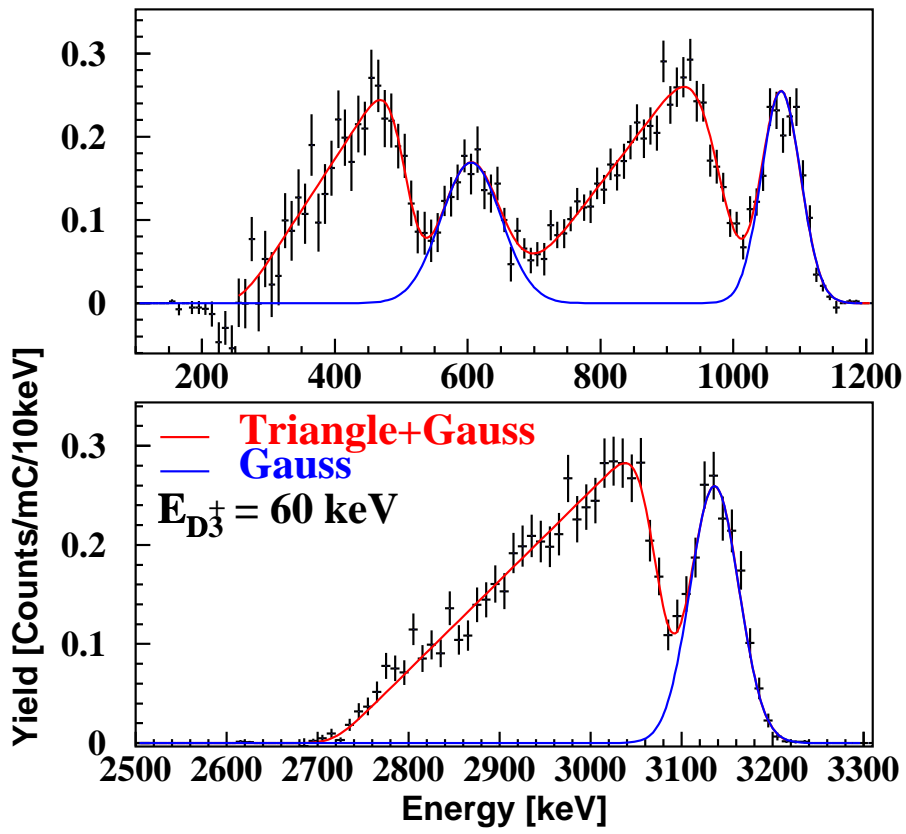


Figure 6.10: Fitting result of CCM and absorber background.

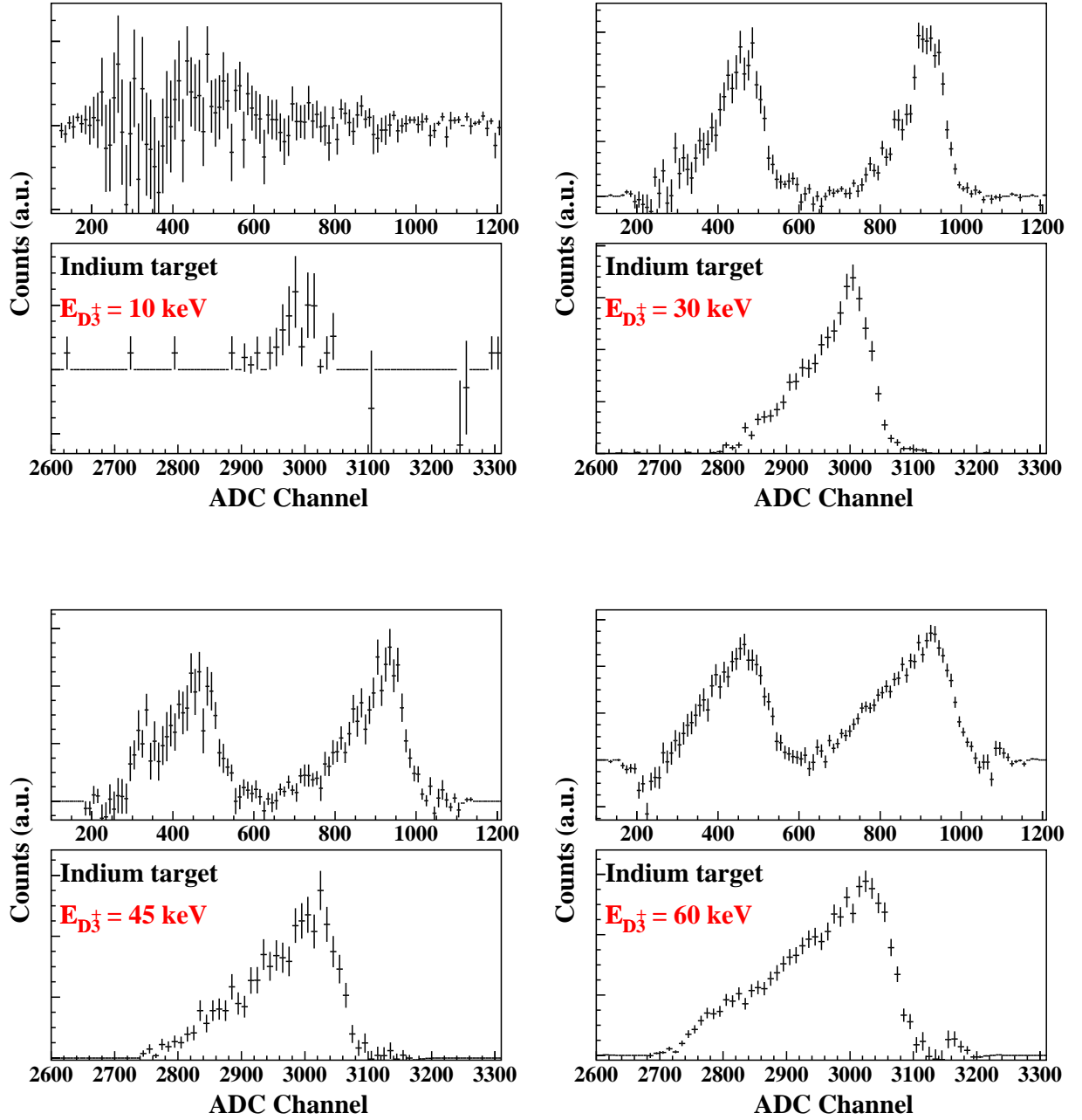


Figure 6.11: Energy energy spectra for the liquid In target with the D_3^+ beam for the total incident energies of 10, 30, 45 and 60 keV.

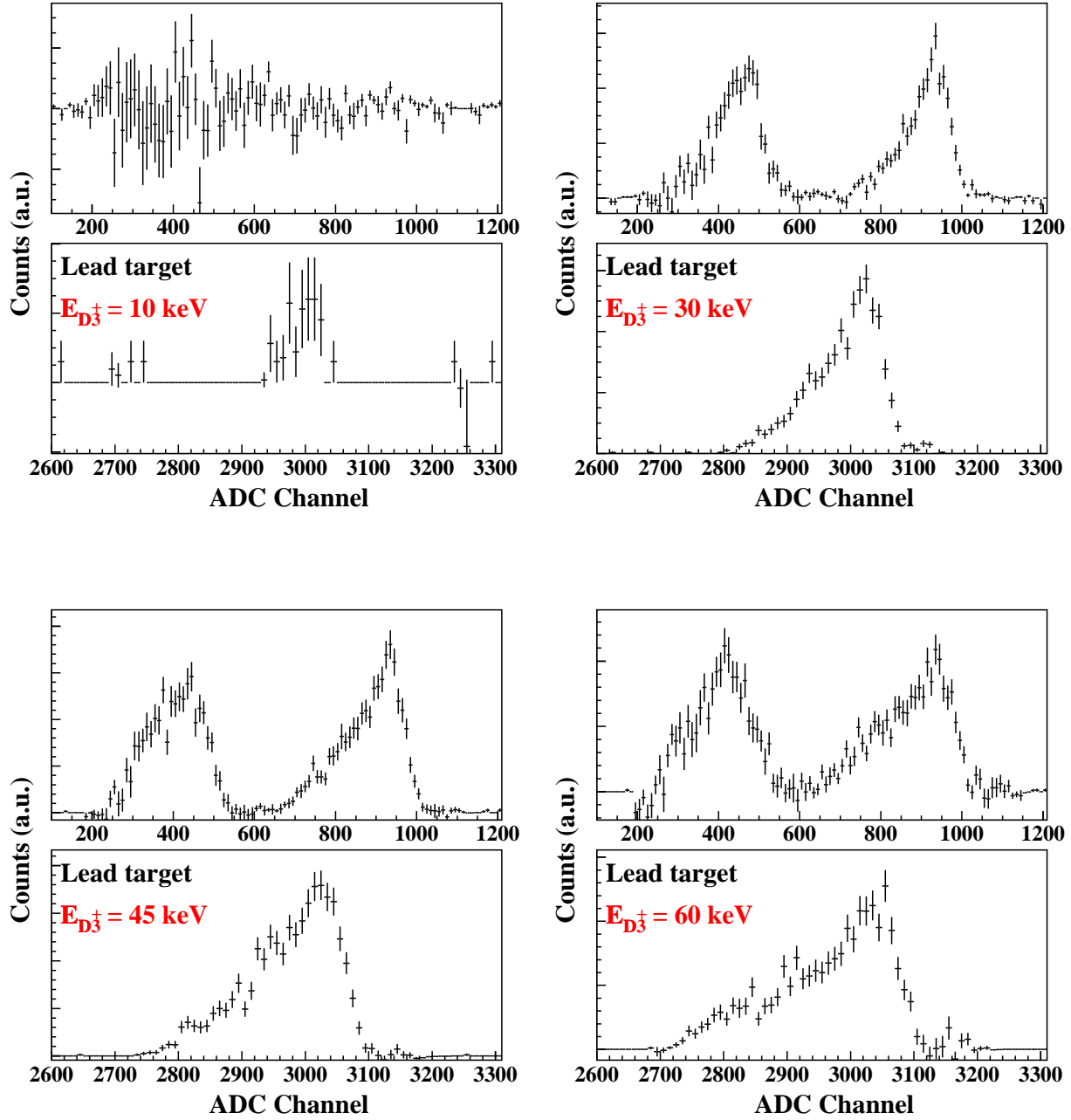


Figure 6.12: Energy energy spectra for the liquid Pb target with the D_3^+ beam for the total incident energies of 10, 30, 45 and 60 keV.

the closest energy that can be determined was used for the region of them. Examples of the integration region are shown in Figure 6.13. Each row represents the incident energy of 3.3, 5.0, 10.0 and 20.0 keV, respectively, and, each column for ^3He , triton and proton. The blue lines show the background subtracted spectra, and the dashed red and black lines indicate the lower and higher limit of the integral region. The solid red and black lines indicate a statistical error of the data in the region of interest.

6.4.2 Excitation function

The experimental yields of the $d + d$ reactions with CCM for In and Pb target are shown in Figures 6.14, and that for Sn and Bi target are shown in Figure 6.15. The yields of proton, triton and ^3He are described in black circles, red squares and green triangles, respectively. The yield of ^3He seems to be lower than the other at the higher energy. That is because the low-energy tail of the ^3He became broader as the incident energy increased, and it became lower than the threshold of the DAQ.

The yield of proton, triton and ^3He for every target are shown in Figures 6.16, 6.17 and 6.18, respectively. The black points, red squares, green triangles and blue down-pointing triangles represent the yield for Pb, In, Bi and Sn target experiments, respectively. The yield for In and Sn, and Pb and Bi are almost the same. On the other hand, the Yield for In or Sn, and Pb or Bi are greatly different. That is because the yield depends on the atomic number of the target.

The yield $Y(E_d)$ is obtained by the following

$$Y(E_d) = \frac{T^B}{\Omega Q^B T^F} \left(N^F - \frac{T^F}{T^B} N^B - N^G \right), \quad (6.5)$$

with

$$\begin{aligned} N^{F/B} &= \omega \sum_{\epsilon=\epsilon_{\min}}^{\epsilon_{\max}} f^{F/B}(\epsilon) \\ N^G &= \int_{\epsilon_{\min}}^{\epsilon_{\max}} G(\epsilon) d\epsilon \end{aligned} \quad (6.6)$$

Here, ω is the solid angle correction factor of each run calculated in § E.1.2, $f^F(\epsilon)$ and $f^B(\epsilon)$ are energy spectra of detected particles at beam bombardment and current

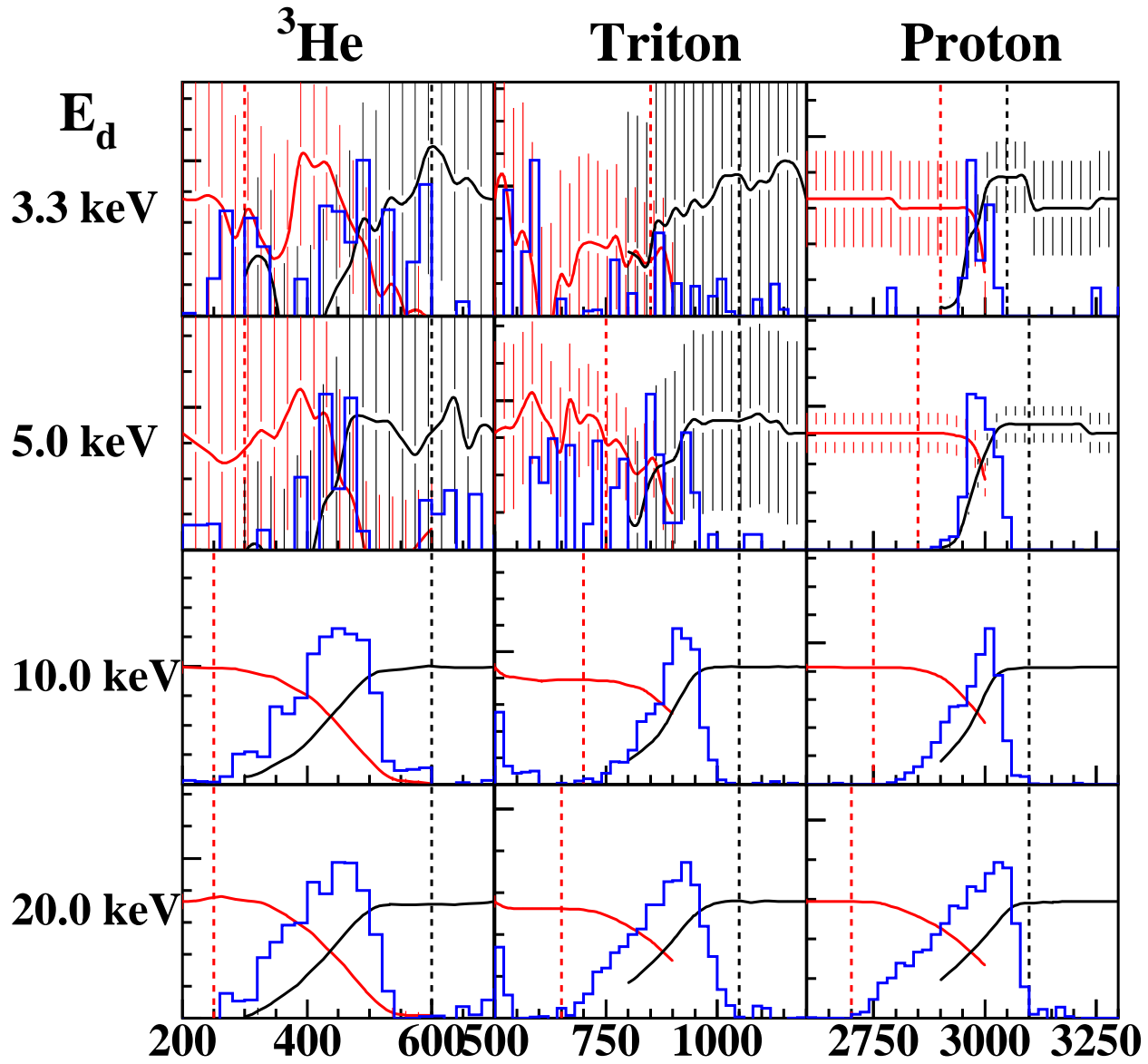


Figure 6.13: Integral region of the each energy spectrum.

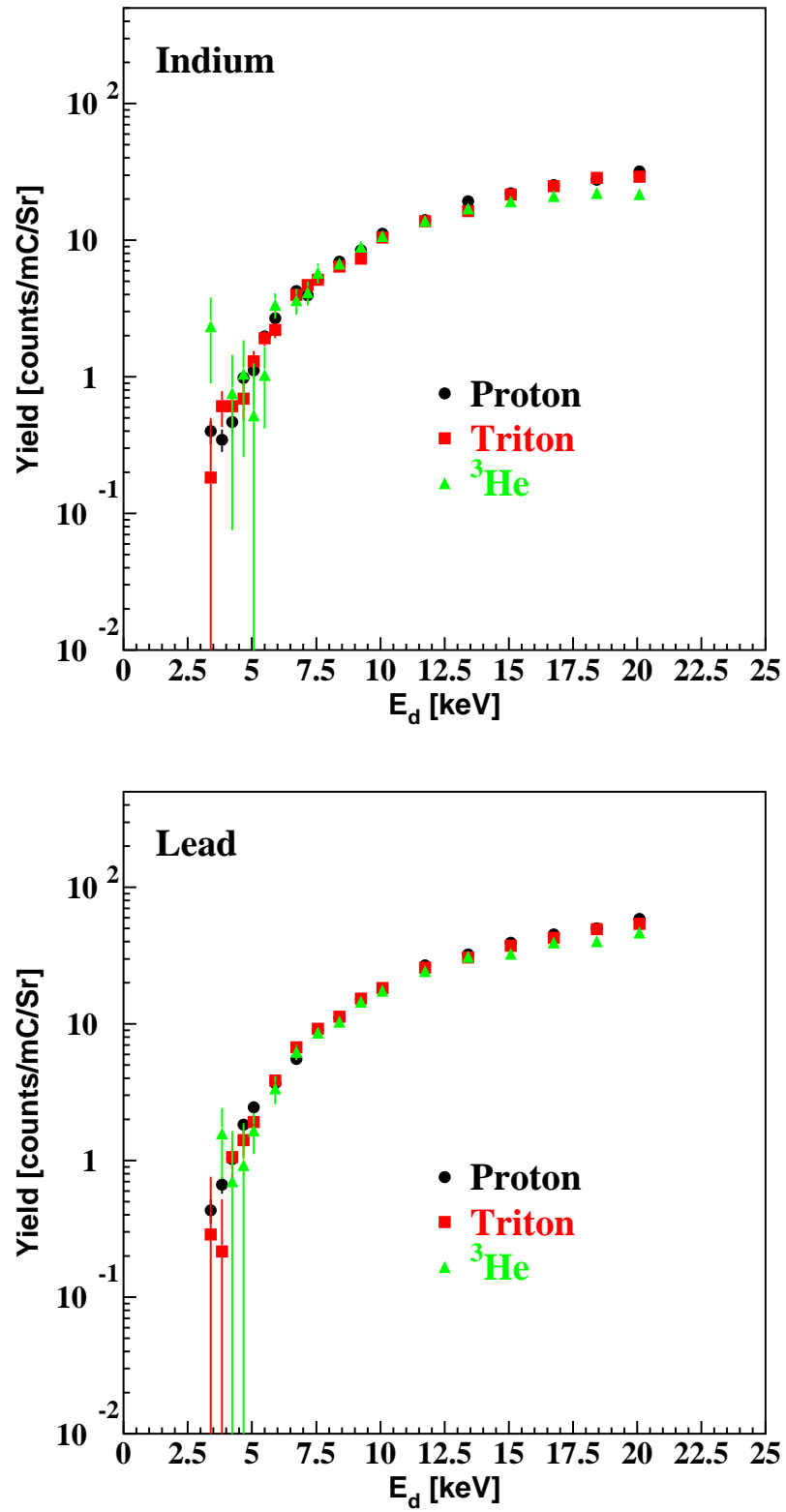


Figure 6.14: Excitation function of the $d + d$ reaction with CCM for In and Pb target experiment.

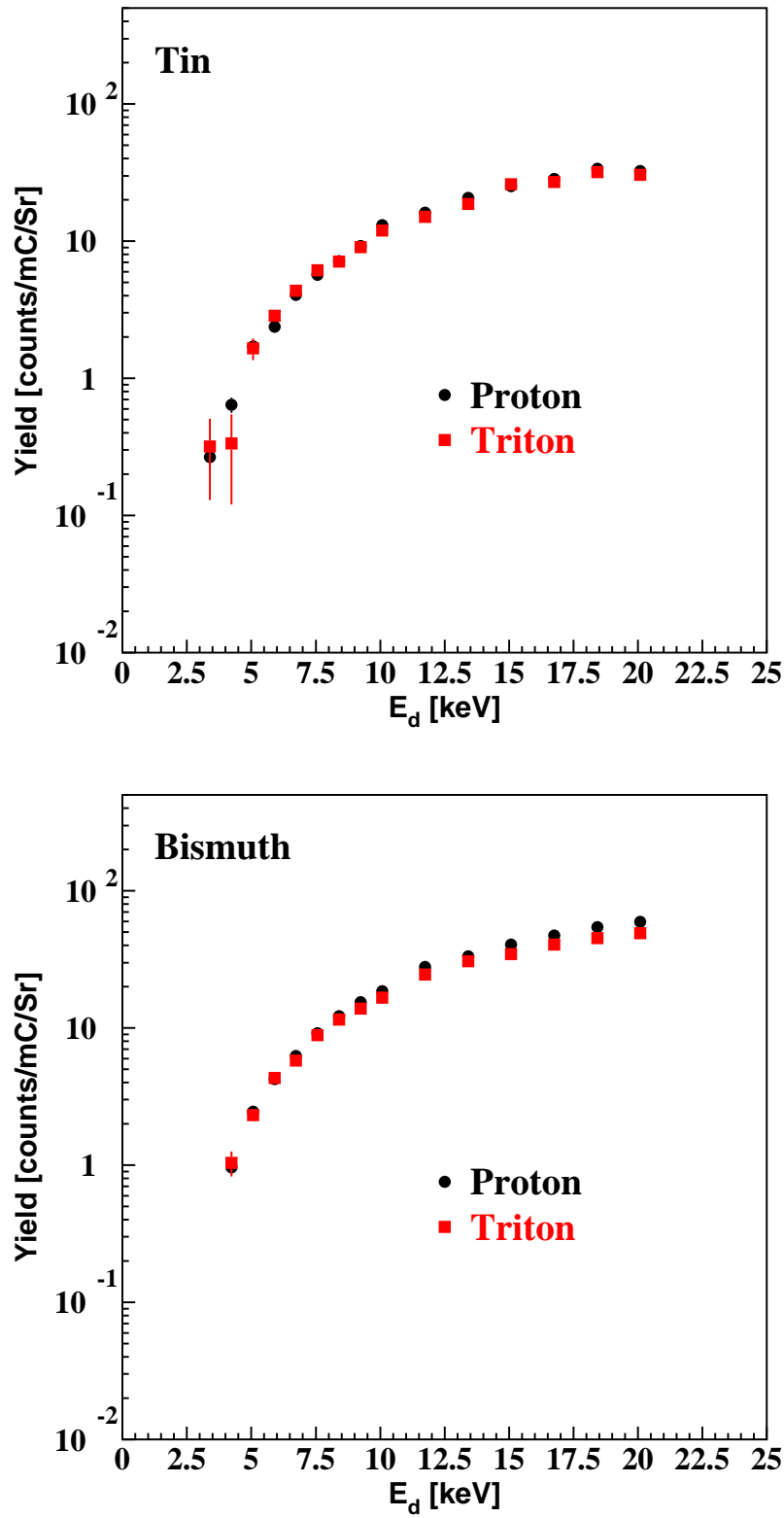


Figure 6.15: Excitation function of the $d + d$ reaction with CCM for Sn and Bi target experiment.

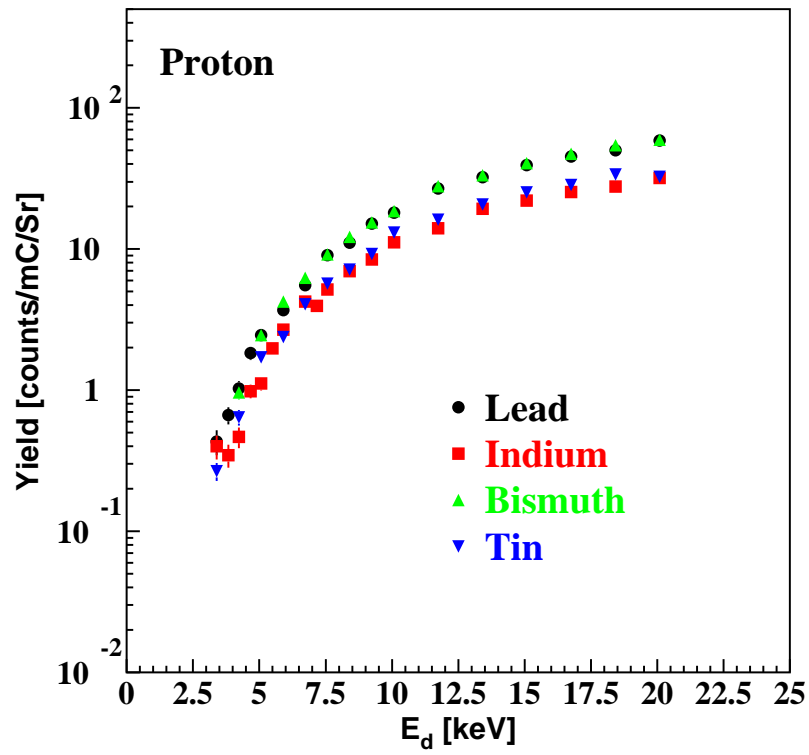


Figure 6.16: Excitation function of proton for every target.

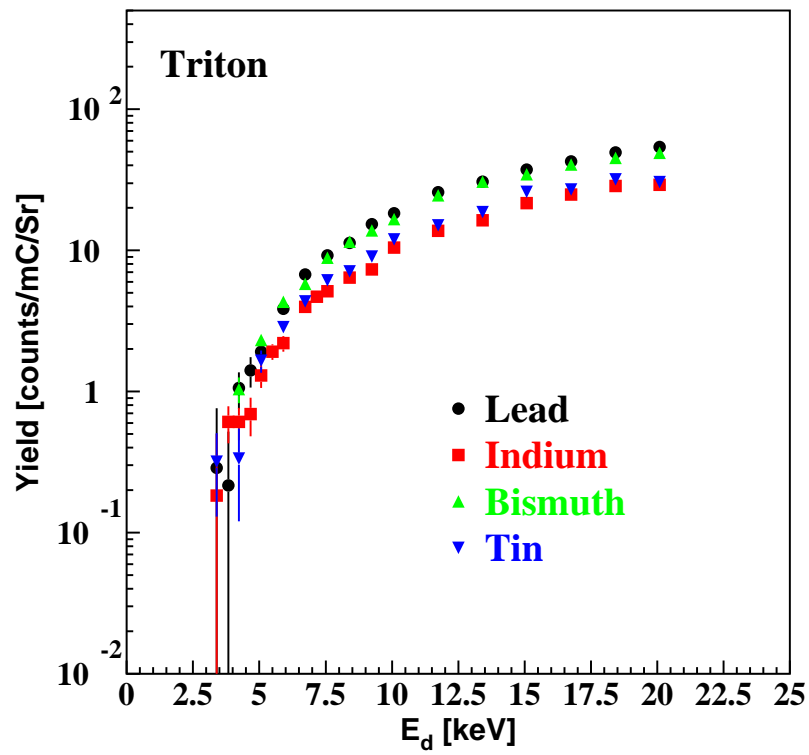


Figure 6.17: Excitation function of triton for every target.

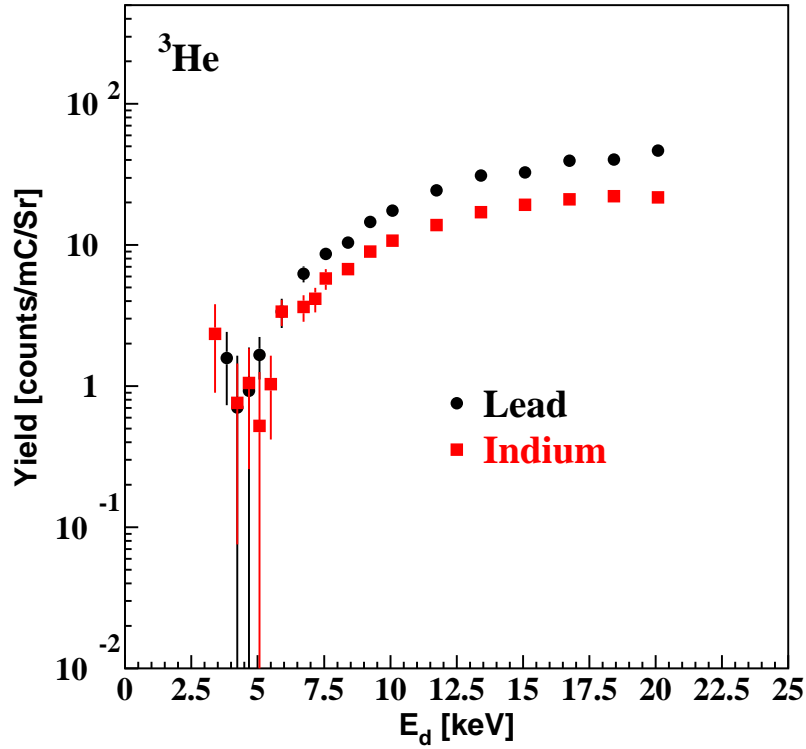


Figure 6.18: Excitation function of ^3He for every target.

measurement, T^F and T^B is the measurement time, and Q^B mC is the amount of the incident charge on the Faraday cup. $G(\epsilon)$ is a Gaussian distribution obtained from the fit performed in § 6.2.2 and is represented by the equation (6.2). The ϵ_{\min} and ϵ_{\max} are the upper and lower limit of the integration region. The Ω is the solid angle covered by the detectors.

The statistical errors for $N^{F/B}$ is given by

$$\Delta N^{F/B} = \sqrt{\omega^2 \sum_{\epsilon=\epsilon_{\min}}^{\epsilon_{\max}} f^{F/B}(\epsilon)}. \quad (6.7)$$

N^G is the partial integral value of the distribution obtained by fitting, and it cannot get error from a simple count number. Therefore, the value obtained by the following method was taken as a statistical error. We express the height, mean and standard deviation of the $G(\epsilon)$ in h , μ and σ , respectively, and these values has a fitting errors,

Δh , $\Delta\mu$ and $\Delta\sigma$. Let consider these values as variables, and modify the $G(\epsilon)$ as

$$G(\epsilon) \equiv g(\epsilon, h, \mu, \sigma) = h \exp\left(-\frac{(\epsilon - \mu)^2}{2\sigma^2}\right) \quad (6.8)$$

Moving the h , μ and σ within the its error, and the N_{\min}^G and N_{\max}^G which are minimum and maximum value of partial integration of $g(\epsilon, h, \mu, \sigma)$ from ϵ_{\min} to ϵ_{\max} are determined. Considering that ϵ_{\max} is always smaller than μ , N_{\min}^G and N_{\max}^G are represented as

$$N_{\min}^G = \int_{\epsilon_{\min}}^{\epsilon_{\max}} g(\epsilon, h - \Delta h, \mu + \Delta\mu, \sigma - \Delta\sigma) d\epsilon, \quad (6.9)$$

and

$$N_{\max}^G = \int_{\epsilon_{\min}}^{\epsilon_{\max}} g(\epsilon, h + \Delta h, \mu - \Delta\mu, \sigma + \Delta\sigma) d\epsilon. \quad (6.10)$$

The larger of difference between these values and N^G was taken as the error ΔN^G of N^G .

$$\Delta N^G = |N_{\min}^G - N^G| \quad \text{or} \quad \Delta N^G = |N_{\max}^G - N^G| \quad (6.11)$$

Chapter 7

Discussion

7.1 Results of experiment and calculation

7.1.1 Energy spectra

The energy spectra of proton and triton for In, Pb, Sn and Bi target are shown in Figures 7.1, 7.2, 7.3 and 7.4, respectively, for several incident energies indicated in each figure. The black and red line show the experimental and calculated spectra. The energy of the calculated spectrum is adjusted to the energy of the emitted particle minus the energy loss in the absorber; the absorber was assumed to be 5000 Å-thick carbon foil for proton and triton spectra. The calculated spectra are convoluted by Gaussian distribution with a standard deviation of 20 keV, which corresponds to the resolution of the detector, and a normalization is performed so that the yield of calculated and experimental spectra become the same.

The spectrum calculated by the CCM well represents the characteristics of the spectral shape of the experiment for all the targets. In detail, however, the experimental and calculated spectrum do not completely coincide with each other in a high incident energy region. Although, the experimental spectrum has sharp peak structure (in the case of proton, around 3 MeV), the calculation shows a flat structure (from 2.8 to 3.1 MeV for proton). It seems that the higher the energy, the worse the agreement between the calculation and the experiment. The events around the peak

energy $E_p \sim 3000$ keV corresponds to large-angle scattered deuterons; the scattering angles are greater than 100° . This suggests the possibility that the deuteron angular distribution of the scattering with metal atom is not correct. If the large-angle scattering cross section is larger, the calculation show the sharp peak structure. Or, if the small-angle scattering is suppressed, similar effects might be seen.

7.1.2 Yield

The yield of proton and triton are shown in Figure 7.5 and 7.6 as a function of the incident energy, E_d . The black circles show the experimental yield, and the red, green and blue curves show the calculated one with the Bohr, Moliere and ZBL screening model. As seen, the experimental absolute yield and excitation function for the proton and triton have good agreements with the calculated these with the Bohr model.

7.2 Screening potential

Since the $d + d$ reaction with CCM occur in the metal target, its reaction rate is affected by the screening effect. With the presence of the screening effect the cross section of the $d + d$ reaction, $\sigma_{\text{scr}}(E, U_s)$, is described by the following equation

$$\sigma_{\text{scr}}(E, U_s) = \sigma_{\text{bare}}(E + U_s) \quad (7.1)$$

$$\sim \frac{S(E)}{E} \exp\left(\frac{-31.397}{\sqrt{E + U_s}}\right) \quad (7.2)$$

Here, $\sigma_{\text{bare}}(E)$ is the cross section for bare nuclei, and U_s is the screening potential. The $d + d$ reaction yield with CCM, $Y^{\text{CCM}}(E, U_s)$, taking into account the screening effect can be calculated by converting the $d + d$ reaction cross section; $\sigma_{\text{bare}} \rightarrow \sigma_{\text{scr}}$. A suitable screening potential is obtain by the comparison between experimental yield $Y^{\text{exp}}(E)$ and $Y^{\text{CCM}}(E, U_s)$.

7.2.1 Interatomic potential dependence of screening potentials

In the previous section, the Bohr, Moliere and ZBL screening model were examined for the interatomic potential between a deuteron and a metal atom. Since the Coulomb scattering cross section varies depending on the interatomic potential, the calculated

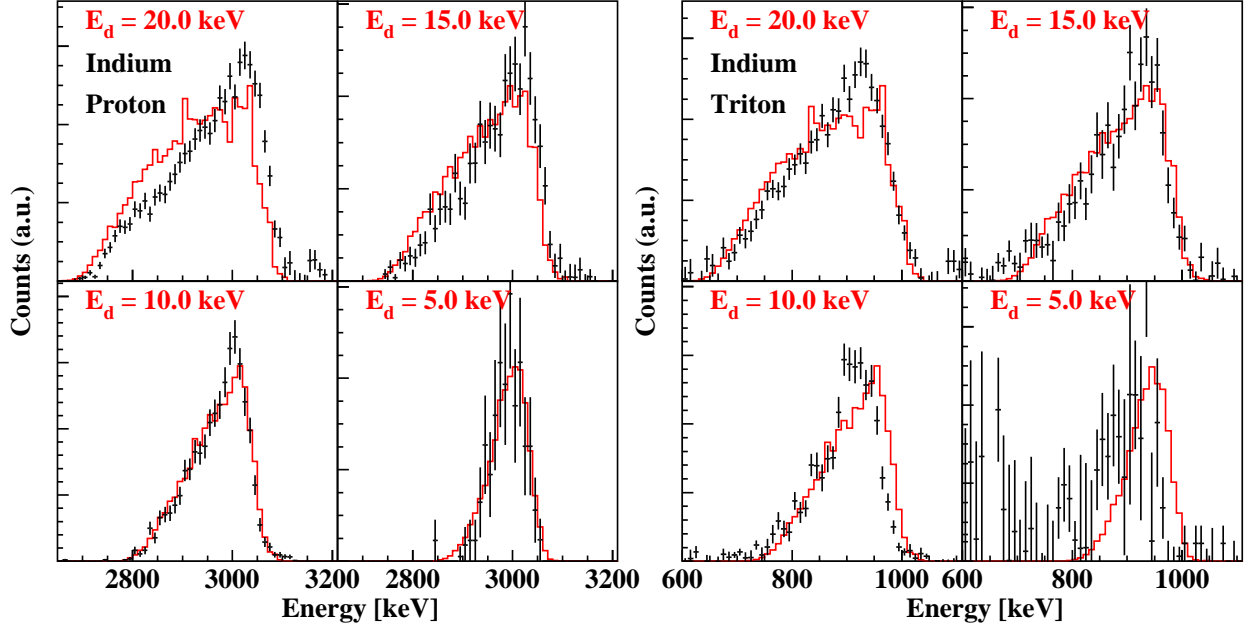


Figure 7.1: Energy spectra of proton and triton obtained from experiment and calculation for In target. The black and red line show the experimental and calculated one.

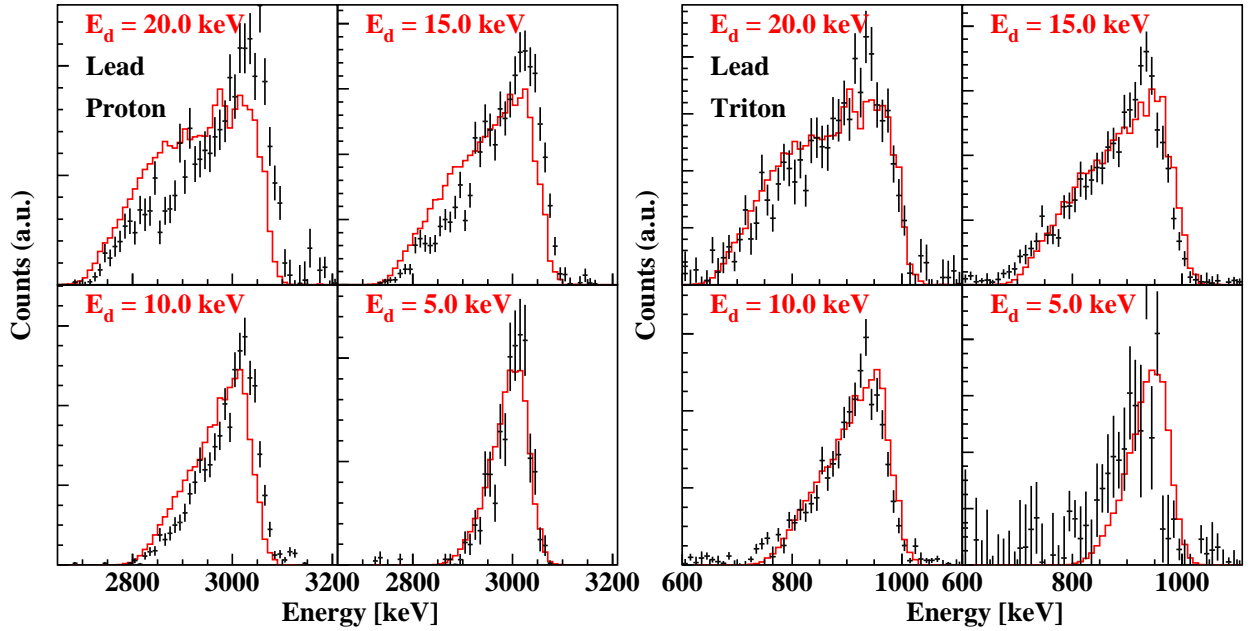


Figure 7.2: Energy spectra of proton and triton obtained from experiment and calculation for Pb target. The black and red line show the experimental and calculated one.

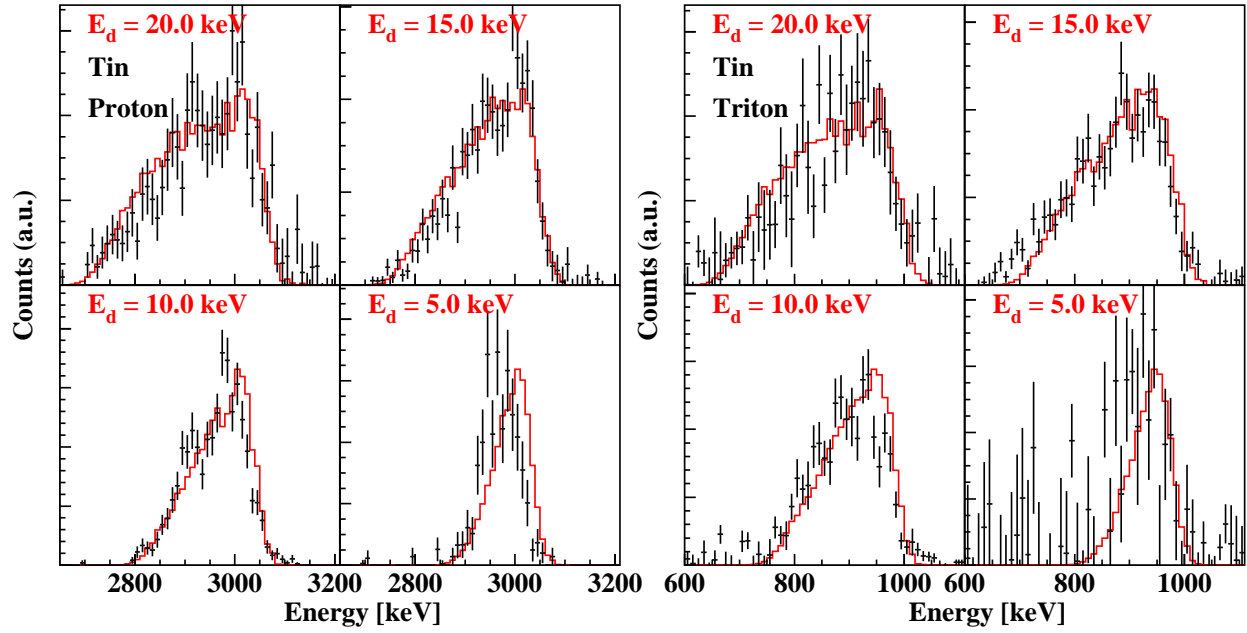


Figure 7.3: Energy spectra of proton and triton obtained from experiment and calculation for Sn target. The black and red line show the experimental and calculated one.

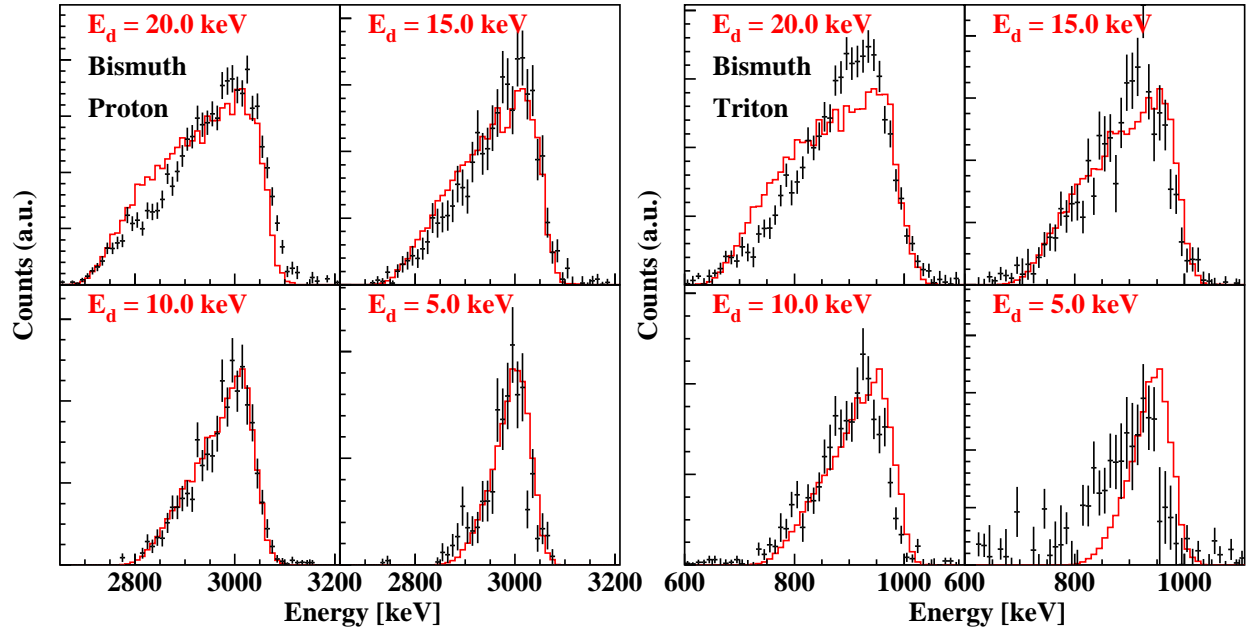


Figure 7.4: Energy spectra of proton and triton obtained from experiment and calculation for Bi target. The black and red line show the experimental and calculated one.

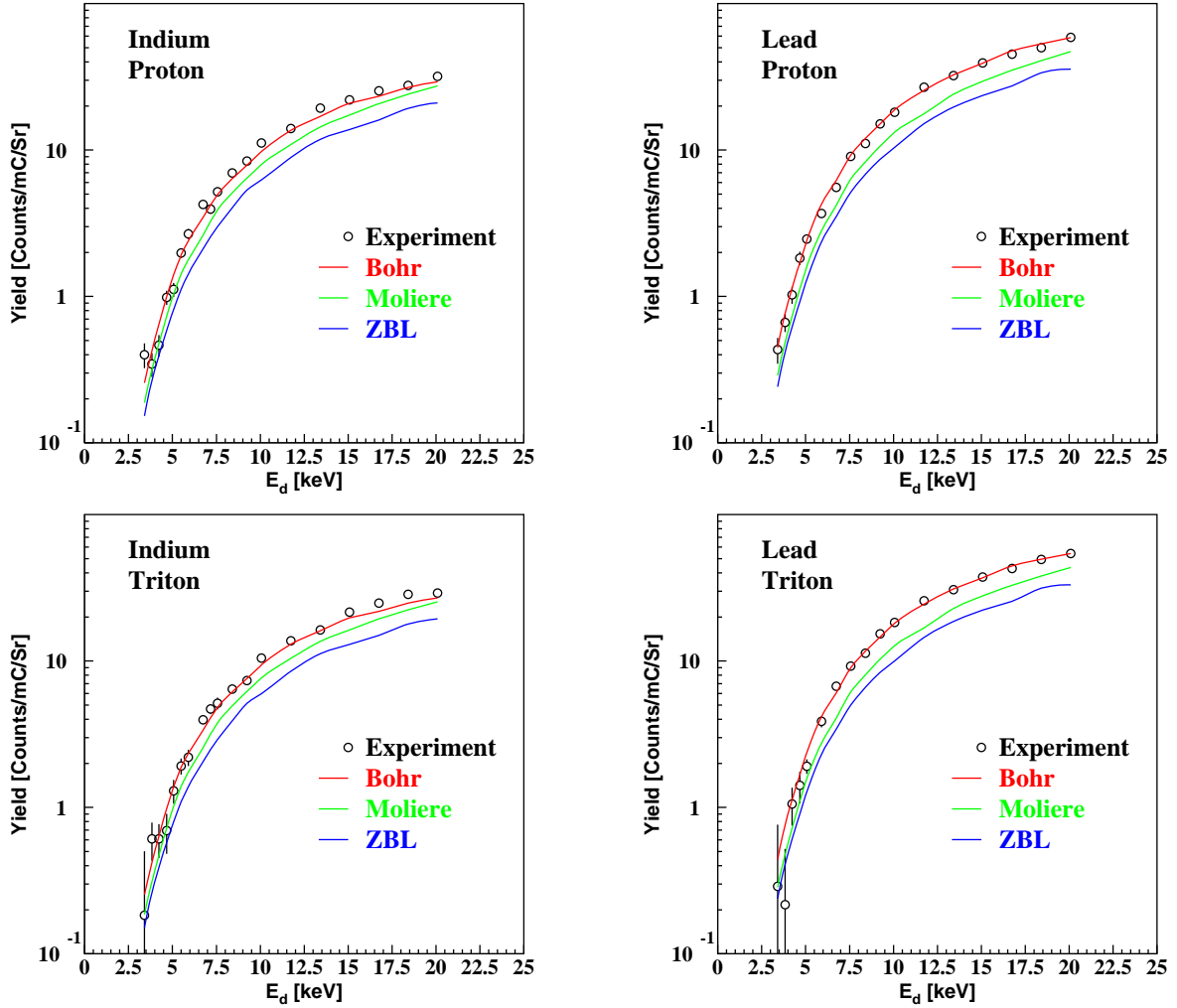


Figure 7.5: Experimental and calculated yield of proton(top) and triton(bottom) for the In(left) and Pb(right) target. The black points show the experimental yield, and the red, green and blue curves show the calculated one with the Bohr, Moliere and ZBL screening model.

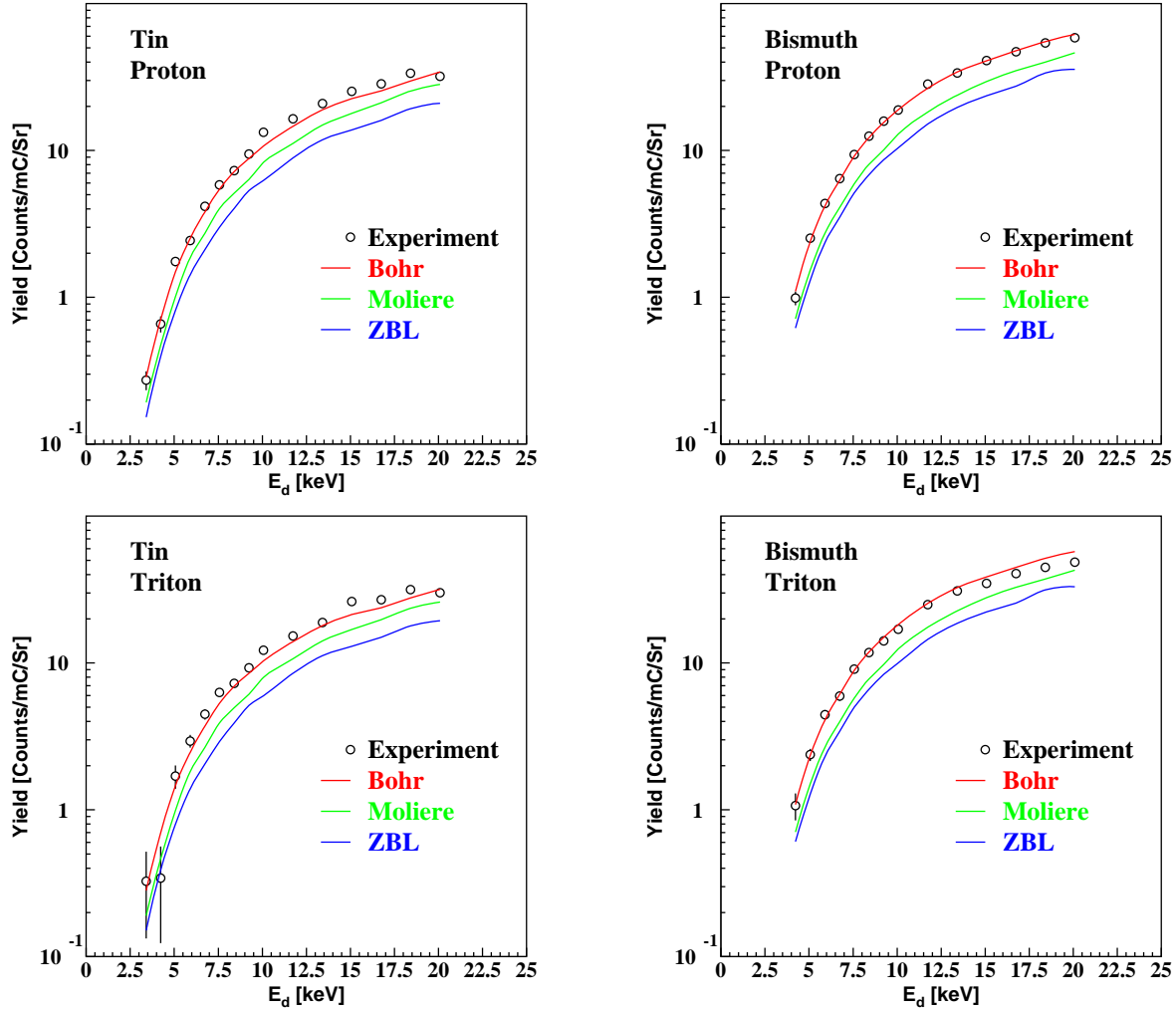


Figure 7.6: Experimental and calculated yield of proton(top) and triton(bottom) for the Sn(left) and Bi(right) target. The black points show the experimental yield, and the red, green and blue curves show the calculated one with the Bohr, Moliere and ZBL screening model.

yields also varies depending on the model. Therefore, a deduced value of the screening potential also depends on the model. As we saw, the Bohr model reproduce the data best, but we discuss the screening potential deduced by the Bohr and the Moliere model.

We compared the $Y^{\text{CCM}}(E, U_s)$ and $Y^{\text{exp}}(E)$, and find the suitable U_s which minimize the χ^2 described as,

$$\chi^2(U_s) = \sum_j^{p,t} \sum_i \left(\frac{Y_j^{\text{CCM}}(E_i, U_s) - Y_j^{\text{exp}}(E_i)}{\Delta Y_j^{\text{exp}}(E_i)} \right)^2. \quad (7.3)$$

Here, E_i is the incident energy, Y_p and Y_t are the yield of the proton and triton, and $\Delta Y_j^{\text{exp}}(E_i)$ is the statistical error of the $Y_j^{\text{exp}}(E_i)$. As the yield of p and t becomes exponentially small as plotted in Figure 7.5 and 7.6, it is rather difficult to show the differences in the form of the excitation function. Thus we define the enhancement factor ($EF^{\text{exp}}(E_d)$ and $EF^{\text{cal}}(E_d, U_s)$) as the ratio of measured yield to the calculated yield without the screening potential ($U_s=0$). They are

$$EF^{\text{exp}}(E_d) = \frac{Y^{\text{exp}}(E_d)}{Y^{\text{CCM}}(E_d, 0)} \quad (7.4)$$

and

$$EF^{\text{cal}}(E_d, U_s) = \frac{Y^{\text{CCM}}(E_d, U_s)}{Y^{\text{CCM}}(E_d, 0)}. \quad (7.5)$$

The $EF^{\text{exp}}(E_d)$ and $EF^{\text{cal}}(E_d, U_s)$ for In and Pb targets are shown in Figures 7.7 and 7.8, respectively. The left(right) column shows enhancement factors with the Bohr(Moliere) model, and the upper(lower) of the each panel shows that for proton(triton). The red points show the $EF_{\text{CCM}}^{\text{exp}}(E_d)$, and the black dash curves show the $EF_{\text{CCM}}^{\text{cal}}(E_d, U_s)$ with $U_s = 0, 200, 400, 600, 800, 1000$ eV from the bottom to top. The red curve shows the $EF_{\text{CCM}}^{\text{cal}}(E_d, U_s)$ with the suitable U_s ; the deduced U_s are 170 ± 30 and ≤ 10 eV for the In and Pb targets with the Bohr model, and $670 \pm 20, 850 \pm 20$ eV for the Moliere model, respectively. Since the absolute yield calculated with the ZBL model is about half of the experimental yield, the deduced U_s is anomalously large. Therefore we did not analyze the data by ZBL model.

Likewise, $EF^{\text{exp}}(E_d)$ and $EF^{\text{cal}}(E_d, U_s)$ for Sn and Bi targets are shown in the Figure 7.9 and 7.10, respectively. The deduced U_s are 250 ± 20 and ≤ 10 eV for

the Sn and Bi targets with the Bohr model, and 930 ± 20 , 990 ± 20 eV for the Moliere model, respectively. However, because the experiments with the Sn and Bi target have large systematic errors, the U_s are treated as the reference. The U_s and minimized χ^2 is summarized in Table 7.1.

As expected, the deduced screening potential strongly depends on the interatomic potential, V_{M-D} . As the calculated yield with the Moliere model is small, the U_s becomes large so as to compensate the small yield. As a result of the large U_s , the absolute value of the yield is reproduced, however, the χ^2 become large because the enhancement at the low-energy side cannot be seen in the experimental yield. On the other hand, since the calculated yield with the Bohr model is almost the same as experimental yield, the U_s becomes small. Hence, the enhancement at the low-energy side is small, and it makes the χ^2 small. From these facts, the best agreement between the experimental and calculated result are given with the Bohr model. Therefore, the calculation based on the Bohr model are used for future discussions.

However, as already seen in the spectrum analysis, the agreement with the calculation by the Bohr model is not perfect, and the χ^2/n is large. Since the enhancement due to the screening is small at the higher incident energy region, the yield and the spectrum in the region reflect the V_{M-D} accurately. The V_{M-D} which gives the more correct spectrum shape and yield in the region is required.

Table 7.1: Summary of deduced screening potentials.

Model	Target	U_s [eV]	χ^2/n
Bohr	In	170 ± 30	120.3/38
	Pb	≤ 10	58.4/34
	Sn	(250 ± 20)	131.9/30
	Bi	(≤ 10)	193.0/28
Moliere	In	670 ± 20	202.9/38
	Pb	850 ± 20	321.7/34
	Sn	(930 ± 20)	342.9/30
	Bi	(990 ± 20)	221.5/28

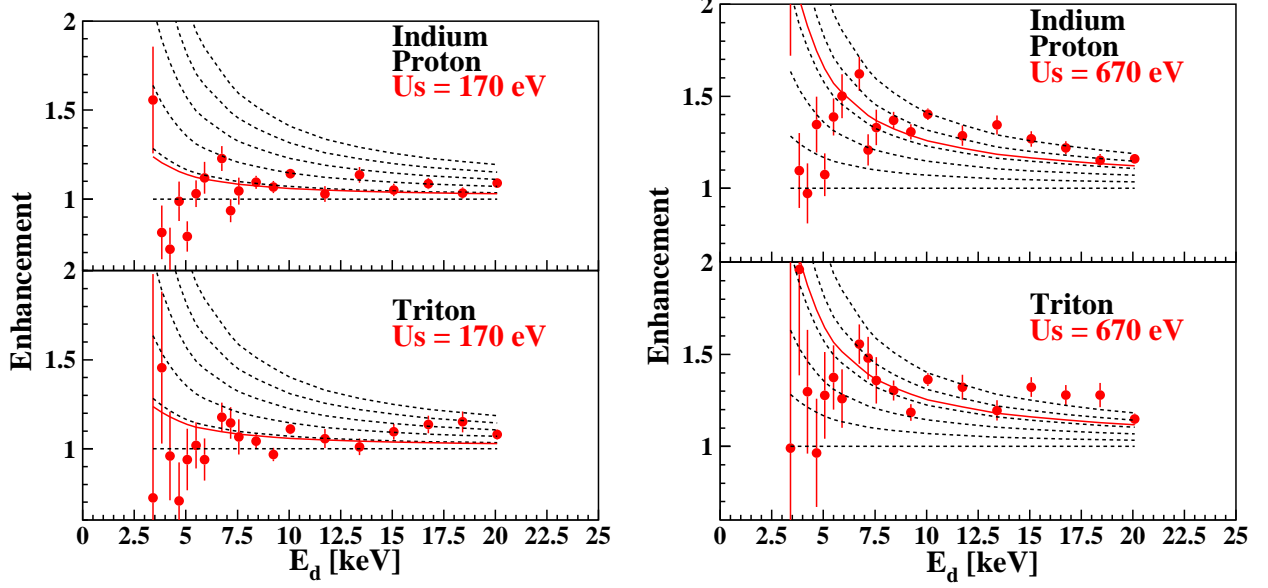


Figure 7.7: Enhancement factor of CCM with Bohr(left) and Moliere(right) model for In target. The red points show the experimental ones, and the black dash curves show the calculated ones with $U_s = 0, 200, 400, 600, 800, 1000$ eV from the bottom to top. The red curve shows the calculated enhancement factor with the suitable $U_s = 170$ and 670 eV for Bohr and Moliere model, respectively.

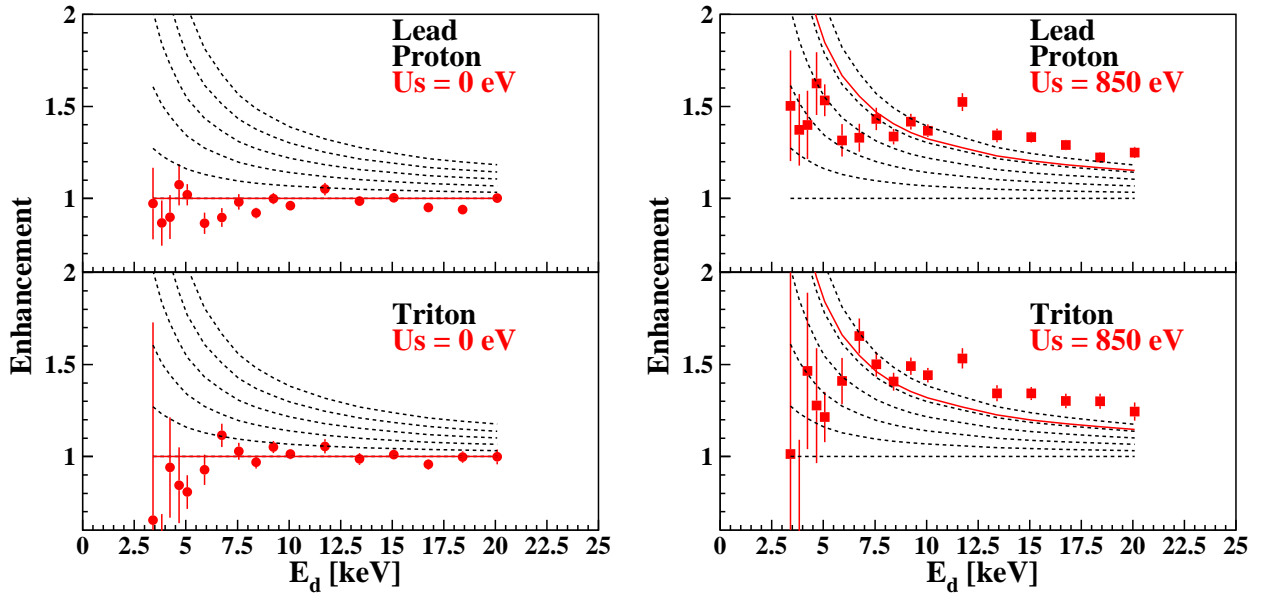


Figure 7.8: Enhancement factor of CCM with Bohr(left) and Moliere(right) model for Pb target. The red points show the experimental ones, and the black dash curves show the calculated ones with $U_s = 0, 200, 400, 600, 800, 1000$ eV from the bottom to top. The red curve shows the calculated enhancement factor with the suitable $U_s = 0$ and 850 eV for Bohr and Moliere model, respectively.

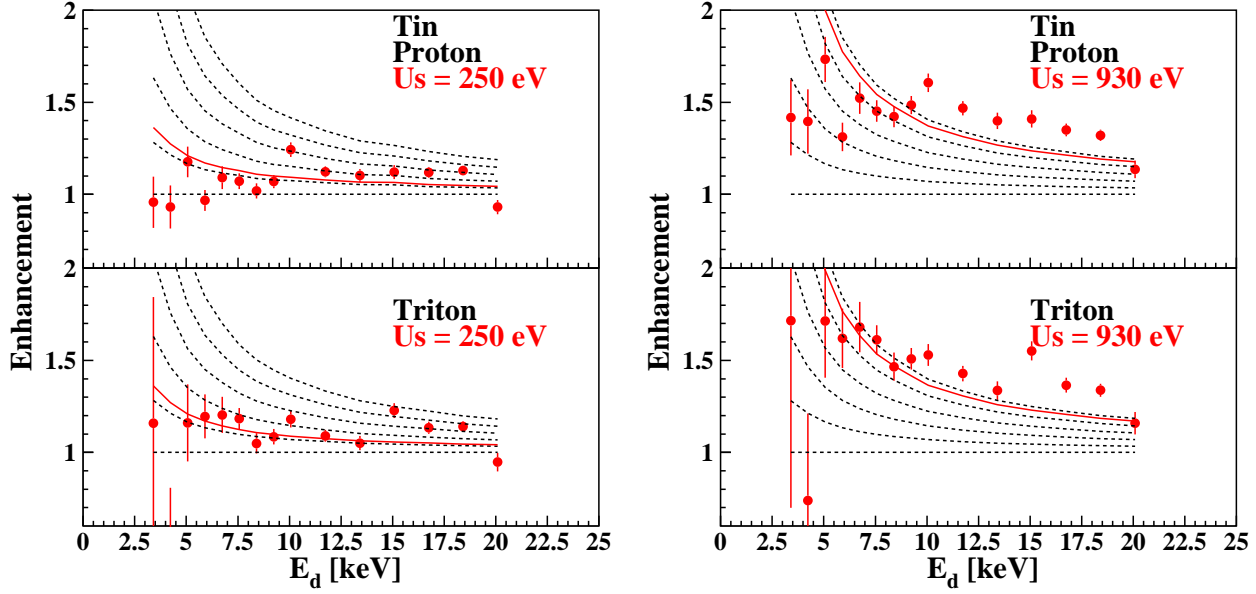


Figure 7.9: Enhancement factor of CCM with Bohr(left) and Moliere(right) model for Sn target . The red points show the experimental these, and the black dash curves show the calculated these with $U_s = 0, 200, 400, 600, 800, 1000$ eV from the bottom to top. The red curve shows the calculated enhancement factor with the suitable $U_s = 250$ and 930 eV for Bohr and Moliere model, respectively.

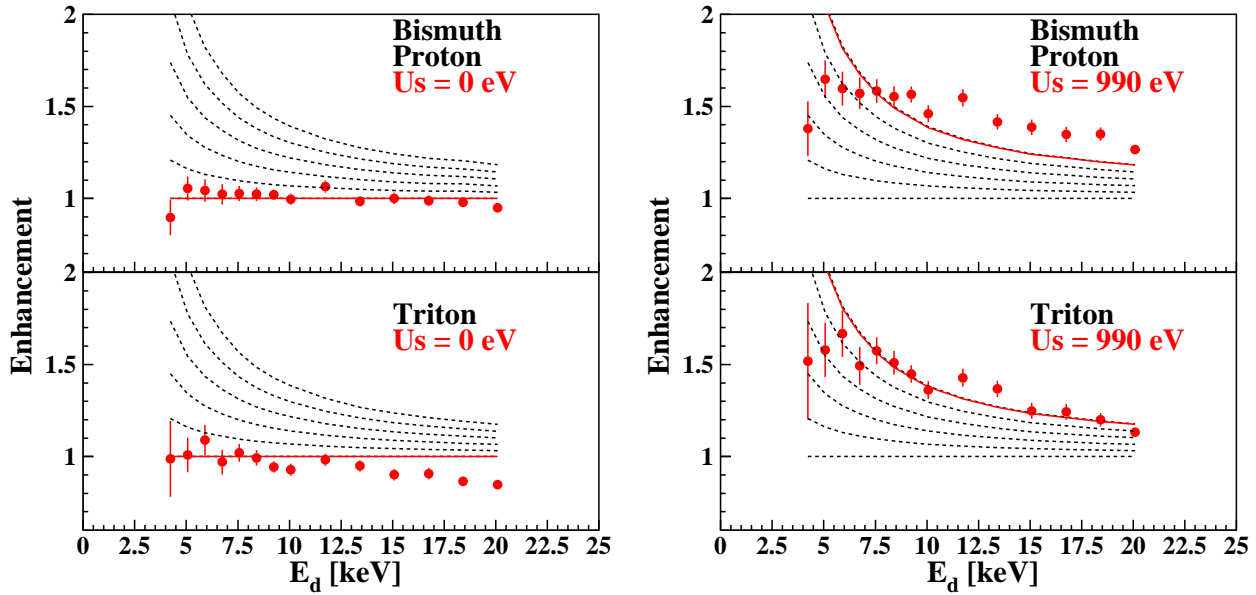


Figure 7.10: Enhancement factor of CCM with Bohr(left) and Moliere(right) model for Bi target . The red points show the experimental these, and the black dash curves show the calculated these with $U_s = 0, 200, 400, 600, 800, 1000$ eV from the bottom to top. The red curve shows the calculated enhancement factor with the suitable $U_s = 0$ and 990 eV for Bohr and Moliere model, respectively.

7.2.2 Systematic uncertainty

The systematic uncertainties are summarized in Table 7.2. The ΔU_s due to the solid angle comes from the ambiguity of the detector. The ambiguity is $\pm 2.6\%$ for the In and Pb target and $\pm 7\%$ for the Sn and Bi target. It causes the ΔU_s of the ± 70 , $+20$, ± 170 , $+120$ eV for the In, Pb, Sn and Bi target, respectively.

The ΔU_s due to the beam energy comes from its fluctuation. The fluctuation is ± 0.02 eV for the energy of the single deuteron. It causes the ΔU_s of the ± 10 , 0 , ± 10 , 0 eV, respectively.

The ΔU_s due to the r_{dd} comes from the accuracy of the interatomic distance of the deuterons in a molecule. In this work, $r_{dd} = 0.93 \pm 0.02$ Å is adopted for the D_3^+ molecule, the value is reported by Miao *et al.* [41]. In order to estimate the r_{dd} dependence of the CCM yield, Y^{CCM} , we calculated the Y^{CCM} with various r_{dd} ; the result is shown in Figure 7.11. In the calculation, the incident energy is fixed to 20 keV, and the target is In. The open circles show the calculated Y^{CCM} , and red curve shows the result of the fitting as

$$Y^{\text{CCM}} \propto r_{dd}^{-1.57}. \quad (7.6)$$

With the dependence of Equation (7.6), the Y^{CCM} fluctuates $\pm 3.4\%$ by change of one standard deviation of the r_{dd} . The fluctuation causes the uncertainty for screening potential of ± 80 , $+40$, ± 80 and 0 eV for In, Pb, Sn and Bi target, respectively.

Table 7.2: Summary of the systematic errors.

Metal	Solid angle	ΔU_s [eV]	
		beam energy	r_{dd}
In	± 70	± 10	± 80
Pb	$+ 20$	0	$+ 40$
Sn	± 170	± 10	± 80
Bi	$+ 120$	0	0

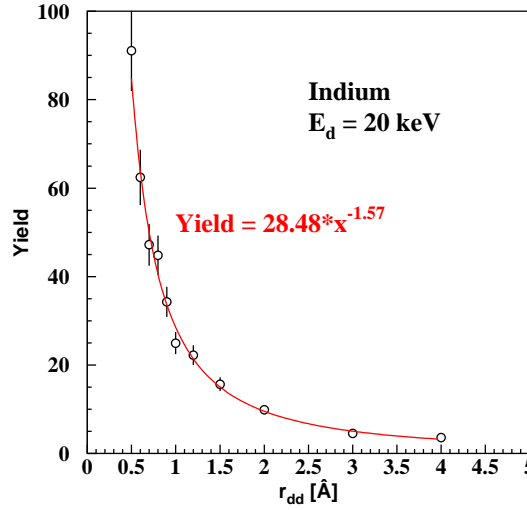


Figure 7.11: Calculated yield of the CCM as a function of the r_{dd} . The target is the In, and the incident energy is fixed to 20 keV. The open circles show the calculated yields, and red curve shows the result of the fitting as described in the figure.

7.2.3 Screening effect for the CCM

Consider what kind of the screening effect contributes to the $d+d$ reaction through the CCM. A screening effect originates from a change of charge distribution of electrons and ions around the colliding nuclei. Thus, when the reacting nuclei move faster than these, a screening effect becomes small because there is not enough time to change the charge distribution [42]. For the $d+d$ reaction through the CCM, in this work, deuteron has a kinetic energy of 20 keV maximum and its velocity is $v_d/c = \beta_d = 4.5 \times 10^{-3}$. On the other hand, Fermi velocities of the conduction electrons of In, Pb, Sn and Bi are $v_F/c = \beta_F = 5.7 \times 10^{-3}$, 5.9×10^{-3} , 6.2×10^{-3} and 6.3×10^{-3} , respectively. Since the β_F faster than the β_d , the conduction electrons can contribute to the screening effect. By means of the Thomas-Fermi screening model, the screening potential U_s^{TF} originates from the conduction electrons is calculated as

follow.

$$\text{In} : U_s^{\text{TF}} = 27.3 \text{ eV} \quad (7.7)$$

$$\text{Pb} : U_s^{\text{TF}} = 27.8 \text{ eV} \quad (7.8)$$

$$\text{Sn} : U_s^{\text{TF}} = 28.4 \text{ eV} \quad (7.9)$$

$$\text{Bi} : U_s^{\text{TF}} = 28.5 \text{ eV} \quad (7.10)$$

Similarly consider the velocity of the metal ion. Since the metal is liquefied, the metal ion can move and may contribute to the screening effect. As the thermal energy of ions is larger than the Fermi energy of ones, its momentum distribution is determined by temperature. The thermal energy of the metal ion is approximately only 30 meV, and the velocity is lower than the incident deuteron, obviously. Therefore, the metal ions cannot contribute to the screening effect. If the ions can contribute, the screening potential is calculated by means of the Debye screening model, and the value is $U_c^D = 290, 285, 310$ and 320 eV for In, Pb, Sn and Bi, respectively, with the temperature of the present work.

Consider the screening potential, U_s^B , due to the polarization of bound electrons of the metal atoms; it is argued by Czerski *et al* [43]. According to Bohr's model, the velocity of the bound electron β_B is calculated by

$$\beta_B = \frac{Ze^2}{4\pi\epsilon_0\hbar n} \sim 7.3 \times 10^{-3} \times \frac{Z}{n}. \quad (7.11)$$

Here, Z is an atomic number of the metal, and n is the principal quantum number of the bound electron. Substituting 5 and 6 for n , which values correspond to the principal quantum number of the peripheral electron of In and Pb, the β_B become 7.2×10^{-2} for In and 1.0×10^{-1} for Pb, respectively. Since β_B of used metal are faster than its β_d , the bound electrons can contribute to the screening effect. The screening potential U_s^{pol} , which is a sum of the U_s^{TF} and U_s^B , is calculated as approximately 60 eV for used metals [44].

A cohesion screening is considered by Czerski *et al*. The value of the screening potential U_s^{coh} is described as

$$U_s^{\text{coh}}(r) = 2 V_{\text{M-D}}(r) - V_{\text{M-He}}(r), \quad (7.12)$$

where the V_{M-He} is an interatomic potential between metal atom and helium. Since we adopted the Bohr screening model which serves strong reduction in interatomic potential, the U_s^{coh} become very small; less than 1 eV.

From the above discussion, the conduction and bound electrons are considered to contribute to the screening effect, and the value of the screening potential U_s^{theo} is 60 eV for each metal.

7.2.4 Discussion about screening potential

The experimental and theoretical screening potential, U_s and U_s^{theo} , and experimental uncertainties are summarized in Table 7.3. The ΔU_s^{stat} is the statistical uncertainty, the ΔU_s^{sys} is the systematic one and the U_s^{solid} is the screening potential measured with solid metal target.

Table 7.3: Summary of deduced screening potentials and errors in a unit of eV

Metal	U_s	ΔU_s^{stat}	ΔU_s^{sys}	U_s^{theo}	U_s^{solid}
In	170	± 30	± 110	60	520 ± 50 [10]
Pb	≤ 10	-	$+ 60$	60	480 ± 50 [10], 440 ± 50 [13]
Sn	250	± 20	± 190	60	130 ± 20 [10], 200 ± 20 [45]
Bi	≤ 10	-	$+ 120$	60	540 ± 60 [10]

In this work, we obtained that the screening potentials for the In, Sn, Pb and Bi are 170 ± 30 , ≤ 10 , 250 ± 20 , ≤ 10 eV, respectively. In comparison with U_s^{theo} , because of its large systematic uncertainty, the U_s and U_s^{theo} have an agreement within a standard deviation for all target. Therefore our results may be explained by only electron screening without other enhancement effects. In comparison with U_s^{solid} , for the Sn target, our value agrees with the one reported by Raiola *et al.*, 130 ± 20 [10] and 200 ± 20 eV [45]. However, for the In, Pb and Bi targets, the reported screening potentials are nearly 500 eV, they do not coincide with our results at all. Our results are greatly smaller than these. Since the D_3^+ beam was used for the solid metal experiments, the possibility of an enhancement due to the CCM is considered in § 7.3.

7.3 Contribution of CCM to solid metal experiment

A molecular beam is used for the previous solid metal experiments conducted by the Bochum and Berlin group [11, 46]. However, the CCM is not taken into account for their analysis. As compared with the yield of the normal $d + d$ reaction, the yield of the CCM decreases more slowly as the incident energy decreases. Thus, when the molecular beam is used, the yields at the low-incident energy are enhanced by the CCM. The enhancement may be incorrectly recognized as the enhancement due to the electron screening effect. In this section, we perform a simple simulation. The $d + d$ reaction yields for the solid metal target with the D_3^+ beam bombardment are calculated, and its enhancement effect is deduced.

Figure 7.12 shows a simulation of the yield. When the solid In target is bombarded by a D^+ beam, there is no contribution from the CCM, and a reaction yield is represented by a normal $d + d$ reaction, correctly. The yield of the normal $d + d$ reaction is proportional to the deuteron density; the calculated yields without the screening potential are drawn in the figure by the solid and dashed black curves with the deuteron density of 1.0×10^{22} (ρ_1) and 0.1×10^{22} cm^{-3} (ρ_2), respectively. When the solid In target is bombarded by a D_3^+ beam, an additional contribution from the CCM exists. The contributions obtained from the experiment and the calculation are drawn in the figure by blue points and a solid curve, respectively. As a result, experimental yield obtained from the D_3^+ beam bombardment to the solid In target becomes a sum of the normal $d + d$ reaction yield and the contribution from the CCM. The sum is drawn by solid (dashed) red line in the figure. Since the yield of the CCM independent on the deuteron density, the influence from the CCM becomes larger as the deuteron density decreases.

For the solid metal experiments, an enhancement factor is usually obtained from the ratio of the measured yield to the calculated normal $d + d$ reaction yield without the screening potential. It corresponds to the ratio of red and black solid (dashed) line in the Figure 7.12. The enhancement factor with the ρ_1 and ρ_2 are described in the Figure 7.13 by the black and red points, respectively. The black and red solid lines show the fitting result with the free parameter of the screening potential and the normalize factor. The deduced screening potentials, we call it U_s^{Dummy} , are 126 eV for the ρ_1 and 496 eV for the ρ_2 . It is found that when the D_3^+ beam is used, a screening potential of few 100 eV can be misidentified even if there is no screening effect. For the

solid In target experiment by Bochum group, which reported the screening potential of 500 eV, the deuteron density is deduced to be $\rho \sim 0.1 \times 10^{22} \text{ cm}^{-3}$. Thus, there is a probability that all of the enhancement came from the CCM.

The U_s^{Dummy} for the In and Pb target are calculated as a function of the (ρ_d/Z) , and drawn in Figure 7.14 with black and red curve, respectively. Since the yield of the CCM nearly proportions to the Z , the U_s^{Dummy} for the In and Pb become almost the same in the axis of (ρ_d/Z) . As is obvious, the U_s^{Dummy} increases as the (ρ_d/Z) decreases. When the (ρ_d/Z) is less than 10^{22} cm^{-3} , the U_s^{Dummy} becomes enough small. The screening potentials reported by Bochum group are also shown in Figure 7.14 with black, red and green points [10, 13, 46]. The Bochum group used D_3^+ beam in the range of $2.10 \leq E_d \leq 3.75 \text{ keV}$ [46]. The (ρ_d/Z) of the Bochum group measurements are concentrated near the $1-4 \times 10^{20}$, where U_s^{Dummy} is about 100–250 eV. The reported screening potentials in that region concentrate about 200–500 eV, and about half values of it can be explained by U_s^{Dummy} . The U_s^{Dummy} is calculated using the our experimental yield of the CCM with the incident energy of 3.3 - 20 keV. However, the minimum incident energy of the Bochum group is 2.10 keV, where the larger enhancement due to the CCM should appear. It should increases the U_s^{Dummy} . Thus, it may be possible to explain larger screening potentials by the U_s^{Dummy} .

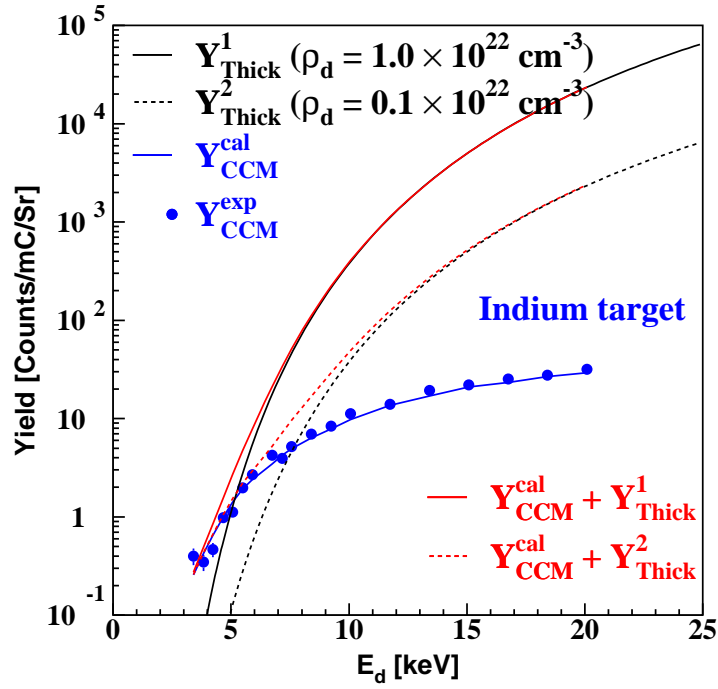


Figure 7.12: Yield simulation of solid metal target experiment using D_3^+ beam.

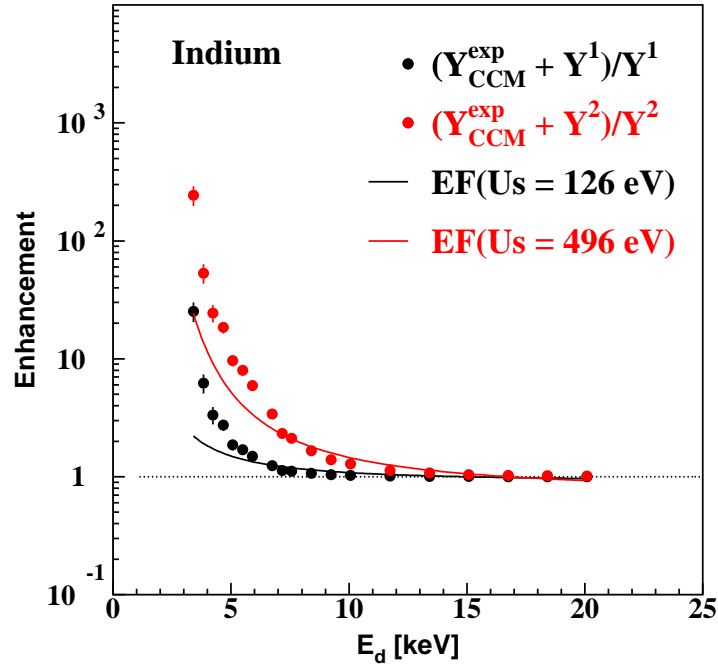


Figure 7.13: Simulated enhancement factor of solid metal target experiment using D_3^+ beam.

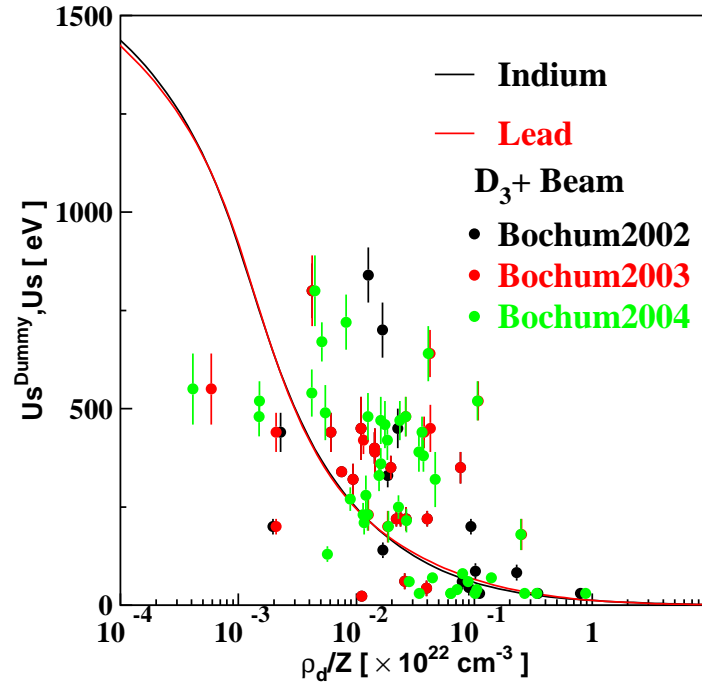


Figure 7.14: The calculated U_s^{Dummy} for the In and Pb target and reported U_s as a function of the (ρ_d/Z) .

Chapter 8

Conclusions

In order to clarify the enhancement due to the screening effect for the nuclear reaction in dense plasma, a measurement of the screening potential with the CCM was developed. To deepen the understanding of the CCM, an accumulation of the experimental data and a development of the simulation were conducted.

We bombarded metal targets, In, Pb, Sn and Bi by a D_3^+ beam, and measured the $d + d$ reaction which occurred through the CCM. The emissions of the proton, triton and ^3He were clearly observed with both the liquid and solid metal target, but the energy spectra for the both target were significantly different. That is because, the dominant reaction is different due to the deuteron density in the target. For the liquid metal target, the $d + d$ reaction through the CCM becomes the dominant since the deuteron density is very low ($\rho_d \sim 10^{17} \text{ cm}^{-3}$). A wide and asymmetry energy spectrum was observed which is peculiar to the CCM. The line shapes of the energy spectra measured with the same incident energy are almost the same for the all liquid target. The yields for the Pb and Bi target were higher than ones for the In and Sn target, and the yield ratio corresponds to approximately 1.7.

A simulation of the spectrum and the reaction yield of the $d + d$ reaction through the CCM is developed. A relative momentum distribution of the deuterons at the collision was obtained by mean of the trajectory calculation of the deuteron in the metal with a Monte Carlo method. Three screening models, Bohr, Moliere and ZBL, were adopted to examine an interatomic potential of a deuteron and a metal atom. The

shape of the calculated energy spectrum with the same incident energy is almost the same for all models. However, the reaction yield strongly depends on the interatomic potential. The ratio of the calculated yield with each model is about Bohr : Moliere : ZBL = 1 : 0.9 : 0.6. The ratio corresponds to the ratio of the cross section of the large-angle scattering calculated from the models. It indicates that the yield of the CCM at the higher energy is dominated by the large-angle scattering cross section.

As a result of the comparison between the experimental result and the calculation, our calculation quantitatively represented the experimental yield and energy spectra. A screening potential, U_s , was deduced. Since the calculated yield depends on the model, the value of U_s also has a model dependence. A minimum χ^2 was obtained for the calculation with the Bohr model. The systematic uncertainties from the ambiguity of the solid angle, the fluctuation of the beam energy and the accuracy of the r_{dd} were considered, and deduced values of U_s were $170_{-30}^{+30+110}$, 0_{-0}^{+10+60} , $250_{-20}^{+20+190}$, $0_{-0}^{+10+120}$ for the In, Pb, Sn and Bi target, respectively. For the Sn target, our value agrees with the ones reported by Raiola *et al.*, 130 ± 20 [10] and 200 ± 20 eV [45]. On the other hands, for the In, Pb and Bi target, the reported screening potentials for these are nearly 500 eV, they do not coincide with our results at all. In comparison with the theoretical screening potentials of $U_s^{\text{theo}} = 60$ eV, U_s and U_s^{theo} have a agreement within a standard deviation for all target because of the large systematic uncertainty of the experimental data. Therefore our results may be explained by only electron screening without other enhancement effects.

It became clear that the $d + d$ reaction through the CCM affects the value of the screening potential measured so far with the deuteron molecular beam. Since the misinterpretation of the screening potential of several hundred eV is caused, the CCM must be considered for a determination of the screening potential. With the D_3^+ beam, when the ρ_d/Z is 10^{20} cm^{-3} , a screening potential of 200 eV may be misidentified. The enhancement due to the CCM decreases as the ρ_d/Z increases, and almost diminished at about $\rho_d/Z \sim 10^{22} \text{ cm}^{-3}$.

8.1 Future issue

Throughout the present study, I have been convinced that nuclear reaction in liquid targets will greatly contribute to the development of both atomic and nuclear physics.

It is highly desirable to acquire systematic data of the CCM $d + d$ reaction from experiments that can be carried out immediately.

Examples are those: Measurement with Ga ($Z=31$) and K ($Z=19$) will bring new information about Z dependence of the potential. Both metals can be liquefied easily.

Measurement with non-metal materials are also interesting. We might know the effect of the conduction electrons on the CCM reaction. Candidate for such experiments are Se ($Z=34$) and S ($Z=16$), both of which can be liquefied easily again.

Acknowledgments

The work underlying this thesis has been conducted in the Research Center for Electron Photon Science (ELPH), Tohoku University, Japan. I could never complete this thesis without helps, supports and encouragements of many people.

I am deeply grateful to my supervisor Prof. Hajime Shimizu for his constant encouragement and taking care of me for seven years throughout my student days.

I would like to express the deepest appreciation to Prof. em. Jirohta Kasagi for introducing me to this field, low energy nuclear physics. Without his guidance and persistent help this thesis would not have been possible.

I would particularly like to thank Prof. Toshimi Suda, Assoc. Prof. Kouich Hagino, Assoc. Prof. Masatoshi Itoh, and Assoc. Prof. Kimiko Sekiguchi for being my thesis committee and giving many constructive suggestions. Prof. Toshimi Suda read my thesis and gave me many incisive comments.

I am indebted to Assoc. Prof. Norihito Muramatsu, Dr. Takatsugu Ishikawa, Dr. Manabu Miyabe, and Dr. Atsushi O. Tokiyasu for practical advices of experiments and analyses.

I am grateful to Mr. Kazue Matsuda and technical staffs of ELPH for building experimental equipment and guidance of the operation of machine tools.

I would like to offer my special thanks to Dr. Yusuke Tsuchikawa, Mr. Akihiko Nakamura, Mr. Yusuke Taniguchi, Mr. Ryuji Yamazaki, Mr. Tatsuya Amagai, and Mr. Takaya Miyamoto for their supports and friendships.

My special thanks go to all the early contributors for the low energy nuclear experiments at ELPH. I could not complete this work without their developments of experimental equipment and accumulations of the experiments

Finally, I would like to thank my parents for their supports and encouragements.

Appendix A

Calibration of the emissivity

A.1 Calibration of the thermal emissivity

The temperature of the target is measured by a infrared radiation thermometer (IRT). In order to determine a temperature, IRT needs the emissivity of the target. In general, it is difficult to use the literature values of the emissivity because they are affected by various factors, such as surface roughness and cleanness. In order to obtain the emissivity, we used a inflection of the temperature change at the melting point. Figure A.1 shows the measured temperature of In by IRT as a function of the time. At the time is zero, we stopped heating of the In, and the temperature decreases monotonically until it reaches to the melting point. At the melting point, the heat of solidification makes the temperature decreasing slowly. A discontinuity change of the emissivity originated from a phase change may also distort the temperature curve. As a result, an inflection point appears. After the solidification, we started heating again. An inflection point which is a result of the liquefaction appears. Since the different phase has a different emissivity even if the material is the same, the temperature of these inflection points are slightly different. We calculated the emissivity which represents that the measured temperature at the solidification points corresponds to the melting temperature.

The spectral density of the radiation emitted by a black body, $I^b(\lambda, T)$, is described

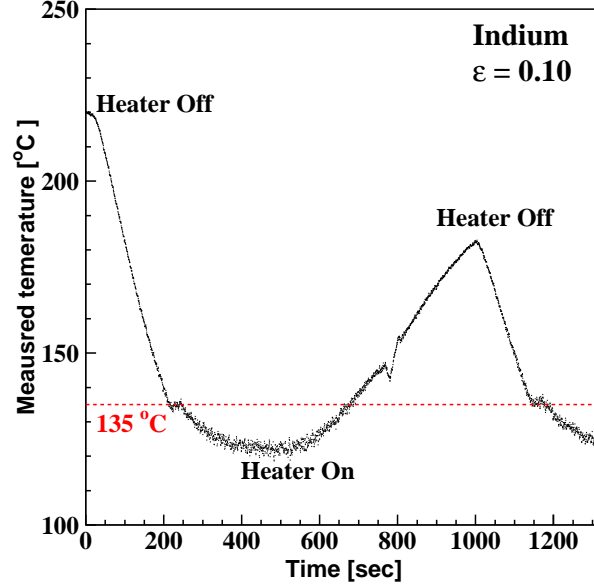


Figure A.1: Time dependence of the temperature of indium.

by Planck's law of radiation,

$$I^b(\lambda, T) = \frac{2hc^2}{\lambda^5} \frac{1}{\exp(hc/\lambda kT) - 1}, \quad (\text{A.1})$$

$$\sim \frac{2hc^2}{\lambda^5} \exp(-hc/\lambda kT) \quad \left(\frac{hc}{\lambda} \gg kT \right). \quad (\text{A.2})$$

Here, λ, T, h, c, k are wavelength of the radiation, temperature of a black body, Planck constant, speed of light and Boltzmann constant. In the present measurement, the radiation energy (hc/λ) and thermal energy (kT) are approximately 440–620 meV ($\lambda = 2.0\text{--}2.8 \mu\text{m}$) and 40–60 meV ($T \sim 500\text{--}730\text{K}$), respectively. Since the radiation energy is greatly larger than the thermal energy, the Planck's law is approximated by the Wein's radiation law, Equation (A.2). The spectral emissivity in wavelength, ϵ_λ , is defined as the ratio of $I^b(\lambda, T)$ and a measured spectral density, $I(\lambda, T)$.

$$\epsilon_{\lambda, T} \equiv \frac{I(\lambda, T)}{I^b(\lambda, T)} \quad (\text{A.3})$$

In the experiment, the measured value is a part of a radiation energy, $E^{abs}(T)$, which is proportional to a integral of the spectral density. The emissivity, ϵ_T , is defined by following equation,

$$\epsilon_T \equiv \frac{\int \epsilon_{\lambda,T} I^b(\lambda, T) d\lambda}{\int I^b(\lambda, T) d\lambda} = \frac{E^{abs}(T)}{\int I^b(\lambda, T) d\lambda}. \quad (A.4)$$

A relationship among the absorbed energy, emissivity and spectral densities is described in Equation (A.5). Here, $\epsilon_T^1, \epsilon_T^2, T^1$ and T^2 are correct/incorrect emissivity and temperature of the object measured with $\epsilon_T^1/\epsilon_T^2$, respectively. The ϵ_T^1 is calculated by equation (A.6).

$$E^{abs} = \epsilon_T^1 \int I^b(\lambda, T^1) d\lambda = \epsilon_T^2 \int I^b(\lambda, T^2) d\lambda \quad (A.5)$$

$$\epsilon_T^1 = \epsilon_T^2 \frac{\int I^b(\lambda, T^2) d\lambda}{\int I^b(\lambda, T^1) d\lambda} \quad (A.6)$$

We substituted the temperatures of the melting point and measured inflection point for the equation (A.6), and calculated the correct emissivities. They are summarized in TableA.1. Since the emissivities for In and Sn are lower than 0.1 which is the minimum set value of used IRT, the emissivity is set to 0.1, and correction with the calculated emissivity is performed after the measurement.

Let me confirm the validity of the calculation. Figure A.2 shows the temperature of the indium with various heating power as a function of the emissivity. The black points shows the measured temperature by IRT, and the red curves shows the result of calculation which take a true temperature as a fit parameter. The calculation results very well agree with the measurement. It was confirmed that emissivity dependency was expressed correctly.

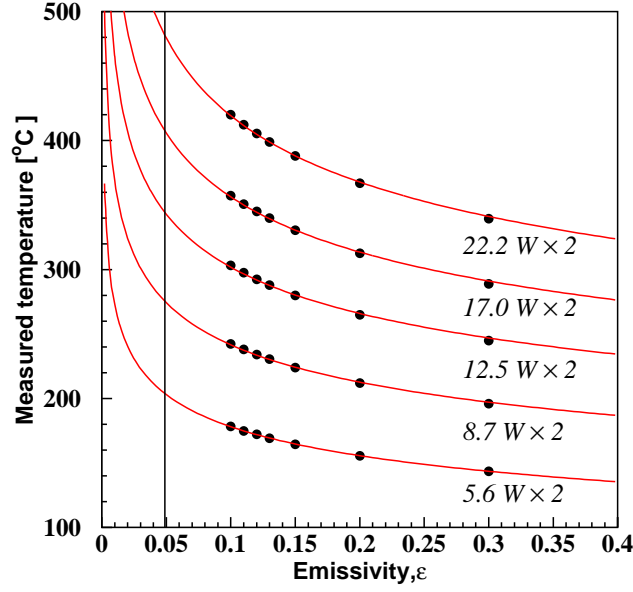


Figure A.2: Emissivity dependence of the measured indium temperature for various heating.

Table A.1: Temperature and thermal emissivity of the target

Metal	Heater [W]	ϵ^2	T^2 [°C]	ϵ^1	T^1 [°C]	ρ
In	2×12.5	0.10	235 – 285	0.054	264 – 320	6.95 – 6.91
Pb	2×42.0	0.10	400 – 430	0.134	378 – 406	10.61 – 10.57
Sn	2×17.0	0.10	360 – 400	0.035	438 – 489	6.89 – 6.86
Bi	2×17.0	0.10	330 – 370	0.119	320 – 358	9.96 – 9.92

Appendix B

Rest deuteron in the liquid metal

B.1 Rest target background

The yields of the rest target background are proportional to the deuteron density in the target metal. If the surface of the liquid target is clean, the accumulated deuteron density is very low and cannot be seen on the energy spectrum. For that reason the deuteron density was estimated after each measurement from the $d + d$ reaction yield of D^+ beam bombardment at 60 keV. The energy spectra for the Pb target is shown in Figure B.1. Since the reaction yield is very small, the spectrum is the sum of all 60-keV D^+ measurements.

Figure B.2 shows the yield, Y_{exp} , in the range of 2700–3000 keV for each run. It can be seen that $Y_{\text{exp}} \leq 2$ for most of the runs. We deduced the deuteron density from Y_{exp} and estimated the influence on the D_3^+ beam experiment.

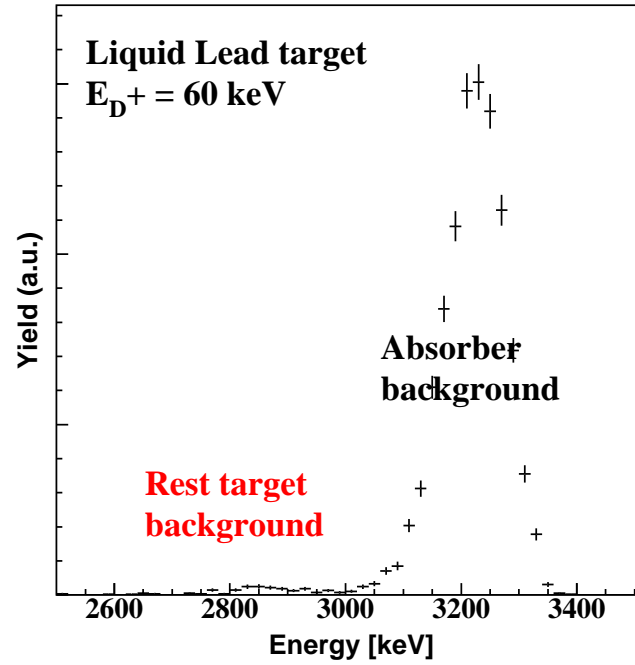


Figure B.1: Energy spectra of proton with the 60 keV D^+ beam bombardment.

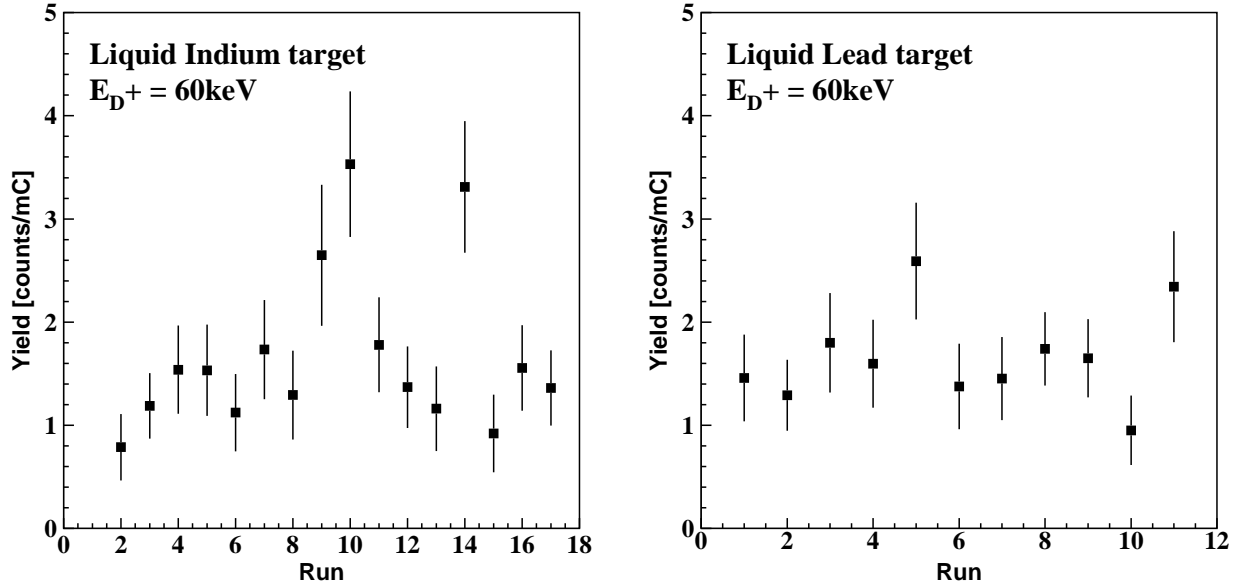


Figure B.2: Yields of the rest target event with the 60 keV D⁺ beam bombardment.

Deuteron density in liquid metal

Using the above obtained yields, the deuteron density in the liquid metal for the D₃⁺ bombardments can be estimated by the formula,

$$\rho_d = \frac{\alpha\beta Y}{6\sqrt{2}N_C(\Omega/4\pi)S} \exp\left(\frac{\alpha}{\sqrt{E_d/2}}\right). \quad (\text{B.1})$$

Here, Y is the yield of the $d + d$ reaction of the rest target, N_C is the incident beam charge number, α is obtained from the Sommerfeld parameter, and Ω is the solid angle covered by the detector. Let Y be the yield per 1 mC incident, and summarize each value below.

S	52.9×10^{-24}	keV · cm ⁻³
N_C	6.241×10^{15}	
α	31.40	keV ^{1/2}
$\Omega/4\pi$	0.0276	

The β of each metal is obtained from fitting the stopping power of SRIM in the range of $E_d = 1\text{--}20$ keV.

$$\beta = \begin{cases} 1.506 \times 10^5 & \text{For Indium} \\ 1.377 \times 10^5 & \text{For Lead} \end{cases} \quad \text{keV}^{\frac{1}{2}} \cdot \text{cm} \quad (\text{B.2})$$

We assume $Y = 2$ from Figure B.2, then, ρ_d is given as followed,

$$\rho_d = \begin{cases} 1.13 \times 10^{17} & \text{For Indium} \\ 1.04 \times 10^{17} & \text{For Lead} \end{cases} \quad \text{cm}^{-3}. \quad (\text{B.3})$$

Yield of rest target background

Assuming the deuteron density shown in the Equation (B.3), we estimated the yield of the rest target background, Y_{rest} , for the D_3^+ beam experiment, as follows.

$$Y_{\text{rest}} = \begin{cases} 1850 \exp\left(-\frac{31.40}{\sqrt{E}}\right) & \text{For In} \\ 1860 \exp\left(-\frac{31.40}{\sqrt{E}}\right) & \text{For Pb} \end{cases} \quad (\text{B.4})$$

Figure B.3 shows the experiment yield and Y_{rest} . The percentage of Y_{rest} is maximum at $E_d = 20$ keV, but it is still less than 1 %. Therefor, the contribution of the rest target background is negligibly small, and we ignored it.

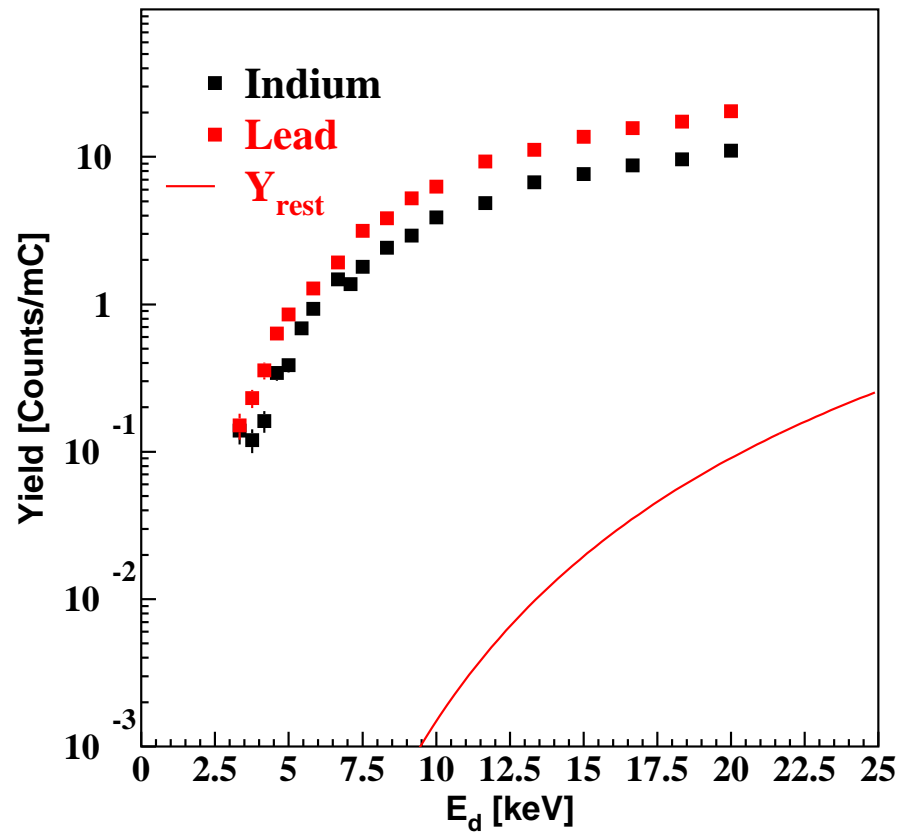


Figure B.3: Excitation functions of CCM and rest target background.

Appendix C

Absorber event

C.1 Absorber background

The yield and the energy spectra of the absorber background were calculated using a Monte Carlo method to estimate the contribution of the absorber background. The designed setup described in Figure 5.3, and the cross section of the $d + d$ reaction for bare nuclei were used for the calculation. The calculation needs energy distributions of the deuterons scattered into the absorber, including complex process as such as energy loss, and multiple scattering. For the calculation, the Transport of Ions in Matter so called, TRIM code, was adopted; it can simulate the transportation of the ion in matter.

The trajectories in the metal for 1,000,000–5,000,000 counts of deuteron with incident energies of 3.3–60 keV are calculated, and the momentum vectors of the ejected deuterons were obtained. The deuteron going on the absorber is extracted from them based on the direction of traveling. The energy distribution of the ejected deuterons is shown in Figure C.1 for the incident energy of 20 keV with the indium target. The black line is the energy distribution of all ejected deuterons, and the red line is the energy distribution of the deuterons reaching the absorber. The latter was used for the calculation of the absorber background.

The thick yield of the $d + d$ reaction in the absorber is calculated for ejected energy

E_0 by the following equation.

$$Y_{\text{thick}} = W(\theta)K(\theta) \int_0^{E_0} \sigma(E)\rho(x) \left(\frac{dE}{dx}\right)^{-1} dE \quad (\text{C.1})$$

Here, θ is a detection angle, $W(\theta)$ and $K(\theta)$ are angular distribution and solid angle ratio, $\sigma(E)$ is a cross section of the $d+d$ reaction, (dE/dx) is a energy loss of deuteron in the absorber and $\rho(x)$ is a target deuteron density which is assumed to be uniform. A calculated energy distribution for the In target with $E_0 = 20$ keV is shown in Figure 6.7. A sharp peaks similar to the energy spectra for solid target are seen. Since the charged particles are emitted forward, their energies are larger than these for solid target.

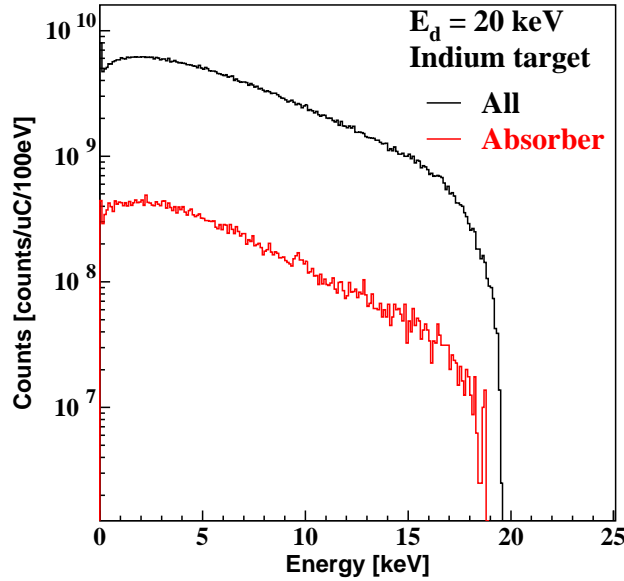


Figure C.1: Energy distribution of the back-scattered deuteron by indium. Calculation was performed by TRIM.

The excitation function of each charged particle emitted from the absorber is shown in Figure 6.8 with the CCM yield. The yield of the absorber background decreases faster as compared to that of CCM. Although not clearly seen in the figure, the magnitude of the yield is the order of ^3He particle, triton and proton. This is due

to the difference in the detector solid angle of the CM system. The yield ratios of triton and ^3He to proton are shown in Figure 6.9.

Appendix D

Energy calibration

D.1 Energy Calibration

Energy calibrations were carried out using the peak of the absorber background. Parameters for converting ADC channels to energy values were obtained by the least squares method so that the mean value of the absorber background of proton and triton correspond to the calculated value. Since the ^3He particle was most strongly influenced by the thickness of the absorber, the peak channel of ^3He was not used for the calibration. The obtained equation is shown below.

$$\begin{array}{ll} \text{In} & \left\{ \begin{array}{ll} \text{Detector 1} & E = 1.781 \times \text{CH} + 107.25 \\ \text{Detector 2} & E = 1.839 \times \text{CH} + 54.14 \end{array} \right. \\ \text{Pb} & \left\{ \begin{array}{ll} \text{Detector 1} & E = 1.804 \times \text{CH} + 77.12 \\ \text{Detector 2} & E = 1.868 \times \text{CH} + 1.41 \end{array} \right. \\ \text{Sn} & \left\{ \begin{array}{ll} \text{Detector 1} & E = 1.779 \times \text{CH} + 112.65 \\ \text{Detector 2} & E = 1.841 \times \text{CH} + 58.00 \end{array} \right. \\ \text{Bi} & \left\{ \begin{array}{ll} \text{Detector 1} & E = 1.779 \times \text{CH} + 99.95 \\ \text{Detector 2} & E = 1.854 \times \text{CH} + 39.82 \end{array} \right. \end{array}$$

A calculated mean value (solid line) and calibrated experimental mean values of absorber background (red points) are shown in Figures D.1 and D.2.

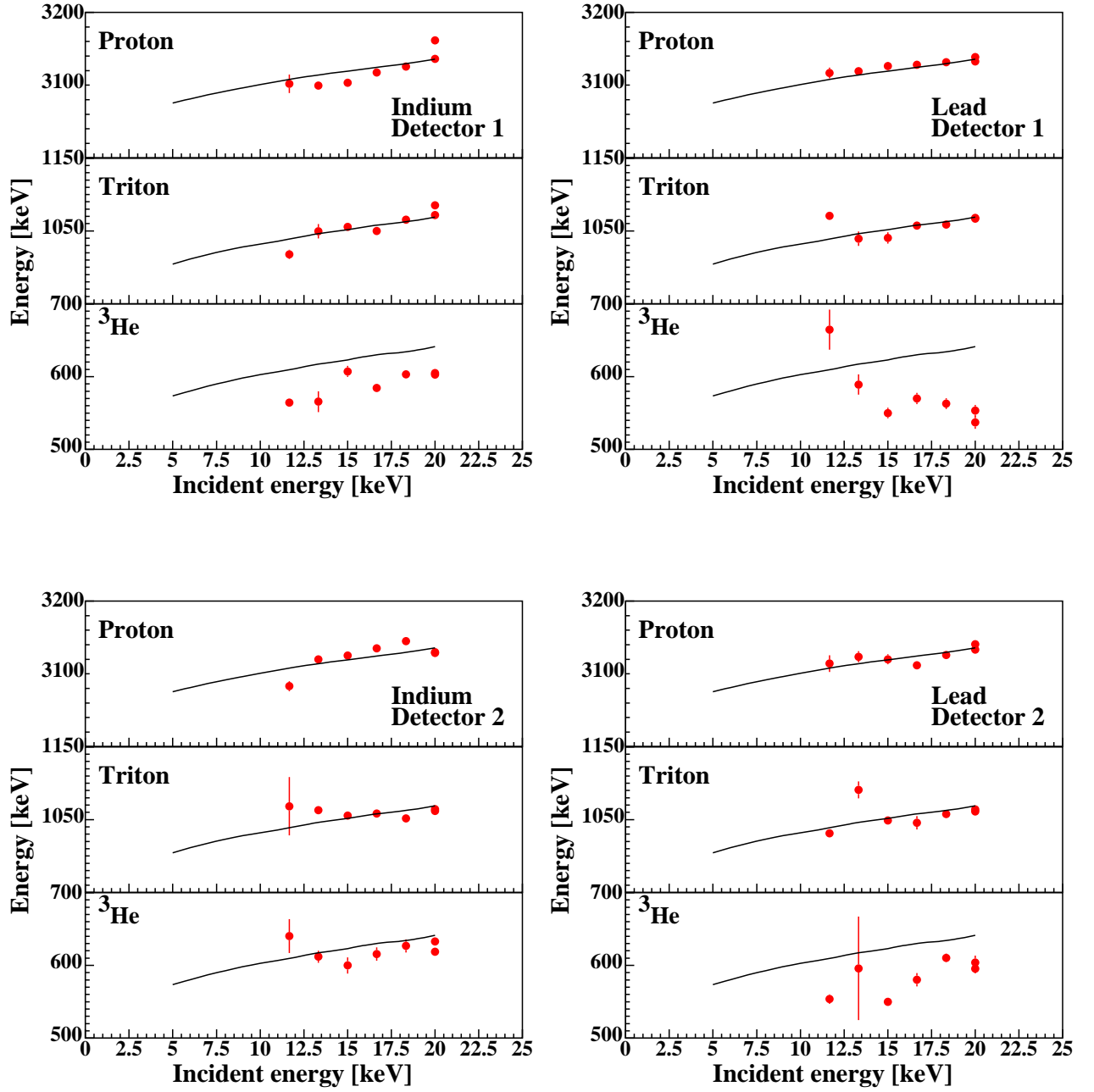


Figure D.1: Result of the energy calibration for In and Pb target experiment. Black line shows a calculated mean energy of the absorber event.

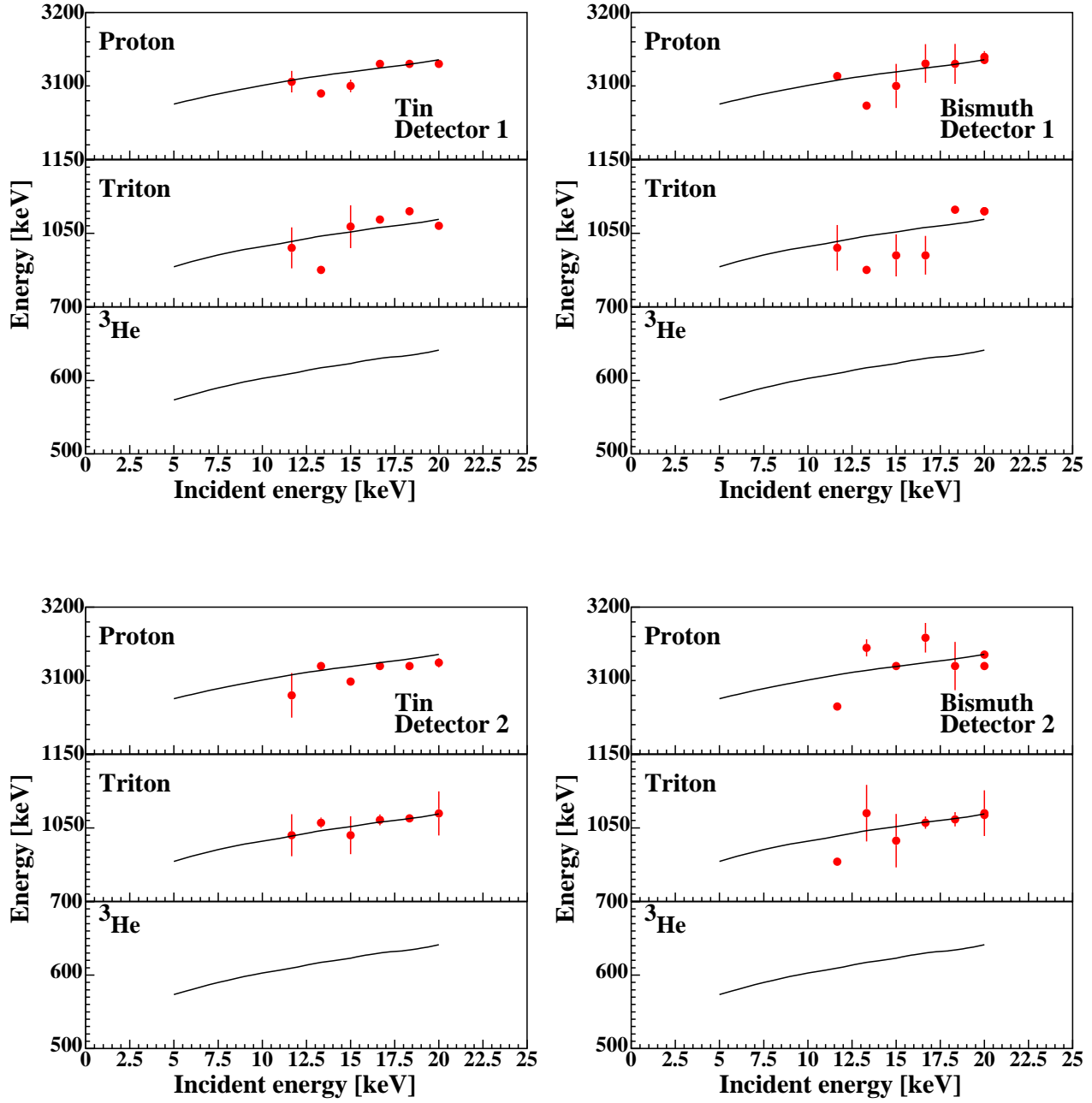


Figure D.2: Result of the energy calibration for Sn and Bi target experiment. Black line shows a calculated mean energy of the absorber event.

Appendix E

Solid angle correction

E.1 Run dependence of solid angle

As described in Section 5.3.4, a change of the target height makes a run dependence of the solid angle. The dependence was compensated based on results of the target height measurement.

E.1.1 Target height

The target height measurements (THMs) were conducted for In and Pb target experiments. Since THMs were performed for solid metal, the measured heights (h_S) were slightly lower than heights of liquid metal (h_L) due to increasing the density. It is considered that the height of the liquid metal was expressed in the following equation,

$$h_L = (h_{TH} + h_S) \frac{\rho_S}{\rho_L} - h_{TH}. \quad (\text{E.1})$$

Here, h_{TH} , ρ_S and ρ_L are depth of the target holder, 3.5 mm, and density of the solid metal and liquid metal, respectively. The results of h_S are described below.

Pb target experiment

Since the Pb target maintained clean surface during the experiments, the cleaning was not performed. Thus, the series does not have run dependence of the target height. The height was measured after finishing all run, and the height h_S is 0.37 mm.

In target experiment

The measurement for In needed cleaning every several hours of the beam bombardment. The measured distances from laser displacement sensor (LDS) to the target and the target holder are shown in Figure E.1 as a function of the number of the cleaning, N_{clean} . Due to decreasing the quantity of the target, the distance to the target became longer as the N_{clean} increases. The distance to the target holder became slightly shorter as proceeding the run. It was considered that LDS fell down as time goes on.

The run dependence of the target height is shown in Figure E.2. The height is calculated from the difference between the distance to the target holder and the distance to the target. The height seems to decrease linearly as a function of N_{clean} . The red line shows a result of fitting a liner function to the height, which is expressed in the following equation,

$$h_S(N_{\text{clean}}) = 2.235 - 0.108N_{\text{clean}}. \quad (\text{E.2})$$

The result means that the height of the indium starts from 2.235 mm and decreases 0.108 mm every cleaning.

Sn and Bi target experiment

The target height measurements were not conducted for Sn and Bi target experiment, even though the cleaning were performed many times. Therefore, we supposed the maximum variation of the height to be ± 2 mm, and considered the systematic uncertainty of the run-dependent solid angle to be ± 8 % which is equivalent to the such a height variation.

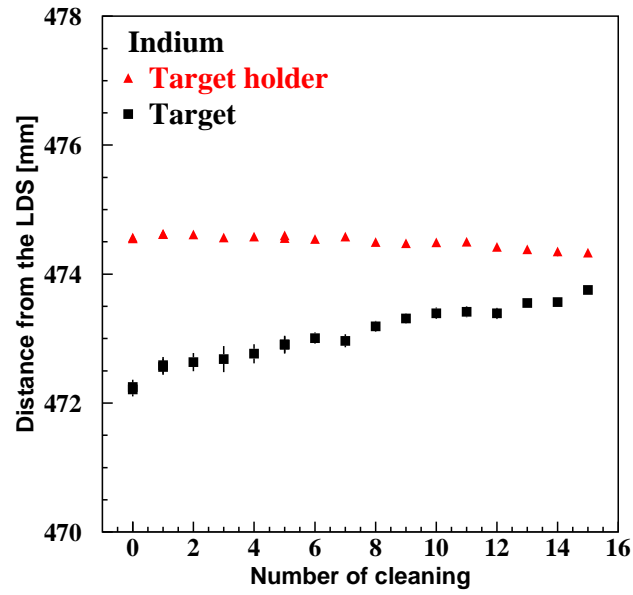


Figure E.1: Run dependence of distances from LDS to target and target holder for Setup Indium.

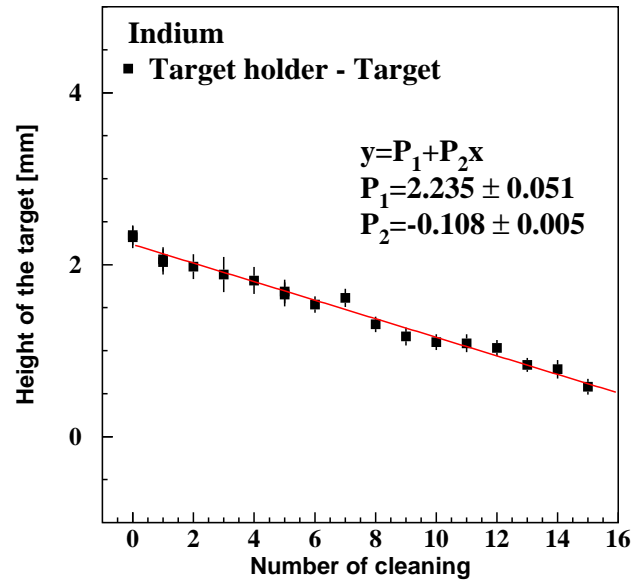


Figure E.2: Run dependence of target heights for Setup Indium.

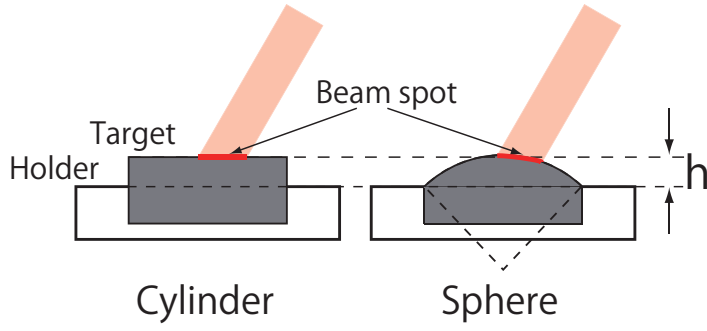


Figure E.3: Shape of the target.

E.1.2 Solid angle correction depend on the target height

The solid angle, $\Omega(h)$, was calculated as a function of the target height. The calculation was performed by a Monte Carlo methods. It is supposed that the beam intensity is uniformly distributed within a circle with a diameter of 4 mm on the target, and the beam center corresponds to the center of the target holder. Since the target scan system can not determine the shape of the target, because it can measure only distance to the target around the center due to low diffuse reflectivity. Thus, two kinds of shapes, cylinder and sphere were considered. The shapes are shown in Figure E.3. It is thought that the maximum and minimum solid angles with the same height are realized by these two shapes. Now, the definition of a target height is an average of the height within 4 mm from the center, which is the same definition of the height measured by LDS.

The target height dependence of the solid angles are shown in Figure E.4. The black points and red points show $\Omega(h)/4\pi$ respectively for the target shape of cylinder and sphere. The dependence is slightly larger for the cylinder target than for the sphere target. The black line is an approximate equation of $\Omega(h)/4\pi$ as expressed below

$$\Omega(h)/4\pi = 1.2288 + 0.04955h - 0.002359h^2. \quad (\text{E.3})$$

The discrepancy between the calculated solid angle and the approximated one is described in Figure E.5. The discrepancies with both target shapes fall in approximately 0.5 %. As this is small enough, Equation (E.3) was used to calculate the solid angle of each target height.

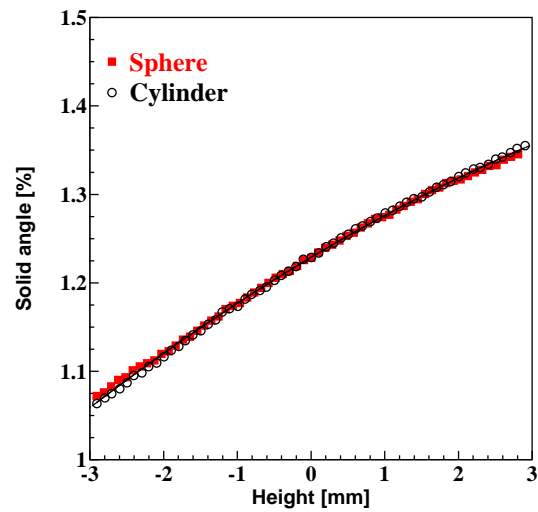


Figure E.4: Target height dependence of solid angles

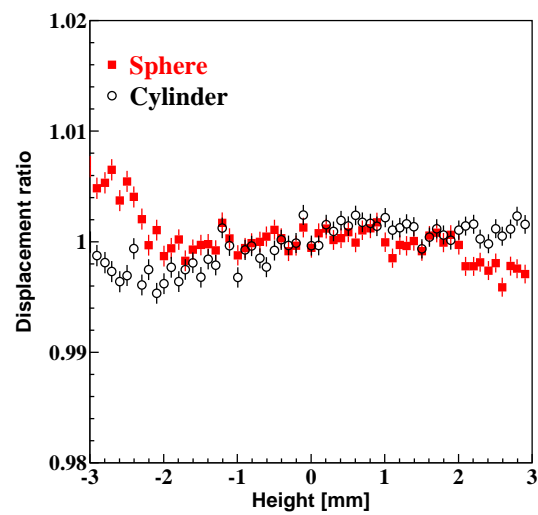


Figure E.5: Discrepancy between calculated and approximated solid angle.

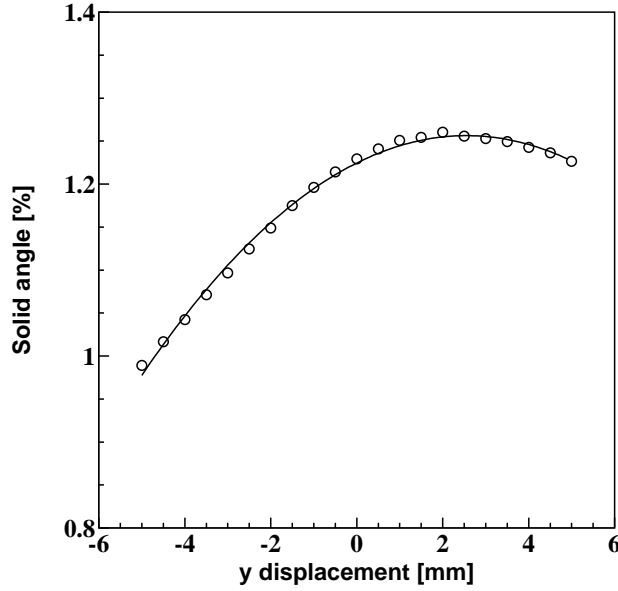


Figure E.6: Solid angle of a detector as a function of beam position. The solid curve shows a result of the fitting.

E.1.3 Solid angle correction depend on the beam position

Since the adjustment of the beam position is not conducted for Sn and Bi target experiments, the solid angle depends on the beam energy ($\Omega(y)$). The dependence was also calculated by Monte Carlo method and shown in Figure E.6. Each point shows $\Omega(y)/4\pi$ as a function of the beam position displacement from the center to y direction. A coordinate system is same as described in Figure 5.8. The approximation of the $\Omega(y)/4\pi$ is obtained by fitting, as

$$\Omega(y)/4\pi = 1.2246 + 0.02494y - 0.00489y^2. \quad (\text{E.4})$$

The y position of the beam spot for each incident energy is calculated by Equation (5.2). These equations were used to compensate the solid angle of Sn and Bi target experiments.

List of Figures

1.1	Experimental and theoretical electron screening energies reported by Czerski	6
1.2	Screening potentials for Pt in the temperature range of 20–340 °C reported by Raiola <i>et al.</i>	8
1.3	Diagram of cooperative colliding mechanism.	11
2.1	Astrophysical S-factor reported by Krauss <i>et al.</i>	17
2.2	Angular distribution coefficients of $d + d$ reactions reported by Krauss <i>et al.</i>	19
2.3	Fit of angular distribution coefficients reported by Krauss <i>et al.</i>	20
2.4	Angular dependence of proton energy emitted from $d + d \rightarrow p + t$ reaction.	25
3.1	Coulomb potentials between indium and hydrogen for some screening model	29
3.2	Particle trajectories in CM system.	31
3.3	Differential cross section of Coulomb scattering between indium and hydrogen with a CM energy of 20 keV	33
4.1	Ratio of the total cross section of the large-angle scattering for the Bohr, Moliere and ZBL screening model to the non-screening	38
4.2	Flowchart for calculation of deuteron trajectory in metal.	42
4.3	E_{cm} distribution at collision	46
4.4	Scatter plot of E_1 and E_2 at collision point.	47
4.5	Energy distributions of E_1 and E_2 at collision.	48

4.6	Calculated total yield of CCM for Indium target.	53
4.7	Yield ratio with respect to Bohr screening model.	53
4.8	Differential cross section ratio of large angle scattering with respect to one of Bohr screening model.	54
4.9	Differential cross section ratio of small angle scattering with respect to one of Bohr screening model.	54
4.10	Angular dependence of the CCM yield for each component	55
4.11	Angle dependence for each incident energy for In target	55
4.12	CCM yield for Bohr model and a thick-target yield for same incident energy with a rest deuteron target	56
4.13	Energy spectra of emitted particles from CCM for In target	57
4.14	Energy spectra of proton from CCM with each model	57
4.15	2-dimensional histogram of θ_2 vs E_p	58
4.16	The θ_2 distribution for each region of E_p	59
4.17	Energy spectra of proton emitted from CCM for each incident energy	60
4.18	The E_p spectra for each detection angle θ^{lab}	61
5.1	Overview of the High Current Ion Accelerator (HCIA) at ELPH. . . .	66
5.2	Result of the beam spot measurement with a fixed beam collimator. .	69
5.3	Summary of the beam spot measurement with a fixed beam collimator.	69
5.4	Summary of the beam spot measurement with a optimum beam colli- mator position.	70
5.5	Side view of the reaction chamber.	71
5.6	Top view of the target holders.	72
5.7	Side view of the setup in the reaction chamber.	74
5.8	Overview of geometry of detectors, absorbers, target and beam path. .	76
5.9	Typical results of the target scan with LDS for several targets. . . .	80
5.10	Stopping powers of various metals for hydrogen.	82
5.11	Stopping powers of absorbers for hydrogen and helium	83
5.12	Block diagram for the energy measurement.	87
5.13	Time and Current measurement system.	88
6.1	Raw spectra for the liquid indium target	91
6.2	Raw spectra for the solid indium target	91

6.3	Raw spectra for the liquid In target for various incident energies . . .	92
6.4	Raw spectra for the liquid Pb target for various incident energies . . .	93
6.5	Energy spectra of foreground and thermal noise	95
6.6	Briefly illustration of the absorber event.	96
6.7	Energy spectra of the absorber event for In target with incident energy of 20 keV.	96
6.8	Excitation function of the absorber event and CCM for In target. . .	98
6.9	The yield ratios of triton and ^3He to proton of absorber background.	98
6.10	Fitting result of CCM and absorber background.	100
6.11	Energy spectra for the liquid In target for various incident energies . .	101
6.12	Energy spectra for the liquid Pb target for various incident energies .	102
6.13	Integral region of the each energy spectrum.	104
6.14	Excitation function of the $d+d$ reaction with CCM for In and Pb target experiment.	105
6.15	Excitation function of the $d+d$ reaction with CCM for Sn and Bi target experiment.	106
6.16	Excitation function of proton for every target.	107
6.17	Excitation function of triton for every target.	107
6.18	Excitation function of ^3He for every target.	108
7.1	Energy spectra obtained from experiment and calculation for In target	113
7.2	Energy spectra obtained from experiment and calculation for Pb target	113
7.3	Energy spectra obtained from experiment and calculation for Sn target	114
7.4	Energy spectra obtained from experiment and calculation for Bi target	114
7.5	Experimental and calculated yield of proton and triton for the In and Pb target	115
7.6	Experimental and calculated yield of proton and triton for the Sn and Bi target	116
7.7	Enhancement factor of CCM for In target	119
7.8	Enhancement factor of CCM for Pb target	119
7.9	Enhancement factor of CCM for Sn target	120
7.10	Enhancement factor of CCM for Bi target	120
7.11	Calculated yield of the CCM as a function of the r_{dd}	122
7.12	Yield simulation of solid metal target experiment using D_3^+ beam. . .	127

7.13	Simulated enhancement factor of solid metal target experiment using D_3^+ beam.	127
7.14	The U_s^{Dummy} for the In and Pb target and reported U_s	128
A.1	Time dependence of the temperature of indium.	134
A.2	Emissivity dependence of the measured indium temperature for various heating.	136
B.1	Energy spectra of proton with the 60 keV D^+ beam bombardment. . .	138
B.2	Yields of the rest target event with the 60 keV D^+ beam bombardment.	139
B.3	Excitation functions of CCM and rest target background.	141
C.1	Energy distribution of the back-scattered deuteron by indium. Calculation was performed by TRIM.	144
D.1	Result of the energy calibration for In and Pb target experiment . . .	149
D.2	Result of the energy calibration for Sn and Bi target experiment . . .	150
E.1	Run dependence of distances from LDS to target and target holder for Setup Indium.	153
E.2	Run dependence of target heights for Setup Indium.	153
E.3	Shape of the target.	154
E.4	Target height dependence of solid angles	155
E.5	Discrepancy between calculated and approximated solid angle.	155
E.6	Solid angle of a detector as a function of beam position	156

List of Tables

2.1	Astrophysical S-factor reported by Krauss <i>et al.</i>	16
2.2	Astrophysical S-factor reported by Ronald <i>et al.</i>	18
2.3	Fitting result of a_2 parameter reported by Krauss	21
3.1	Correction coefficients of Magic formula for Moliere and ZBL screening model	32
5.1	Summary of the experimental conditions	65
5.2	Summary of the property of target metals	79
5.3	Candidate for the target of liquid metal experiments.	81
5.4	Temperature of the target	84
5.5	Solid angle of the detector for various setups	85
5.6	Cycle of the data acquisition.	86
7.1	Summary of deduced screening potentials.	118
7.2	Summary of the systematic errors	121
7.3	Summary of deduced screening potentials and errors	124
A.1	Temperature and thermal emissivity of the target	136

Bibliography

- [1] E. Rutherford. Collisions of alpha Particles with Light Atoms. IV. An Anomalous Effect in Nitrogen. *The London, Edinburgh and Dublin Philosophical Magazine and Journal of Science*, 6th series, 37:581, 1919.
- [2] J D Cockcroft and E T S Walton. Disintegration of lithium by swift protons, 1932.
- [3] Richard H. Cyburt, Brian D. Fields, Keith A. Olive, and Tsung Han Yeh. Big bang nucleosynthesis: Present status. *Reviews of Modern Physics*, 88(1):1–22, 2016.
- [4] Y. Xu, K. Takahashi, S. Goriely, M. Arnould, M. Ohta, and H. Utsunomiya. NACRE II: An update of the NACRE compilation of charged-particle-induced thermonuclear reaction rates for nuclei with mass number $A > 16$. *Nuclear Physics A*, 918:61–169, 2013.
- [5] Setsuo Ichimaru. Nuclear fusion in dense plasmas. *Reviews of Modern Physics*, 65(2):255–299, 1993.
- [6] A. G. W. Cameron. Pycnonuclear Reactions and Nova Explosions. *Astrophysical Journal*, 130:916, 1959.
- [7] Rachid Ouyed and Prashanth Jaikumar. Nuclear fusion in the deuterated cores of inflated hot Jupiters. *Astrophysics and Space Science*, 361(3):1–10, 2016.
- [8] A Y Potekhin and G Chabrier. Thermonuclear fusion in dense stars. *Astronomy & Astrophysics*, 538:A115, 2012.

- [9] Jirohta Kasagi, Hideyuki Yuki, Taiji Baba, Takashi Noda, Tsutomu Ohtsuki, and Andrey G. Lipson. Strongly Enhanced DD Fusion Reaction in Metals Observed for keV D + Bombardment. *Journal of the Physical Society of Japan*, 71(12):2881–2885, 2002.
- [10] F. Raiola, L. Gang, C. Bonomo, G. Gyürky, M. Aliotta, H. W. Becker, R. Bonetti, C. Broggini, P. Corvisiero, A. D’Onofrio, Z. Fülöp, G. Gervino, L. Gialanella, M. Junker, P. Prati, V. Roca, C. Rolfs, M. Romano, E. Somorjai, F. Strieder, F. Terrasi, G. Fiorentini, K. Langanke, and J. Winter. Enhanced electron screening in d(d,p)t for deuterated metals. *European Physical Journal A*, 19(2):283–287, 2004.
- [11] K Czerski, A Huke, A Biller, P Heide, M Hoeft, and G Ruprecht. Enhancement of the electron screening effect for d + d fusion reactions in metallic environments. *Europhysics Letters (EPL)*, 54(4):449–455, 2001.
- [12] K. Czerski, a. Huke, P. Heide, and G. Ruprecht. Experimental and theoretical screening energies for the $2\text{H}(d, p) 3\text{H}$ reaction in metallic environments. *European Physical Journal A*, 27(SUPPL. 1):83–88, 2006.
- [13] C Bonomo. Enhanced electron screening in d (d, p) t for deuterated metals. *Nuclear Physics A*, 719:C37–C42, 2003.
- [14] Francis F. Chen. *Introduction to plasma physics and controlled fusion*, volume 53. Plenum, 1984.
- [15] F Raiola, the Luna Collaboration, B Burchard, Z Fülöp, G Gyürky, S Zeng, J Cruz, a Di Leva, B Limata, M Fonseca, H Luis, M Aliotta, H W Becker, C Broggini, a D’Onofrio, L Gialanella, G Imbriani, a P Jesus, M Junker, J P Ribeiro, V Roca, C Rolfs, M Romano, E Somorjai, F Strieder, and F Terrasi. Electron screening in d(d, p)t for deuterated metals: temperature effects. *Journal of Physics G: Nuclear and Particle Physics*, 31(11):1141–1149, 2005.
- [16] V. M. Bystritsky, Vit. M. Bystritskii, G. N. Dudkin, M. Filipowicz, S. Gazi, J. Huran, A. P. Kobzev, G. A. Mesyats, B. A. Nechaev, V. N. Padalko, S. S. Parzhitskii, F. M. Pen’kov, A. V. Philippov, V. L. Kaminskii, Yu. Zh. Tuleushev, and J. Wozniak. Investigation of temperature dependence of neutron yield and

- electron screening potential for the $d(d, n)^3\text{He}$ reaction proceeding in deuterides ZrD_2 and TiD_2 . *Physics of Atomic Nuclei*, 75(8):913–922, 2012.
- [17] V.M. Bystritsky, Vit.M. Bystritskii, G.N. Dudkin, M. Filipowicz, S. Gazi, J. Huran, G.a. Mesyats, B.a. Nechaev, V.N. Padalko, S.S. Parzhitskii, F.M. Pen'kov, a.V. Philippov, Yu.Zh. Tuleushev, and V.a. Varlachev. Experimental verification of hypothesis of dd reaction enhancement by channeling of deuterons in titanium deuteride at ultralow energies. *Nuclear Instruments and Methods in Physics Research Section A: Accelerators, Spectrometers, Detectors and Associated Equipment*, 764:42–47, 2014.
 - [18] a. Huke, K. Czerski, P. Heide, G. Ruprecht, N. Targosz, and W. Zebrowski. Enhancement of deuteron-fusion reactions in metals and experimental implications. *Physical Review C - Nuclear Physics*, 78(1):1–20, 2008.
 - [19] A Huke, K Czerski, and P Heide. Measurement of the enhanced screening effect of the $d + d$ reactions in metals. *Nuclear Instruments and Methods in Physics Research B*, 256:599–618, 2007.
 - [20] H Yuki, J Kasagi, A G Lipson, T Ohtsuki, T Baba, and T Noda. Anomalous enhancement of DD reaction in Pd and Au / Pd / PdO heterostructure targets under low-energy deuteron bombardment. *Jetp Letters*, 68(11):823–829, 1998.
 - [21] Hideyuki Yuki, Takehiko Sato, Tsutomu Ohtsuki, Tetsuhiko Yorita, Yuka Aoki, Hirohito Yamazaki, Jirohta Kasagi, and Keizo Ishii. Measurement of the $D(d, p)T$ Reaction in Ti for $2.5 < E_d < 6.5$ ke V and Electron Screening in Metal, 1997.
 - [22] Y. Toriyabe, E. Yoshida, J. Kasagi, and M. Fukuhara. Acceleration of the $d+d$ reaction in metal lithium acoustic cavitation with deuteron bombardment from 30 to 70 keV. *Physical Review C - Nuclear Physics*, 85(5):1–20, 2012.
 - [23] Yoshida Eiji. 液体 In 中の低エネルギー D+D 反応の研究. *Master thesis*, 2009.
 - [24] Honda Yuki. D+3 イオン入射による液体 In 中での DD 反応の研究. *Master thesis*, 2012.

- [25] A. Krauss, H. W. Becker, H. P. Trautvetter, C. Rolfs, and K. Brand. Low-energy fusion cross sections of $D + D$ and $D + {}^3\text{He}$ reactions. *Nuclear Physics, Section A*, 465(1):150–172, 1987.
- [26] Ronald E. Brown and Nelson Jarmie. Differential cross sections at low energies for $2\text{H}(\text{d},\text{p}){}^3\text{H}$ and $2\text{H}(\text{d},\text{n}){}^3\text{He}$. *Physical review C*, 41(4):1391–1400, 1990.
- [27] Gary L. Catchen, Javed Husain, and Richard N Zare. Scattering kinematics : Transformation of differential cross sections between two moving frames. *J. Chem. Phys.*, 64(4):1737–1741, 1978.
- [28] Edgar Everhart, Gerald Stone, and R. J. Carbone. Classical calculation of differential cross section for scattering from a coulomb potential with exponential screening. *Physical Review*, 99(4):1287–1290, 1955.
- [29] J.P. Biersack and L.G. Hagmark. A Monte Carlo computer program for the transport of energetic ions in amorphous targets. *Nuclear Instruments and Methods*, 174(1-2):257–269, 1980.
- [30] Bruno Rossi. *High-Energy Particles*. New York: Prentice-Hall, 1952.
- [31] J. Remillieux. Interaction of fast molecular ions with surfaces. *Nuclear Inst. and Methods*, 170(1):31–40, 1980.
- [32] Werner Brandt and R. H. Ritchie. Penetration of swift ion clusters through solids. *Nuclear Instruments and Methods*, 132:43–55, 1976.
- [33] Michi-hiko MANNAMI and Kenji KIMURA. ANGULAR DISTRIBUTION MEASUREMENTS OF SPUTTERED Au ATOMS WITH QUARTZ OSCILLATOR. *Nuclear Instruments and Methods*, 185:533–537, 1981.
- [34] C. B. Alcock, V. P. Itkin, and M. K. Horrigan. Vapour pressure equations for the metallic elements: 298-2500 K. *Canadian Metallurgical Quartely*, 23(3):309–313, 1984.
- [35] J. R. Weeks. LEAD, BISMUTH, TIN and THEIR ALLOYS AS NUCLEAR COOLANTS. *Nuclear engineering and design*, 15:363–372, 1971.

- [36] Mithlesh Kumari and Narsingh Dass. Temperature dependence of density and thermal expansion in some liquid metals. *Journal of Non-Crystalline Solids*, 156-158(PART 1):417–420, 1993.
- [37] A.D. Kirshenbaum, J A Cahill, and A V Grosse. The density of liquid lead from the melting point to the normal boiling point. *J. inorg. nucl. Chem.*, 22(1960):33–38, 1961.
- [38] B B Alchagirov and a M Chochaeva. Temperature Dependence of the Density of Liquid Tin. *High Temperature*, 38(1):44–48, 2000.
- [39] J A Cahill and A D Kirshenbaum. THE DENSITY OF LIQUID BISMUTH FROM ITS MELTING POINT TO ITS NORMAL BOILING POINT AND AN ESTIMATE OF ITS CRITICAL CONSTANTS *. *Journal of Inorganic and Nuclear Chemistry*, 25(2159):501–506, 1963.
- [40] J. F. Ziegler and J. P. Biersack. SRIM 2012.
- [41] MIAO Jing-wei, YANG Bei-fang, HAO Shi-zuho, JIANG Zeng-xue, SHI Mian-gong, and N. CUE. INTERNUCLEAR SEPARATIONS FROM FOIL BREAKUP OF FAST H₂⁺, H₃⁺, D₂⁺ AND D₃⁺ MOLECULES. *Nuclear Instruments and Methods in Physics Research B*, 13:181–183, 1986.
- [42] V. N. Neelavathi, R. H. Ritchie, and Werner Brandt. Bound electron states in the wake of swift ions in solids. *Physical Review Letters*, 33(5):302–305, 1974.
- [43] K Czerski, a Huke, P Heide, and G Ruprecht. The 2 H(d,p) 3 H reaction in metallic media at very low energies. *Europhysics Letters (EPL)*, 68(3):363–369, 2004.
- [44] N. Targosz-Ślczka, K. Czerski, a. Huke, G. Ruprecht, D. Weissbach, L. Martin, a. I. Kiliç, M. Kaczmariski, and H. Winter. Experiments on screening effect in deuteron fusion reactions at extremely low energies. *The European Physical Journal Special Topics*, 222(9):2353–2359, 2013.
- [45] F Raiola, P Migliardi, L Gang, C Bonomo, G Gyürky, and R Bonetti. Electron screening in d (d , p) t for deuterated metals and the periodic table . *Physics Letters B*, 547:193–199, 2002.

- [46] F. Raiola, P. Migliardi, and G. Gyurky. Enhanced electron screening in $d(d, p)t$ for deuterated Ta*. *The European Physical A*, 13:377–382, 2002.